

1-1-2007

## Three Stage Level Set Segmentation of Mass Core, Periphery, and Spiculations for Automated Image Analysis of Digital Mammograms

John E. Ball

Follow this and additional works at: <https://scholarsjunction.msstate.edu/td>

---

### Recommended Citation

Ball, John E., "Three Stage Level Set Segmentation of Mass Core, Periphery, and Spiculations for Automated Image Analysis of Digital Mammograms" (2007). *Theses and Dissertations*. 4730.  
<https://scholarsjunction.msstate.edu/td/4730>

This Dissertation - Open Access is brought to you for free and open access by the Theses and Dissertations at Scholars Junction. It has been accepted for inclusion in Theses and Dissertations by an authorized administrator of Scholars Junction. For more information, please contact [scholcomm@msstate.libanswers.com](mailto:scholcomm@msstate.libanswers.com).

THREE STAGE LEVEL SET SEGMENTATION OF MASS CORE,  
PERIPHERY, AND SPICULATIONS FOR AUTOMATED  
IMAGE ANALYSIS OF DIGITAL MAMMOGRAMS

By

John Eugene Ball

A Dissertation  
Submitted to the Faculty of  
Mississippi State University  
in Partial Fulfillment of the Requirements  
for the Degree of Doctor of Philosophy  
in Electrical Engineering  
in the Department of Electrical and Computer Engineering

Mississippi State, Mississippi

May 2007

Copyright by  
John Eugene Ball  
2007

THREE STAGE LEVEL SET SEGMENTATION OF MASS CORE,  
PERIPHERY, AND SPICULATIONS FOR AUTOMATED  
IMAGE ANALYSIS OF DIGITAL MAMMOGRAMS

By

John Eugene Ball

Approved:

---

Lori M. Bruce  
Professor of Electrical and  
Computer Engineering  
Associate Director for Research,  
GeoResources Institute  
(Director of Dissertation)

---

Roger L. King  
William L. Giles Distinguished  
Professor of Electrical and Computer  
Engineering  
Associate Dean of Engineering  
(Committee Member)

---

Nicholas H. Younan  
Professor of Electrical and  
Computer Engineering  
Graduate Program Director,  
Electrical and Computer  
Engineering  
(Committee Member)

---

James E. Fowler  
Professor of Electrical and Computer  
Engineering  
(Committee Member)

---

Kirk H. Schulz  
Dean of the Bagley College of  
Engineering

Name: John Eugene Ball

Date of Degree: May 4, 2007

Institution: Mississippi State University

Major Field: Electrical Engineering

Major Professor: Dr. Lori Mann Bruce

Title of Study: THREE STAGE LEVEL SET SEGMENTATION OF MASS  
CORE, PERIPHERY, AND SPICULATIONS FOR  
AUTOMATED IMAGE ANALYSIS OF DIGITAL  
MAMMOGRAMS

Pages in Study: 170

Candidate for Degree of Doctor of Philosophy

In this dissertation, level set methods are employed to segment masses in digital mammographic images and to classify land cover classes in hyperspectral data. For the mammography computer aided diagnosis (CAD) application, level set-based segmentation methods are designed and validated for mass-periphery segmentation, spiculation segmentation, and core segmentation.

The proposed periphery segmentation uses the narrowband level set method in conjunction with an adaptive speed function based on a measure of the boundary complexity in the polar domain. The boundary complexity term is shown to be beneficial for delineating challenging masses with ill-defined and irregularly shaped borders. The proposed method is shown to outperform periphery segmentation methods currently reported in the literature.

The proposed mass spiculation segmentation uses a generalized form of the Dixon and Taylor Line Operator along with narrowband level sets using a customized speed function. The resulting spiculation features are shown to be very beneficial for classifying the mass as benign or malignant. For example, when using patient age and texture features combined with a maximum likelihood (ML) classifier, the spiculation segmentation method increases the overall accuracy to 92% with 2 false negatives as compared to 87% with 4 false negatives when using periphery segmentation approaches.

The proposed mass core segmentation uses the Chan-Vese level set method with a minimal variance criterion. The resulting core features are shown to be effective and comparable to periphery features, and are shown to reduce the number of false negatives in some cases. Most mammographic CAD systems use only a periphery segmentation, so those systems could potentially benefit from core features.

## DEDICATION

I dedicate this dissertation to my late aunt Vaudie Vee (Ball) Bonner, who died after a long battle with breast cancer. Her beautiful smile, keen sense of humor, and her love for family and for friends provide inspiration to all who knew her.

## ACKNOWLEDGMENTS

I thank my wife, Kim Ball, my children, Nathan, Elise, and Grayson, and my parents, Dr. and Mrs. Billie J. Ball, for patience and understanding when I had to spend long hours in the lab.

I sincerely thank my dissertation advisor, Dr. Lori Mann Bruce, for her constant encouragement, and for keeping me on track and focused. I thank my committee members, Dr. Roger King, Dr. Nick Younan, and Dr. James Fowler for providing valuable guidance. Thanks also go to Terrance West, Saurabh Prasad, and Vijay Shah, current PhD students at Mississippi State University, and Dr. Abhinav Mathur, a former classmate at Mississippi State University, for insightful conversations, helping with Matlab issues, and providing assistance with hyperspectral imagery.

I thank Dr. David T. Morse of Mississippi State University for providing guidance on statistical-analysis methods.

I thank Ms. Anuradha Agatheeswaran for providing Matlab code for feature extraction and downloading and organizing the mammography database.

I also owe a debt of gratitude to Dr. Jasjit Suri of Eigen, Inc., for providing level set training and answering technical questions of level set implementations, to Dr. Nikos Paragios of the Applied Mathematics and System Laboratory at the Ecole Centrale de Paris, and Dr. Ron Kimmel of the Computer Science department at Technion University, Israel, for answering technical questions on level set implementations.

I want to thank Dr. Gilda Cardenosa, M.D, in the Radiology department at Virginia Commonwealth University, and Dr. Susan Love, M.D., of the David Geffen School of Medicine at University of California, Los Angeles, for guidance and answering questions on mammography.

I thank the Electrical and Computer Engineering Department at Mississippi State University for the Honda Fellowship and the National Science Foundation for providing a Graduate Fellowship. Without this financial support, it would have been extremely difficult for me to have pursued this degree.

## TABLE OF CONTENTS

	Page
DEDICATION .....	ii
ACKNOWLEDGMENTS .....	iii
LIST OF TABLES .....	x
LIST OF FIGURES .....	xii
CHAPTER	
I.    INTRODUCTION .....	1
1.1 Digital Image Segmentation .....	1
1.2 Level Sets .....	2
1.3 Digital Mammography Analysis .....	2
1.4 Hyperspectral Image Analysis .....	4
1.5 Contributions of this Work .....	5
1.6 Dissertation Outline .....	7
II.   LEVEL SET BACKGROUND .....	8
2.1 Level Sets .....	8
2.2 Terminology .....	8
2.3 Formulation .....	9
2.3.1 Level Set Equation of Motion .....	9
2.3.2 Level Set Implementations .....	14
2.4 Functional Optimization .....	19
2.4.1 Level Set Functional Optimization over a region $R$ .....	19
2.4.2 The Chan-Vese Minimal-Variance Method .....	22
2.4.3 Level Set Applications .....	24



CHAPTER	Page
V. DIGITAL MAMMOGRAPHY CURRENT STATE OF KNOWLEDGE .....	56
5.1 Mammography Databases.....	56
5.2 Case Study from DDSM .....	59
5.3 Tumors .....	64
5.3.1 Image-Enhancement Techniques .....	64
5.3.2 The Rubber Band Straightening Transform (RBST) .....	66
5.3.3 Image-Segmentation Techniques .....	69
5.4 Spiculations.....	73
5.4.1 Image-Enhancement Techniques .....	75
5.4.2 Spiculation-Detection Techniques .....	80
5.4.3 Spiculation-Segmentation Techniques.....	81
5.5 Features .....	82
5.5.1 Patient-Information Features .....	82
5.5.2 Statistical Features .....	82
5.5.3 Textural Features .....	83
5.5.3.1 GLCM Textural Features .....	83
5.5.3.2 Laws Textural Features .....	86
5.5.4 Morphological Features .....	87
5.5.5 Normalized Radial-Length (NRL) Features .....	88
VI. DIGITAL MAMMOGRAPHIC COMPUTER AIDED DIAGNOSIS (CAD) USING ADAPTIVE LEVEL SET SEGMENTATION .....	90
6.1 Introduction.....	90
6.2 Methodology .....	91
6.2.1 Overview.....	91
6.2.2 Proposed CAD System .....	91
6.2.2.1 Image Enhancement and Denoising.....	91
6.2.2.2 Seed-point Selection .....	93
6.2.2.3 Mass Segmentation .....	94
6.2.2.4 Feature Extraction.....	100
6.2.2.5 Classification.....	101
6.2.3 Comparison CAD System (Catarious).....	102
6.2.4 Implementation Details for the Catarious System .....	104
6.2.5 General Implementation Details .....	104
6.3 Experimental Results .....	105

CHAPTER	Page
6.3.1 Qualitative Visual Comparison.....	105
6.3.2 Quantitative Comparison .....	105
6.3.3 Comparisons to Previous CAD Systems .....	106
6.4 Discussion.....	107
VII. DIGITAL MAMMOGRAM SPICULATED MASS DETECTION AND SPICULE SEGMENTATION USING LEVEL SETS .....	109
7.1 Introduction.....	109
7.2 Background.....	110
7.2.1 Spiculation Segmentation .....	110
7.2.2 Mass-periphery Segmentation .....	111
7.3 Methodology.....	111
7.3.1 Overview of the Proposed CAD System .....	111
7.3.2 Image Enhancement.....	112
7.3.3 Generalized Dixon and Taylor Line Operator (GDTLO).....	113
7.3.4 Determination of Initial Spiculation Presence .....	115
7.3.5 Selection of Spicule Segmentation Seed Points.....	116
7.3.6 Level Set Spicule Segmentation .....	119
7.3.7 Feature Extraction, Optimization, and Classification.....	124
7.3.8 Analysis of Results .....	125
7.4 Results and Discussion .....	126
7.4.1 Example Cases.....	126
7.4.2 Results of GDA Spiculation-Feature Analysis .....	126
7.4.3 Comparison of SSLS to ALSSM .....	127
7.5 Conclusions.....	130
VIII. LEVEL SET-BASED CORE SEGMENTATION OF MAMMOGRAPHIC MASSES FACILITATING THREE-STAGE (CORE, PERIPHERY, SPICULATION) ANALYSIS .....	133
8.1 Introduction.....	133
8.2 Methodology.....	134
8.2.1 Overview of the Proposed CAD System .....	135
8.2.2 Image Preprocessing for Core Segmentation.....	141

CHAPTER	Page
8.2.3 Level Set Core Segmentation.....	141
8.2.4 Feature Extraction, Optimization, and Classification.....	142
8.2.5 Analysis of Results .....	144
8.3 Results and Discussion .....	145
8.3.1 Segmentation Results.....	145
8.3.2 Feature Efficacies.....	145
8.3.3 Overall Results.....	150
8.4 Conclusions.....	151
IX. CONCLUSIONS.....	153
9.1 Conclusions.....	153
9.2 Suggested Future Work.....	155
REFERENCES .....	156

## LIST OF TABLES

TABLE		Page
1	Relative breast-cancer survival rates .....	47
2	Breast cancer incidence rates by age .....	48
3	NCI and Army (DOD) breast cancer research dollars awarded ....	55
4	ACR Bi-RADS assessment categories .....	57
5	Listing of case numbers for the DDSM database .....	60
6	Shape keywords and their meanings .....	62
7	Margin keywords and their meanings .....	64
8	Normalizing values .....	84
9	NRL feature descriptions .....	89
10	Feature list .....	101
11	Overall results .....	106
12	Results for previous studies using the DDSM database .....	107
13	Feature list .....	125
14	Overall results .....	128
15	Statistical analysis results comparing the periphery (SSLS) segmentation to the periphery only segmentation (ALSSM) .....	129
16	Feature list for extended core features .....	137
17	Feature list .....	138

TABLE	Page
18 Features considered in this analysis .....	140
19 Mean LOO ROC $A_Z$ values and 95 % confidence interval .....	148
20 Paired $t$ -test statistical results for LOO ROC $A_Z$ values .....	150
21 Overall accuracies (OA) in percent and number of false negatives (FN) .....	151

## LIST OF FIGURES

FIGURE	Page
1 Signed distance function example 1 .....	10
2 Signed distance function example 2 .....	11
3 Narrowband level set method diagram .....	16
4 Narrowband algorithm .....	17
5 Radial profile of functional E .....	21
6 Level set functional minimization example .....	22
7 Chan-Vese implementation algorithm .....	24
8 Typical image processing block diagram .....	28
9 Examples of LDA feature reduction and ROC analysis .....	31
10 Example showing TPF and FPF .....	35
11 Examples of masses with different shapes .....	58
12 Examples of masses with different margins .....	59
13 Case study breast density distributions .....	61
14 Case study Bi-RADS assessment category distribution .....	61
15 Case study DDSM subtlety rating distribution .....	62
16 Case study shape distribution .....	63
17 Case study margin distribution .....	63
18 Example showing the normal vectors for several points in the RBST .....	68

FIGURE	Page
19 Example case showing a mass segmentation, the area of the RBST, and the RBST image .....	69
20 Several DDSM cases which contain spiculated masses .....	75
21 Dixon and Taylor Line Operator (DTLO) masks .....	78
22 Proposed mammographic CAD system block diagram .....	91
23 Image-enhancement pseudo code .....	93
24 Seed-point selection algorithm pseudo code .....	94
25 Level set segmentation pseudo code .....	96
26 Example level set segmentation .....	98
27 Enhancement images and segmentation results for selected cases .....	99
28 Proposed mammographic CAD system block diagram .....	112
29 Dixon and Taylor Line Operator (DTLO) and generalized DTLO (GDTLO) masks .....	114
30 Pseudo code for generation of spiculation-enhancement image.....	115
31 Representation of masks used in spiculation seed point determination .....	117
32 Graph of spiculation feature showing seed points and spiculation enhancement image .....	119
33 Diagrams for GDTLO analysis.....	121
34 Selected spiculated mammograms showing images in spiculation processing .....	123
35 SLDA LOO $A_z$ analysis results for morphological and NRL features .....	131
36 SLDA LOO $A_z$ analysis results for statistical, GLCM segmentation (SEG) and GLCM RBST (RBST) features .....	132

FIGURE	Page
37 Three stage segmentation model .....	134
38 Proposed mammographic CAD system block diagram .....	136
39 Example segmentations .....	139
40 SLDA LOO $A_Z$ values .....	147

# CHAPTER I

## INTRODUCTION

### 1.1 Digital Image Segmentation

Digital image segmentation is an important problem in the image processing field. Gonzalez and Woods [1] define segmentation as a process that “...subdivides an image into its constituent regions or objects.” In some applications, this process is a binary task, such as segmenting a mass from surrounding tissues in a digital mammogram. Image segmentation can also be a multi-class task, such as delineating grass, cotton, soil, and trees in a remotely sensed image.

Segmentation involves extracting information from the image, and then using that information in order to divide the image into regions. The information may be simple, such as graylevel pixel values, or derived information. Examples of derived information are texture measures such as Laws texture values, pixel graylevel statistics such as mean and covariance, edge images from the output of an edge-detection algorithm, or information derived from the discrete wavelet transform or Fourier transform of the image [1]. Thresholding, region growing, and clustering are three common segmentation techniques that are widely used by the image processing community [1,2]. Segmenting by thresholding is simple and effective when the image has distinctly different pixel values for each region. Region growing and clustering typically use specialized iterative algorithms to perform segmentation. A more recent method is the level set method, which involves solving a partial differential equation that controls the motion of the segmented region in a direction normal to the region boundary [3].

The following sections in this chapter provide introductory information on level sets, digital mammography; list the contributions of this research; and provide an overview of the organization of this dissertation.

## 1.2 Level Sets

The level set method provides a robust framework for image segmentation. The level set moves the segmentation boundary normal to itself, with a speed determined by the speed function. The level set method has standard, fast, and numerically stable implementations. The main contribution of most level set work that uses these standard methods are the unique speed functions created to produce accurate segmentations. This section is intended to provide a brief overview of the method, and the level set formulation and implementation are described in detail in chapter II. Specific implementation details in terms of mammography segmentation are described in chapters VI, VII, and VIII.

Advantages of the level set methods are well-known: (1) topological changes in the evolving segmented areas are handled naturally; (2) very fast and flexible implementations such as the narrowband method are available [4]; (3) well-known and well-behaved techniques from numerical PDE solutions are readily available and well understood [4]; (4) level sets have been used extensively in image analysis and segmentation [5-7] and (5) level sets can easily adapt the segmentation to automatically determine an extremum of a function over the segmentation region or of a function of the boundary pixels, or both [8].

## 1.3 Digital Mammography Analysis

Breast cancer is the number-one leading type of cancer in women, and it is the second most fatal type of cancer [9,10]. Early detection is the key to survival, but manual diagnosis is tedious, time-consuming, and requires the skill of an expert oncologist or radiologist [11]. Mammograms are the best method of detecting breast cancer [12] and can detect cancer years

before physical symptoms occur [13]. Qian *et al.* [14] show that radiologists can benefit from the aid of computer-aided-diagnosis (CAD) systems, and Sahiner *et al.* showed that a good CAD system is comparable to expert radiologists [14,15]. The CAD systems range from more simple systems that offer image-contrast enhancement, in order to assist the radiologist in finding cancerous masses, to fully automated systems, in which the system automatically determines the presence of cancerous masses. Companies such as Kodak, R2, and Imaginis manufacture various CAD systems for detection and screening of breast cancer.

In digital mammography analysis, the desired end result is an automated decision of whether the mammogram has cancer. This is a difficult problem because the mammograms often have poor contrast, and because cancerous masses often have a appearance similar to some benign masses. Furthermore, parenchyma (the working breast organs as opposed to supportive tissue) can look like cancerous masses or hide masses if the breast is very dense.

Shape plays a very important role in determination of cancerous versus benign tissue [16], but masses often have ill-defined borders [17], making shape definition difficult. Furthermore, many of the textural features, such as features derived from the Rubber Band Straightening Transform (RBST), which is a specialized image transformation developed for mammographic image analysis in [14], are derived based on the location of the mass border. The RBST analysis methods are described in section V. Therefore, for a mammography system to have high-quality performance, segmentation is very important because many of the discriminating features derived from a mammogram often depend heavily on the location of the mass border [16].

A three stage mammographic analysis is proposed, based on three separate segmentations of the mass periphery (i.e. the main mass), the core (bright, low variance areas inside periphery), and spiculations, which are fine, tentacle-like extensions appearing on some malignant masses. The details of these methods are provided in chapters IV, V, VIII, IX, and X.

In order to assess the accuracy of the proposed method, three comparisons are performed. In all three comparisons, statistical methods will be employed to determine if results derived from

the various classification methods are statistically significant and provide significant improvement.

In the first comparison, classification results will be compared to those reported in the literature for current state-of-the-art CAD systems. Comparisons will be made to reported studies that use the same mammographic image database as the one used in this dissertation, the Digital Database of Screening Mammography (DDSM) [18].

In the second comparison, the proposed level set method will be compared qualitatively and quantitatively to the Catarious segmentation method, which uses a global optimal graylevel threshold derived from an optimal Fisher's linear discriminant analysis threshold. This alternate method is chosen because it uses the DDSM database, it achieved overall results that are comparable to other high-accuracy CAD systems reported in the literature, and it is straightforward to implement.

The third comparison will be made based on combinations of features from the core, periphery, and spiculation segmentations. The mass periphery is the main portion of the tumor, spiculations are linear filaments that extend from some malignant masses, and in this dissertation, the core is defined as the bright, low-variance portion of the mass. It is well-known that a mammographic mass periphery is typically more difficult to segment than its core, and the mass spiculations, if any exist, are more difficult to segment than its periphery. In fact, mammographic mass spiculations are notoriously difficult to segment. However, with the use of level sets, segmentation of all three components of the mass are delineated. This comparison will provide a means to determine if the more difficult segmentations provide any benefit, i.e. increase the accuracy of the mass classification as either benign or malignant, or provide increases in the efficacies of individual features.

#### 1.4 Hyperspectral Image Analysis

Although hyperspectral image analysis is not part of this dissertation, previous work has been performed by the author using level set based methods. In this work, spectral similarity

measures such as the spectral angle mapper and spectral information divergence are used to create feature vectors for initial image classification. Level set evolution with a customized speed function is used to make areas in the image more homogeneous. In a rural farm image, processing using the proposed level set method drastically improves the thematic map accuracy, and also makes the results less sensitive to the band selection method [19-22]. The following references are initial studies in hyperspectral image analysis [23]. To the best of my knowledge, these studies represent the first multi-class hyperspectral segmentation using level sets.

### 1.5 Contributions of this Work

Based on the importance of mammography and hyperspectral image processing analysis, and the capabilities of the level set method for image segmentation, the goal of this research is to design a level set based segmentation scheme for these imaging modalities which produces high-quality segmentations. In this dissertation, novel methods are designed to select, segment, and classify masses in digital mammographic images and to segment and classify land cover classes in hyperspectral remotely sensed images.

The primary and secondary contributions of this dissertation are as follows. The primary contributions include:

- Design and validation of a three-stage segmentation process based on physiological mass characteristics: mass-core segmentation, mass-periphery segmentation, and spiculation segmentation.
- Design and validation of mass-periphery segmentation using level sets with an adaptive speed function based on a measure of the boundary complexity for digital mammography segmentation. This method uses specialized speed functions which control the segmentation boundary.

- Design and validation of mass-periphery segmentation in the polar domain. This method makes the border threshold easy to implement. To the best of my knowledge, there have been no previous approaches using the polar domain for mass segmentation. Using the polar domain facilitates the creation of the speed function used to control the level set propagation by restricting radial growth of the segmentation.
- Design and validation of a mass-spiculation segmentation method using level sets driven by a modified Dixon and Taylor Line Operator (DTLO) [24]. This method uses regional minimization techniques.
- Design and validation of a mass-core segmentation using the Chan-Vese level set method [25], which provides binary segmentation with a minimal variance of the segmented region. This method uses a special form of regional minimization.
- Design and validation of a three stage mammographic system, utilizing features from the mass core, periphery, and spicules.

Secondary contributions include:

- Design and validation of new image preprocessing methods for enhancing digital mammographic images which are designed to improve performance of the segmentation methods described above.
- Extensions of the DTLO for analysis and enhancement of linear structures in images, termed Generalized DTLO (GDTLO).

- Design and analysis of features derived from the application of the DTLO, where the features are designed for the detection and classification of spiculated masses.

## 1.6 Dissertation Outline

Chapter II provides a detailed description of the level set methodology, derivations of the level set partial differential equation, and discussion of implementation and functional optimization methods. Chapter III provides background information on digital image processing systems, and discusses the various blocks of an image processing system, including statistical methods used to analyze results. Chapters IV and V give an introduction to digital mammography and list the state-of-the-art techniques used in digital mammography analysis, respectively. Chapter IV also provides definitions of many medical terms which will be used extensively in chapters VI, VII, and VIII, and also provides an overview of the characteristics of benign and malignant tumors or masses in digital mammograms. Conclusions for chapters based on the results from chapters VI – VIII, overall conclusions about level sets, and suggestions for further work are listed in Chapter IX.

## CHAPTER II

# LEVEL SET BACKGROUND

### 2.1 Level Sets

James Sethian and Stanley Osher introduced the world to the level set image processing methodology in 1987 [26]. This work is based on Sethian's doctoral dissertation on tracking the propagation of a burning front [4]. The basics of the level set methodology are found in [25]. The level set methodology provides an elegant approach to image segmentation and has been applied in many diverse fields such as edge detection, boundary extraction, image restoration, image denoising, knowledge-based image segmentation, motion analysis, medical-image analysis of many different modalities, remote sensing image analysis, graphics and simulation, etc. [4]

The level set method is based on sound and well understood mathematical principles of partial differential equations (PDE), and has very fast and flexible implementations, allowing image segmentations to grow, shrink, appear, disappear, merge, and split as required by the speed function, which controls the level set propagation.

In the following sections, terminology is introduced, the level set equation of motion is derived, implementation methods, and methods for functional optimization are discussed.

### 2.2 Terminology

The following are level set terminology used in the literature and are defined here for clarity of the following sections.

*front* – The set of all points on the zero level set. That is, the front is given by

$$\{(x, y) \mid \phi(x, y) = 0\}.$$

<i>Eikonal</i> –	The speed function which controls the level set depends only on position, and does not vary with time [4].
<i>Eulerian</i> –	This term signifies that the coordinate system is fixed [4].
<i>non-Eikonal</i> –	The speed function which controls the level set may vary with time [7].
<i>PDE</i> –	Partial differential equation.
<i>R</i> –	The region segmented by the level set. That is, $\{(x, y) \mid \phi(x, y) \leq 0\}$ .
<i>SDF</i> –	Signed distance function. A function whose values are the distance to the closest point on the front, and whose sign is negative inside the segmented region, and positive outside.
<i>ZLS</i> –	The zero level set, which is the same as the front.
<i>C(s)</i> –	A parameterization of the zero level set curve with curve parameter $s$ .
$\partial R$ –	The zero level set boundary. That is, $\{(x, y) \mid \phi(x, y) = 0\}$ .
$\partial R(s)$ –	A second form representing the parameterization of the zero level set curve with curve parameter $s$ .
$\phi$ –	The level set signed distance function, also called the implicit function.
$\Omega$ –	The image domain.

## 2.3 Formulation

### 2.3.1 Level Set Equation of Motion

The level set method tracks the motion of the zero level set boundary according to forces acting normally to the zero level set curve. In order to achieve fast processing of the level set propagation, the two-dimensional function  $\phi: \mathbb{R}^2 \rightarrow \mathbb{R}$  is defined on a discrete set of points in  $\mathbb{R}^2$ . In order to understand level sets, the equations governing their behavior need to be understood. The level set equations of motion are relatively straightforward to derive. Consider a region  $R$  in

two-dimensional space and let  $\partial R(t)$  denote the border of the region at time  $t$ . Further, let  $\phi$  be parameterized by a curve parameter variable,  $s$ , and by an artificial time variable,  $t$ . Let  $\phi_t$  be the partial derivative of  $\phi$  with respect to time. In a typical level set implementation, the implicit function  $\phi$  is a signed distance function (SDF). A SDF is a function such that  $\phi(x,y) = \pm D_B(x,y)$ , where  $D_B(x,y)$  is the Euclidean distance from the point  $(x,y)$  to the closest point on the ZLS of  $\phi$ . The positive sign is chosen if the point  $(x,y)$  is outside of the segmented region, and the negative sign is chosen otherwise. A simple example SDF is shown in Figure 1, and a segmented region and the region's corresponding SDF are shown in Figure 2 on the left and right, respectively.

$\sqrt{5}$	$\sqrt{2}$	1	1	1	1	$\sqrt{2}$	$\sqrt{5}$
$\sqrt{2}$	1	0	0	0	0	1	2
1	0	-1	-1	-1	0	1	$\sqrt{2}$
1	0	-1	$-\sqrt{2}$	$-\sqrt{2}$	-1	0	1
1	0	0	-1	-1	0	1	$\sqrt{2}$
$\sqrt{2}$	1	1	0	0	1	2	$\sqrt{5}$

Figure 1 Signed distance function example 1

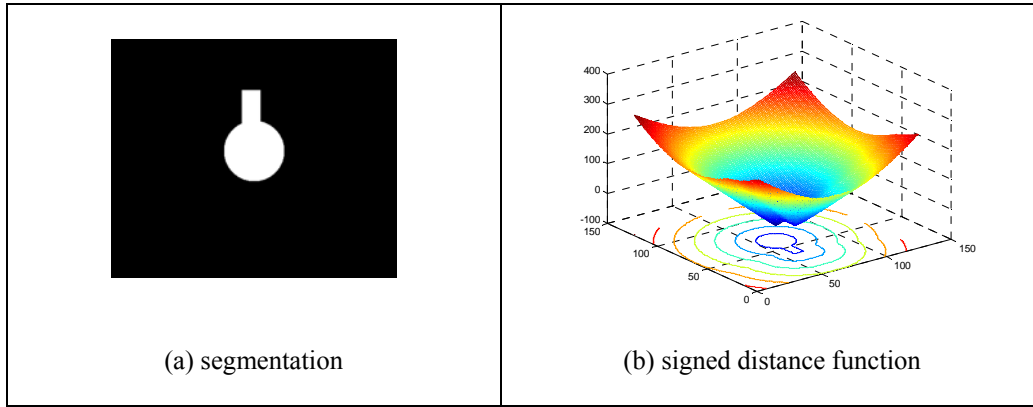


Figure 2 Signed distance function example 2

Before the level set equations are derived, a useful lemma is proven.

Lemma: For a given time  $t$ ,  $\nabla\phi$  is orthogonal to  $C(s)$ . That is, the motion of the ZLS is in a direction normal to the front.

Proof: Following Paragios [4], for a fixed time  $t$ , the relative change of  $\phi$  is zero along the curve  $C(s)$  as the arclength parameter  $s$  changes. That is,  $\phi_s = 0$ . Applying the chain rule gives

$$\frac{\partial\phi}{\partial x} \frac{\partial x}{\partial s} + \frac{\partial\phi}{\partial y} \frac{\partial y}{\partial s} = 0. \quad (2.1)$$

However, since  $\nabla\phi = \left( \frac{\partial\phi}{\partial x}, \frac{\partial\phi}{\partial y} \right) = (\phi_x, \phi_y)$  and  $C_s = \left( \frac{\partial x}{\partial s}, \frac{\partial y}{\partial s} \right) = (x_s, y_s)$ , then

$$\frac{\partial\phi}{\partial x} \frac{\partial x}{\partial s} + \frac{\partial\phi}{\partial y} \frac{\partial y}{\partial s} = \langle \nabla\phi, C_s \rangle, \text{ where } C_s \text{ is the partial derivative of the border } C(s) \text{ with respect to } s.$$

Therefore,  $0 = \langle \nabla\phi, C_s \rangle$ , and  $\nabla\phi$  is orthogonal to  $C_s$ . Q.E.D.

Following Sethian in [4], it is required that the level set implicit-function value for points on the front with path  $C(t)$  must always be zero. That is,

$$\phi(C(t), t) = 0. \quad (2.2)$$

Furthermore, from the lemma, the motion of the level set  $C(s, t)$  is in a direction normal to the ZLS,  $C(s, t)$ . By the lemma, then  $\nabla\phi$  is orthogonal to  $C_s$ . Therefore, the elementary equation governing the evolution of the level set is given by

$$\frac{\partial\phi}{\partial t} + F \cdot \nabla\phi = 0. \quad (2.3)$$

where the  $\cdot$  operator is the dot (inner) product, and  $F$  is the speed function. Using the notation that  $\phi_t = \frac{\partial\phi}{\partial t}$ , then equation (2.3) can also be written as

$$\phi_t + \langle F, \nabla\phi \rangle = 0. \quad (2.4)$$

By the lemma, since  $\nabla\phi$  is orthogonal to the boundary and  $\frac{\nabla\phi}{|\nabla\phi|}$  has unity magnitude (since  $\phi$  is an SDF), then the normal to the curve<sup>1</sup> at point  $s$  is  $\bar{n}_s = \frac{\nabla\phi}{|\nabla\phi|}$ . Since the motion of the level set is orthogonal to the ZLS boundary, then the component of the speed term  $F$  that is normal to the boundary is given by

$$F_n = \left\langle F, \frac{\nabla\phi}{|\nabla\phi|} \right\rangle. \quad (2.5)$$

Combining equations (2.3) and the second term in equation (2.5) gives:

$$\langle \nabla\phi, F_n \rangle = \left\langle \nabla\phi, F \frac{\nabla\phi}{|\nabla\phi|} \right\rangle. \quad (2.6)$$

---

<sup>1</sup> Some authors (such as Paragios) define the normal to point in the opposite direction. Most level set literature uses the convention this dissertation has adopted.

Since  $F$  at any given iteration is constant,

$$\langle \nabla \phi, F_n \rangle = F \left\langle \nabla \phi, \frac{\nabla \phi}{|\nabla \phi|} \right\rangle, \quad (2.7)$$

and since

$$\nabla \phi = \left( \frac{\partial \phi}{\partial x}, \frac{\partial \phi}{\partial y} \right) = (\phi_x, \phi_y), \quad (2.8)$$

then equation (2.8) becomes

$$\langle \nabla \phi, F_n \rangle = F \left\langle (\phi_x, \phi_y), \frac{(\phi_x, \phi_y)}{(\phi_x^2 + \phi_y^2)^{1/2}} \right\rangle. \quad (2.9)$$

After some simple algebraic manipulations,

$$\langle \nabla \phi, F_n \rangle = F \left[ \frac{\phi_x^2 + \phi_y^2}{(\phi_x^2 + \phi_y^2)^{1/2}} \right] \quad (2.10)$$

$$\langle \nabla \phi, F_n \rangle = F \left[ (\phi_x^2 + \phi_y^2)^{1/2} \right]. \quad (2.11)$$

Since  $(\phi_x^2 + \phi_y^2)^{1/2} = |\nabla \phi|$ , then

$$\phi_t + F |\nabla \phi| = 0. \quad (2.12)$$

Equation (2.12) is the level set equation for front propagation with a two-dimensional speed function,  $F(x,y)$ , acting normal to the level set curve. This equation is a PDE, and is known as the level set equation of motion [7]. Equation (2.12) is also referred to as the Eulerian formulation of the curve evolution, and is a Hamilton-Jacobi equation [4,25]. Fortunately, there are many well-behaved and fast methods for evaluating this equation on a discrete Cartesian grid and with discrete time steps [4]. The level set evolves according to the speed function,  $F$ , and it

will continue to propagate as long as the speed function is always non-negative (or always non-positive). Equation (2.12) is an initial-value partial differential equation in three dimensions. If the speed function  $F$  is independent of time, then equation (2.12) is called the Eikonal equation.

This perspective of level sets provides many advantages [4]. First, the level surface  $\phi = 0$  of the propagating hypersurface can change topology and form sharp corners [4,25]. Second, a discrete grid can be used in conjunction with a finite-difference scheme to approximate the solution in a time efficient manner [4]. Third, intrinsic properties of the front are easily calculated; for instance, the normal vector and curvature of the level set are given by  $\vec{n} = \frac{\nabla\phi}{|\nabla\phi|}$  and  $\kappa = \frac{\nabla \cdot \nabla\phi}{|\nabla\phi|}$ , respectively [5,7]. Fourth, segmentation schemes driven by minimization of a functional over the segmented region are easily adapted to level set solutions [27]. Fifth, the level set equation PDE is well-known, and its properties are well-understood. Sixth, the level set segmentation can grow, shrink, merge two disjoint regions, split a region into multiple regions, etc. The level set methodology is therefore very flexible. A demonstration of some of these abilities is shown in section 2.4.1.

### 2.3.2 Level Set Implementations

There are three basic approaches used to implement the PDE updates in the level set methodology: the full-matrix method, the narrowband method, and the fast marching method. One way to solve the level set update equation is to create a discrete grid in the  $x$  and  $y$  directions and use a PDE discrete-approximation numerical scheme to approximate the solution over the entire grid [4]. This is known as the full-matrix method. The problem with this method is that the solution time increases significantly as the image dimensions increase. The full-matrix level set method is the most flexible method, as it allows both Eikonal and non-Eikonal solutions (the segmentation can grow, shrink, split in two, merge, etc.). It also can have terms added to constrain the curve, such as a function based on the level set curvature. However, it has a very slow

implementation,  $O(N^2)$  for a  $N$  by  $N$  image, and is the slowest implementation method of the three. The full-matrix method is used only for very small images.

If flexibility in the segmentation (i.e. the ability for the segmentation to grow inwards as well as outwards) and a fast implementation are important, then the narrowband method provides an intelligent compromise to the full-matrix method without sacrificing segmentation flexibility [4]. The narrowband method is a “smarter” version of the full-matrix method, where the level set is evolved in only a small region around the front. This saves a considerable amount of overhead, as the static portions of the segmentation are not updated needlessly. In the narrow-band approach, the algorithm complexity drops from  $O(N^2)$  for the full-matrix level set implementation to  $O(kN)$ , where  $k$  is the width of the narrowband [4,7]. This complexity difference can obviously be a large savings when  $N$  is large.

Figure 3 shows a simple example of the narrowband concept. The algorithm labels points inside the zero level set as ALIVE, points in the narrowband outside of the ALIVE points as NARROW\_BAND, points just outside of the narrowband as LAND\_MINE, and all other points are labeled FAR. The level set is propagated in the NARROW\_BAND points, and the computations are performed only in the narrowband. If the front propagates to a landmine point, then the NARROW\_BAND and LAND\_MINE points are reassigned.

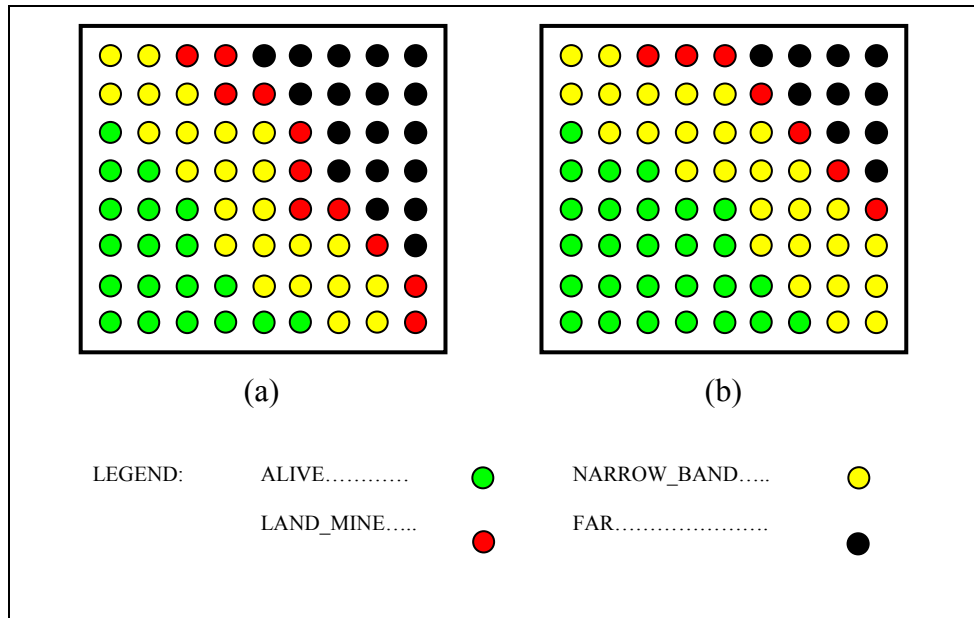


Figure 3 Narrowband level set method diagram

(a) Time  $t = 0$ . Front is advancing from the Southwest to the Northeast. (b) Time  $t > 0$ . The land mine and narrowband points have moved.

Figure 4 shows the algorithm for the narrowband method. The idea is to label points up to a certain distance away from the front as NARROW\_BAND. The PDE controlling the level set equation is updated only in the narrowband. Typically, the updates can continue for a specified number of iterations, or continue until there are no changes in the signed distance function, or until a land-mine is hit. After the stopping criteria is met, then an isocontour extractor determines the new ZLS and  $\phi$  is reinitialized around the ZLS. The narrowband is reinitialized, and narrowband and land-mine pixels are relabeled. This cycle continues until the global stopping criteria occur. The global stopping criterion is typically a maximum number of iterations or the segmentation not changing appreciably.

```

Narrowband Algorithm:
BEGIN
  Call isocontour extractor to identify zero level set
  While (stopping criteria not met)
    Label all pixels within  $k$  pixels of zero level set
    NARROW_BAND
    Label pixels on edge of narrowband as LAND_MINE
    While (no landmines hit and stopping criteria not met)
      Update  $\phi$  in narrowband only
    End Loop
    Call isocontour extractor to identify zero level set
    Reinitialize  $\phi$  in narrowband only
  End Loop
  Reinitialize  $\phi$ 
END

```

Figure 4 Narrowband algorithm

The updates are performed using a first-order space-convex Hamiltonian numerical scheme [4]. The scheme is defined as follows. Using common PDE notation, the superscripts  $+x$ ,  $-x$ , and  $0x$  denote the forward-, backward-, and central-difference approximations in the  $x$  direction, respectively, and similar notation is used for the  $y$  direction. The discrete approximations to the partial derivatives are given by the following equations:

$$\begin{aligned}
 D_{(i,j)}^{+x}\phi &= \frac{\phi(i+1,j) - \phi(i,j)}{\Delta x} & D_{(i,j)}^{-x}\phi &= \frac{\phi(i,j) - \phi(i-1,j)}{\Delta x} \\
 D_{(i,j)}^{0x}\phi &= \frac{\phi(i+1,j) - \phi(i-1,j)}{2\Delta x} & D_{(i,j)}^{+y}\phi &= \frac{\phi(i,j+1) - \phi(i,j)}{\Delta y} \\
 D_{(i,j)}^{-y}\phi &= \frac{\phi(i,j) - \phi(i,j-1)}{\Delta y} & D_{(i,j)}^{0y}\phi &= \frac{\phi(i,j+1) - \phi(i,j-1)}{2\Delta y}
 \end{aligned} \quad (2.13)$$

In practice, the grid is often uniformly spaced, i.e.  $\Delta x = \Delta y = 1$ . This assumption can reduce the time to process the discrete approximations considerably. The discrete update equation is given below, where  $\phi_{(i,j)}^n$  denotes the value of  $\phi(i, j)$  at time  $n(\Delta t)$ , where  $\Delta t$  is the time step:

$$\phi_{(i,j)}^{n+1} = \phi_{(i,j)}^n - \left[ \max(F(i, j), 0)\Delta^+ + \min(F(i, j), 0)\Delta^- \right] (\Delta t), \quad (2.14)$$

where for a first-order space-convex essentially non-oscillatory (ENO) scheme Hamiltonian approximation,  $\Delta^+$  and  $\Delta^-$  are given by

$$\Delta^+ = \left[ \max(D_{(i,j)}^{-x}\phi, 0)^2 + \min(D_{(i,j)}^{+x}\phi, 0)^2 + \max(D_{(i,j)}^{-y}\phi, 0)^2 + \min(D_{(i,j)}^{+y}\phi, 0)^2 \right]^{1/2}, \quad (2.15)$$

$$\Delta^- = \left[ \max(D_{(i,j)}^{+x}\phi, 0)^2 + \min(D_{(i,j)}^{-x}\phi, 0)^2 + \max(D_{(i,j)}^{+y}\phi, 0)^2 + \min(D_{(i,j)}^{-y}\phi, 0)^2 \right]^{1/2}$$

where the  $\max()$  and  $\min()$  functions above ensure that the proper operation of the level set are produced because these switches will turn off whenever a shock is detected in the solution (reference chapters 5 and 6 in [4]).

In contrast to the full-matrix and narrowband methods, the fast marching method can be applied only when the speed function is Eikonal, that is, always non-negative or non-positive and static with respect to time [4]. In this case, the level set can grow outwards (inwards) only, corresponding to a non-negative (non-positive) speed function. The fast marching method is fast because it employs a heap sort algorithm to quickly and efficiently sort all of the candidates for the next boundary pixel to be segmented [4,28]. The fast marching implementation cannot evolve the curves easily and naturally if there are certain constraints, such as a term in the speed function which depends on the curvature.

For two-dimensional (2D) image segmentation, the level set boundary is the ZLS of an implicit function. Therefore, when level sets are used for image segmentation, the segmentation problem becomes one of determining the appropriate speed function and initializing the implicit

function ZLS points at the seed points [5]. The speed function must be created so that it stops the level set propagation at natural boundaries, such as the distinct region between a body of water and grass on the shore in a remotely sensed image.

## 2.4 Functional Optimization

### 2.4.1 Level Set Functional Optimization over a Region R

The level set methodology allows functional optimization of a function within the level set segmented region, i.e. the set of points  $\{(x, y) \mid \phi(x, y) \leq 0\}$ . Consider a functional of the form

$$E[\partial R] = \iint_R f(x, y) dx dy, \quad (2.16)$$

where  $\partial R$  denotes the border of the region  $R$ , and  $f(x, y)$  is a function defined on the domain of the image to be segmented.

Let  $\partial R = \{x(s), y(s)\}$  be parameterized by  $s$  and define the outward normal to  $\partial R$  by  $n(s) = \{-y_s(s), x_s(s)\}$ . Following [6] and [6], by applying variational analysis, the first variation is  $\frac{\delta E[R]}{\delta R} = -f(x, y) \bar{n}$ . Applying Green's theorem with  $P(x, y) = -\frac{1}{2}f(x, y)$  and  $Q(x, y) = \frac{1}{2}f(x, y)$ , then  $f(x, y) = Q_x - P_y$ , and

$$\begin{aligned} E[\partial R] &= \iint_R f(x, y) dx dy \\ &= \iint_R (Q_x - P_y) dx dy \\ &= \iint_R (P dx + Q dy) \quad . \\ &= \iint_R (P x_s + Q y_s) \\ &= \int_{\partial R} \langle \{-Q, P\}, \bar{n} \rangle ds \end{aligned} \quad (2.17)$$

Using Lemma 1 from [24], which states that  $E_V[\partial R] = \int_{\partial R} \langle \{-Q, P\}, \bar{n} \rangle ds$  has first variation given

by  $\frac{\delta E_V[R]}{\delta R} = \text{div}(V) \bar{n}$ , then  $\frac{\delta E[R]}{\delta R} = \text{div}(\{-Q_x, P_y\}) \bar{n} = (-Q_x, P_y) \bar{n} = -f(x, y) \bar{n}$ . From the

level set equation derivation in section 2.3, the motion of the level set is in the direction normal to the boundary. Thus,

$$F_n = -f(x, y), \quad (2.18)$$

Therefore, the level set method will move the boundary to minimize the function in equation (2.16) when the speed function is  $F = -f(x, y)$ .

An example of a functional minimization using level sets is shown below. In this example, it is desired to find a segmentation that minimizes the function of equation (2.16). Let  $R_j$  be a circle of radius  $j$  with center point at  $(200, 200)$  for  $j \in \{0, \dots, 140\}$ , in an image sized  $[400 \times 400]$ . Then  $E[\partial R_j] = \iint_{R_j} f(x, y) dx dy$  defines the energy functional for a circle of radius  $j$

centered in the image. The functional  $E[\partial R_j]$  is shown in Figure 5 as a function of the radius,  $j$ . The level set progression is shown in Figure 6. In this example, the initial segmentation is shown in the upper-left-hand corner, where  $t=0.0$ . The segmented regions outside of the optimal solution shrink and vanish, while the segmentations that are inside the optimal solution grow and eventually merge into the final segmentation. This example illustrates the flexibility of level sets previously mentioned in Section 2.3.

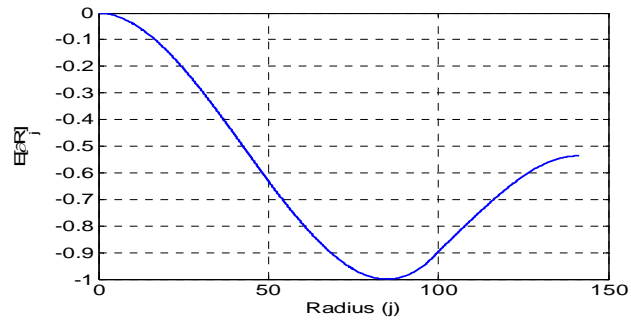


Figure 5 Radial profile of functional E

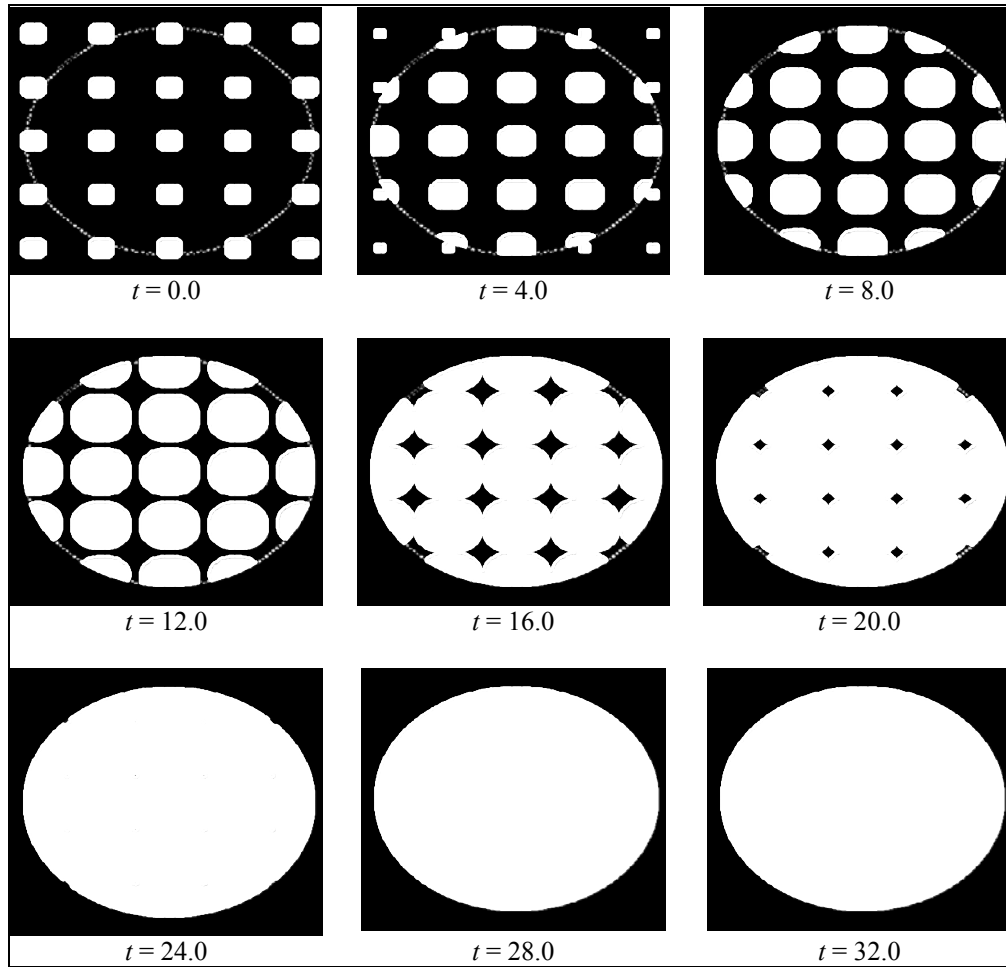


Figure 6 Level set functional minimization example

The times shown are the PDE evaluation times. The white area is the area segmented by the level sets, and the dashed white line is the optimal solution. This example uses  $\Delta t = 0.2$ .

#### 2.4.2 The Chan-Vese Minimal-Variance Method

The Chan-Vese image segmentation method is a binary segmentation method (i.e. two regions in an image) which provides a segmentation with a minimal-variance criterion [4], which is usually implemented with level sets [24]. This method is well-suited for the purpose of segmenting areas with similar intensity levels, that is, areas with low-variance. The functional controlling the segmentation is

$$E[R] = \frac{1}{2} \iint_R (I(x,y) - c_1)^2 dx dy + \frac{1}{2} \iint_{\Omega \setminus R} (I(x,y) - c_2)^2 dx dy \quad (2.19)$$

where  $R$  and  $\Omega \setminus R$  denote the segmented region and the area outside of the segmented region, respectively;  $c_1$  and  $c_2$  are the average image intensities inside  $R$  and  $\Omega \setminus R$ , respectively; and the image pixel is  $I(x,y)$ . The constants  $c_1$  and  $c_2$  are evaluated using the following equations:

$$c_1 = \frac{1}{|R|} \iint_R I(x,y) dx dy \quad c_2 = \frac{1}{|\Omega \setminus R|} \iint_{\Omega \setminus R} I(x,y) dx dy \quad (2.20)$$

where  $|R|$  and  $|\Omega \setminus R|$  are the number of pixels in region  $R$  and  $\Omega \setminus R$ , respectively.

This method can be implemented using the level set methodology. A derivation of the speed function is given in [29] by solving the corresponding Euler-Lagrange equations. The resulting speed function is given by

$$F(x,y) = (c_1 - c_2) \left( I(x,y) - \frac{c_1 + c_2}{2} \right) \quad (2.21)$$

In practice, the level set is allowed to progress through several iterations, then the constants  $c_1$  and  $c_2$  are re-evaluated, and the process repeats until the stopping criteria is met. The stopping criteria could be triggered by a small amount of change in segmentation from one iteration to another, or when the iteration count reaches a pre-defined number. The algorithm shown in Figure 7 is one algorithm used to implement the Chan-Vese method.

```

Chan-Vese Algorithm:
BEGIN
  Initialize  $c_1$  and  $c_2$ 
  While (stopping criteria not met)
    Use narrowband implementation to iterate solution
    When narrowband loop completes, evaluate  $c_1$  and  $c_2$ 
  End Loop
END

```

Figure 7 Chan-Vese implementation algorithm

The Chan-Vese method has been used previously in many image segmentation tasks [30-32], including either directly or in modified forms for medical image segmentation [4].

#### 2.4.3 Level Set Applications

Level sets are used extensively and have applications ranging from flame propagation, 2D and three-dimensional (3D) image segmentation, shape from shading, lithographic-development calculations in microchip manufacturing, optimality problems, image denoising, fluid-flow calculations, crystal growth, minimal-surface computations, shape modeling, and min/max curvature calculations [24]. Although the following is not an exhaustive list, it does give an indication of the versatility and applicability of the level set method. Based on the effectiveness of level set segmentation in these diverse medical imaging modalities, level set segmentation of mammographic masses should provide comparable or improved results to current methods. Level sets have been used in a variety of diverse applications, including:

- general-image segmentation [30,33-48]
- medical-image segmentation [45,46]
- mammography segmentation [49,50]
- medical shape recovery [51,52]

- image denoising [53]
- optimal path planning and first arrival time in seismic analysis [54]
- etching and deposition in microchip fabrication [55-57]
- motion analysis [58-60]
- shape-based and model-based image segmentation [48,61]
- image registration [62]
- simulations of smoke, water, and fire [19,20,63]
- hyperspectral image segmentation [64,65]
- tracking clouds and roads in satellite images [66]
- segmentation of radar imagery fused with satellite imagery [35]

Some specific examples of medical-image segmentation using level sets for various organs or body parts are shown below. The modalities include magnetic resonance imaging (MRI), computed tomography (CT), echocardiographic sequences (ES), digital color images (DCI), and digital mammographic images (DMI).

- Brain  
2D brain MRI [67], 3D brain from MRI [40], corpus callosum from MRI images [42], myocardium in MRI images [48], and 3D brain MRI structures [36]
- Heart and Blood  
Blood cells in CT and MRI [38], left ventricle in cardiac MRI imagery [41], left ventricle in cardiac MRI imagery [33], and 2D cardiac MRI [42]
- Liver in CT images [30]
- Prostrate  
Prostrate segmentation using Pelvic MRI [33], 3D prostrate segmentation using MRI [34]
- Skin Lesions in DCI [44]

- Optic Disk boundary in DCI retinal imagery [47]
- Echocardiographic sequences to track the cardiac muscle in ES [45]
- Digital Mammography imaging (DMI)

Breast and tumor segmentation using fast marching in DMI [46], and automated lesion/tumor detection using adaptive-mesh active contour in DMI [1]

## CHAPTER III

### IMAGE PROCESSING BACKGROUND

#### 3.1 Image Processing Block Diagram

A typical image processing block diagram is shown in Figure 8. Variations of this block diagram can include feedback paths, which are not shown in the figure. For example, there could be feedback from the feature optimization block to the segmentation block. This type of system is frequently encountered in many diverse applications, including automated target recognition (ATR) systems. As an example, a medical mammographic analysis system, often called a computer aided diagnosis (CAD) system, looks for cancerous masses in digital mammograms.

The main blocks of the system are the image enhancement block, the segmentation block, the feature extraction block, the feature optimization block, and the classification block. Also, there can be an optional analysis block after the classification block, which examines results from the segmentation, feature optimization, or the classification blocks. These blocks are discussed in the following sections.

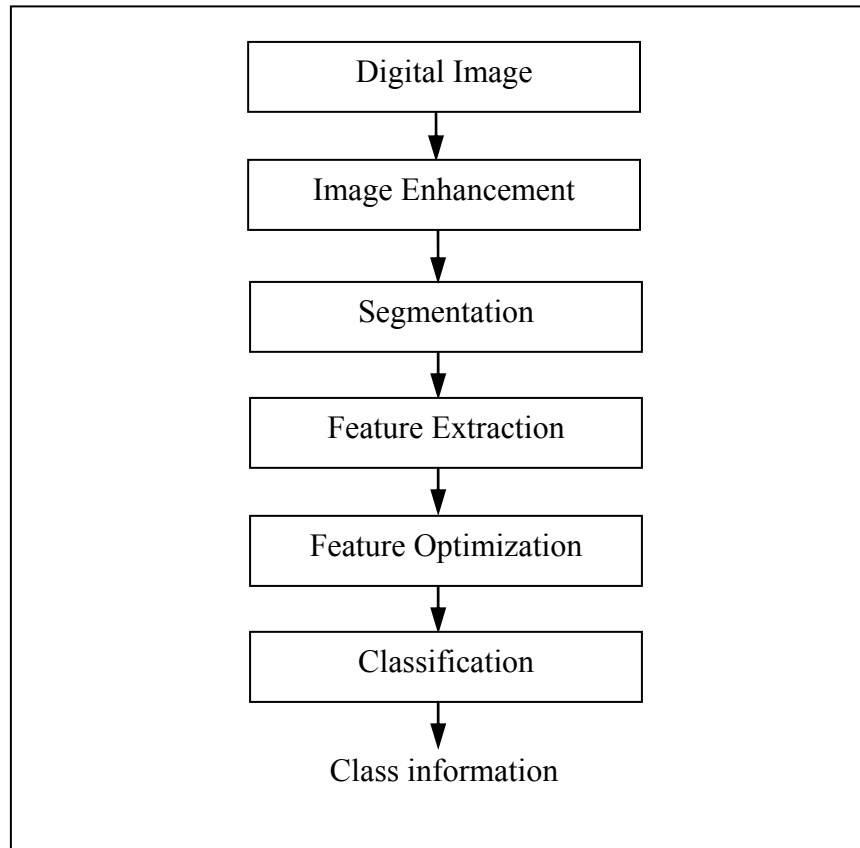


Figure 8 Typical image processing block diagram

### 3.1.1 Image Enhancement

Image enhancement is designed to (1) remove noise, and (2) enhance the image so that the other blocks in the system can perform well. There are many types of image enhancement, and typical methods depend heavily on not only the image processing system itself, but also the goals of the image processing system. Since image enhancement techniques are so diverse and application-dependent, they will be discussed in chapters V and VII.

### 3.1.2 Image Segmentation

The goal of image segmentation is to partition the image into its constituent regions. [2,68] For example, in digital mammography, segmentation might divide the breast from areas

outside of the breast, or divide a mammogram into an area containing a suspicious mass and the rest of the mammogram.

A relatively recent method of region growing is performed using the level set method. There are many different level set segmentation schemes, but most of the approaches minimize a functional over a region or a region boundary, with the hope that functional minimization provides a proper (or even an optimal) segmentation. Segmentation by the level set method is discussed in Chapter II.

### 3.1.3 Feature Extraction and Optimization

Feature extraction involves extracting features from the image or portions of the image. Features can be either global or local in nature. Global features are derived from the entire image or from large portions of the image. Local feature are derived from individual pixels or small regions of the image. Feature extraction methods for digital mammography are discussed in Chapter V.

Often, it is not clear *a priori* which features are the best features for performing a given image-processing task, such as classifying an unknown pixel in a remotely sensed image into a specific ground-cover class. Furthermore, if a large number of features are extracted and an inadequate number of training samples are available, then classification accuracies can be severely lowered if appropriate dimensionality reduction methods are not properly applied. This is known as the “curse of dimensionality” or the Hughes phenomenon [2].

Some methods commonly used for feature dimensionality reduction are forms of linear discriminant analysis (LDA), including Fisher’s linear discriminant analysis (FLDA) and stepwise LDA (SLDA), and nonlinear analysis, such as generalized discriminant analysis (GDA), a non-linear version of LDA.

### 3.1.3.1 Fisher's Linear Discriminant Analysis (FLDA)

FLDA is a method to maximize class separability by selecting an optimal linear projection of the features [2]. FLDA maximizes the so-called generalized Rayleigh quotient [2], given by

$$J(\bar{w}) = \frac{\bar{w}^T S_B \bar{w}}{\bar{w}^T S_W \bar{w}}, \quad (3.1)$$

where  $\bar{w}$  is a weight vector, and  $S_B$  and  $S_W$  are the so-called between-class and within-class scatter matrices, respectively. Both of these matrices are symmetric and positive semidefinite [2]. The optimal linear projection is found by simultaneously maximizing the projected between class scatter and minimizing the projected within class scatter. This optimization problem is solved using generalized eigenanalysis [2]. The between-class scatter matrix is given by

$$S_B = \sum_c N_c (\bar{\mu}_c - \bar{x})(\bar{\mu}_c - \bar{x})^T, \quad (3.2)$$

and the within-class scatter matrix is given by

$$S_W = \sum_c \sum_{i \in C} (\bar{x}_i - \bar{\mu}_c)(\bar{x}_i - \bar{\mu}_c)^T, \quad (3.3)$$

where  $C$  is the number of classes,  $N_k$  is the number of samples for class  $k$ , and  $N$  is the total number of samples for all classes, and

$$\bar{\mu}_C = \frac{1}{N_C} \sum_{i \in C} \bar{x}_i, \quad (3.4)$$

$$\bar{x} = \frac{1}{N} \sum_i \bar{x}_i. \quad (3.5)$$

Once the optimal projection ratio  $\bar{w}$  is determined, then the projected feature is defined by equation (3.6).

$$\vec{f}_{OPT} = \vec{f}\bar{w}, \quad (3.6)$$

It is noted that the magnitude of  $\bar{w}$  is not important, only the direction [2]. Furthermore, if there are  $C$  classes, then FLDA will generate a vector of dimensionality at most  $(C-1)$  [69]. Thus for a two-class problem, the resulting feature vector is a scalar.

Two example cases with two-dimensional features are shown in Figure 9. In the first case, shown in Figure 9 (a), (c) and (e), the features do a good job of separating the data, as can be seen in (c) and the resulting ROC curve. In the second case, which is shown in Figure 9 (b),(d), and (f), two classes are not well-separated.

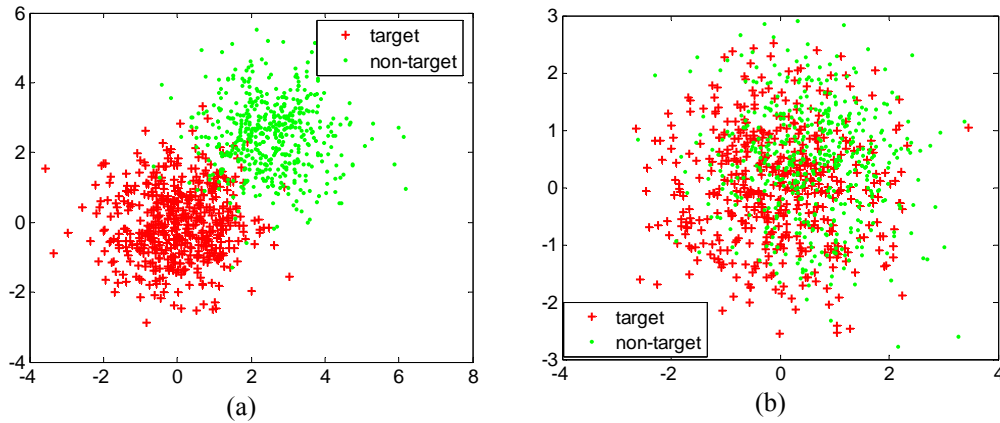


Figure 9 Examples of LDA feature reduction and ROC analysis

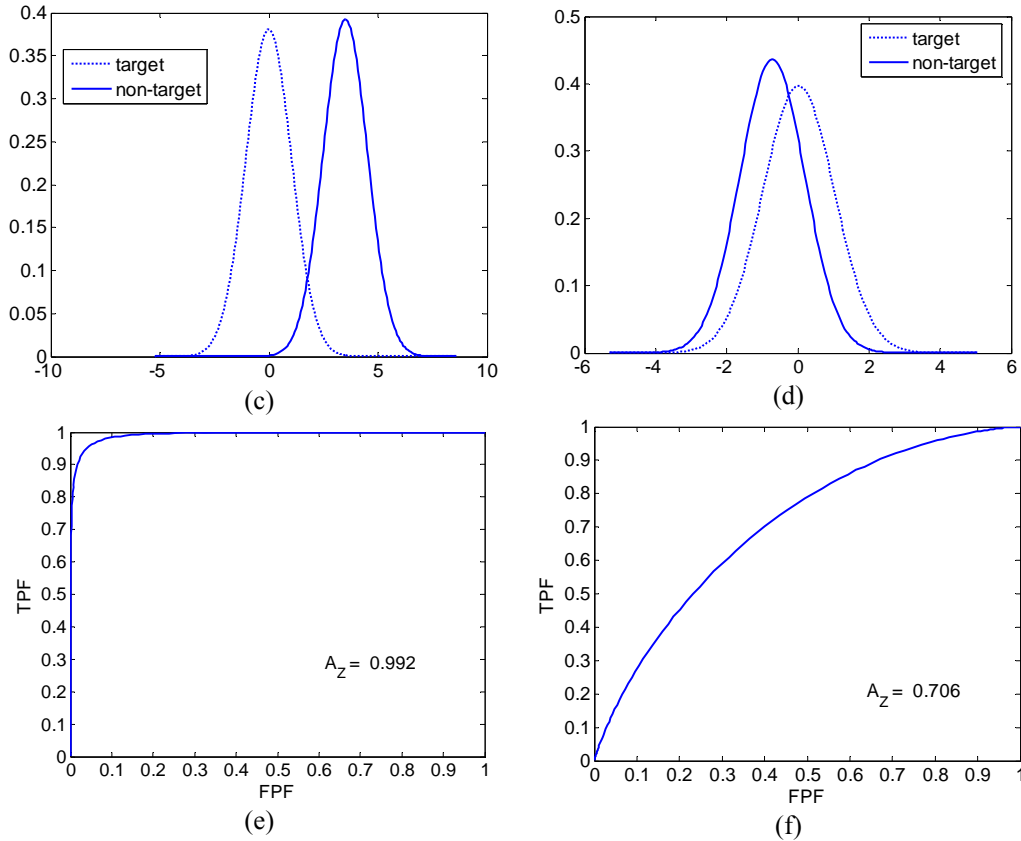


Figure 9 (continued)

(a),(c),(e): (a) Original two dimensional feature vector. (c) Scalar reduced feature vector, where dimensionality reduction is performed with LDA. (e) Resulting ROC curve and  $A_Z$  value. (b),(d),(f): (b) Original two dimensional feature vector. (d) Scalar reduced feature vector. (f) Resulting ROC curve and  $A_Z$  value.

### 3.1.3.2 Stepwise Linear Discriminant Analysis (SLDA)

Stepwise linear discriminant analysis is a version of LDA which is a compromise for a full search of the feature space. In systems with a large feature vector size, an exhaustive search for the optimal solution is generally not feasible. Stepwise LDA (SLDA) with forward selection and backwards rejection can be used for feature optimization. SLDA requires a discrimination metric to decide which features are better-suited to the given task, such as separating two different tumor types in medical imagery. Commonly used methods include receiver operating

characteristics (ROC) area under the curve, which is known as  $A_Z$ , Bhattacharyya Distance (BD), and Jeffries-Matusita distance (JMD).

The following section describes the SLDA feature reduction algorithm, and is an adaptation from the SLDA algorithm as defined in [70]. In this example,  $A_Z$  is used as the discrimination metric, but any appropriate metric theoretically could be used. The forward-selection procedure starts by calculating  $A_Z$  values for each feature separately, using one class as the target and all others as the non-target. The  $A_Z$  values are sorted in descending order. The feature with the highest  $A_Z$  value gets placed into a feature vector, and the ROC area,  $A_{Z\_BEST}$ , is set to  $A_{Z1}$ . The second-best feature is then appended to the feature vector and  $A_{Z2}$  is computed. The second-best feature is only retained if  $A_{Z2} > A_{Z\_BEST}$ . In this case,  $A_{Z\_BEST}$  is set to  $A_{Z2}$ . The third-best feature is then appended to the feature vector and  $A_{Z3}$  is computed. The third best feature is only retained if  $A_{Z3} > A_{Z\_BEST}$ . This process is continued until all the individual features are examined, or until the maximum number of features allowed is reached. The maximum number of the resulting features is determined by the minimum number of training signatures for a class [70]. As a rule of thumb, for every five to ten training signatures, one feature can be added. Therefore, to keep five to ten features, there needs to be at least 25 to 50 training signatures for each class [2].

Next, backwards rejection is then performed. Assume at this stage that there are  $b$  best features selected in the feature vector, and the best ROC area is  $A_{Z\_BEST}$ . If  $b = 1$ , then no features may be removed, and the process halts. If  $b > 1$ , then the first feature is removed, and the ROC area  $A_{Z1}'$  is calculated. If  $A_{Z1}' > A_{Z\_BEST}$ , then the first feature is removed, and  $A_{Z\_BEST}$  is set to  $A_{Z1}'$ . This process continues until all features have been removed and the ROC area has been recalculated. At the end of the procedure, there is a feature vector which contains the set of best features, the best  $A_Z$  value found, and the weighting coefficients.

The advantage of using SLDA is that it can produce very good results, even when individual features may not have very high  $A_Z$  values. Since ROC analysis is employed, then SLDA is limited to two-class (i.e. target and non-target) problems. Disadvantages of SLDA are (1)

that a exhaustive search is not performed, and (2) features near the end of the feature vector with tie scores to features earlier in the vector may not be chosen.

### 3.1.3.3 Receiver Operating Characteristics (ROC)

Receiver-operating-characteristics (ROC) analysis is developed for target-detection applications. ROC analysis uses an adjustable threshold and calculates the true positive fraction (TPF) versus the false positive fraction (FPF) [2].

In a two-class problem, assume that a scalar feature is available<sup>2</sup>. For each class, a plot of the probability density function (PDF) of the feature is shown in Figure 10. A threshold,  $\tau$ , is varied across the range of the two feature vectors, and TPF and FPF are both functions of  $\tau$  defined as

$$TPF(\tau) = \int_{-\infty}^{\tau} p(x | \omega_{TARGET}) P(\omega_{TARGET}) dx \quad (3.7)$$

and

$$FPF(\tau) = \int_{-\infty}^{\tau} p(x | \omega_{NON-TARGET}) P(\omega_{NON-TARGET}) dx, \quad (3.8)$$

where the *a priori* target and non-target probabilities are  $P(\omega_{TARGET})$  and  $P(\omega_{NON-TARGET})$ , respectively, and the PDF of the target and non-target distributions are  $p(x | \omega_{TARGET})$  and  $p(x | \omega_{NON-TARGET})$ , respectively [71]. Also, if the features are Gaussian and distributed such that the target feature has a larger mean value than the non-target feature, then the TPF and FPF equations given in equations (3.7) and (3.8) would instead have upper and lower integral limits of  $+\infty$  and  $\tau$ , respectively.

<sup>2</sup> A scalar feature can always be created for a two-class problem by using FLDA.

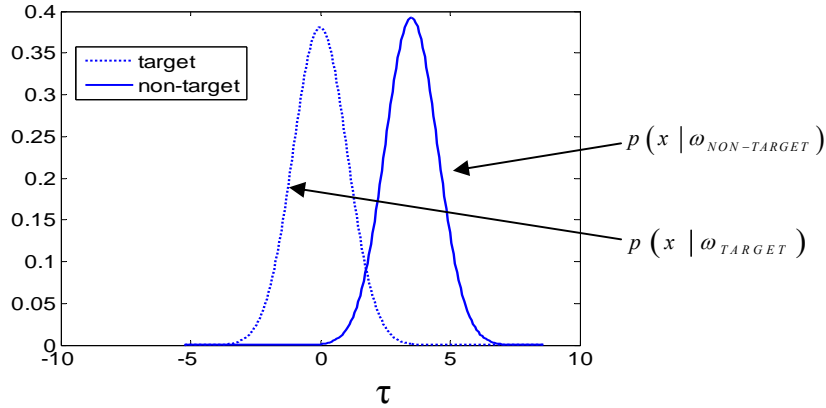


Figure 10 Example showing TPF and FPF

Note that the TPF and FPF values vary from zero to one. The figure of merit for ROC analysis is the area under the ROC curve, where the curve plots TPF( $\tau$ ) on the ordinate axis versus FPF( $\tau$ ) on the abscissa axis. This area is denoted by  $A_Z$ . The  $A_Z$  value can take on values from 0.5 to 1.0, and higher values are generally associated with better data separability. An ideal case with perfectly separable data will have an  $A_Z$  value of 1.0, while a case with absolutely no separability has an  $A_Z$  value of 0.5.

#### 3.1.3.4 Bhattacharyya Distance (BD)

Bhattacharyya distance (BD) is a measure of statistical separability. A nice feature of BD is that there is a simple formula for evaluating BD when the data has a Gaussian distribution. There is a good relationship between the BD and classification accuracy, but it is not exactly linear [2]. BD is unbounded unlike other similar measures such as the Jeffries-Matusita distance.

For two random variables (RV) with multivariate Gaussian distributions such that the first RV has mean  $\bar{\mu}_1$  and covariance matrix  $\Sigma_1$ , and the second RV has mean  $\bar{\mu}_2$  and covariance matrix  $\Sigma_2$ , then the BD is given by the following equation:

$$BD = \frac{1}{8}(\bar{\mu}_2 - \bar{\mu}_1)^T \left[ \frac{\Sigma_1 + \Sigma_2}{2} \right]^{-1} (\bar{\mu}_2 - \bar{\mu}_1) + \frac{1}{2} \ln \left( \frac{\left| \frac{\Sigma_1 + \Sigma_2}{2} \right|}{\sqrt{|\Sigma_1| + |\Sigma_2|}} \right), \quad (3.9)$$

where  $|\cdot|$  is the matrix-determinant operator [2].

### 3.1.3.5 Dimensionality Reduction

Dimensionality reduction (also known as band selection in hyperspectral applications) is a similar problem to feature selection using SLDA. A typical application of dimensionality reduction is choosing the appropriate features in order to achieve the best possible classification accuracy. Dimensionality reduction is discussed in further detail in Chapters VI and VII.

### 3.1.4 Classification

Classification is the process of taking data, interpreting the data, and assigning class labels to the data. In a digital mammography system, the entire image may be classified into malignant or benign, or individual pixels may be classified into “not of interest” and “suspicious” categories in order to facilitate further examination. In the following sections, testing methodologies, or methods of dividing the available data into training and testing sets are discussed, and then several commonly used classifiers are also discussed.

#### 3.1.4.1 Testing Methodologies

Testing methodologies are heavily influenced by the number of training samples. In digital mammography, the images are large and consume a large amount of memory. To obtain the truth about the digital mammograms involves careful, extensive analysis of the mammograms, as well as follow up analysis, and biopsy-specimen analysis.

For these reasons, the training-dataset size is often small compared to the data to be tested. Therefore, methods such as leave one out (LOO), cross validation (CV), and jackknifing<sup>3</sup> are typically used. The key to these methods is that images from the training and testing datasets are disjoint, in order to avoid introducing bias in the classifier system.

In digital mammography, a test case is an entire image. In LOO analysis, each test case is processed in a round-robin fashion, where all of the available cases except the case being tested are used for training. This method is particularly suitable for a dataset where there is a small number of training samples. The advantage of this method is that it allows small datasets to be analyzed, and the disadvantage is that for a dataset with  $N$  instances, the system is trained and tested  $N$  times.

Another method is called cross validation (CV) [2]. In  $n$ -fold cross validation, the dataset is divided as closely as possible into bins where each bin contains  $n$  instances. For instance, if there are 200 images to be processed, one could use 25-fold cross validation, which would divided the 200 images into 8 bins, where each bin contains 25 images. It is noted that LOO is in fact an extreme form of CV: 1-fold CV.

Jackknifing is another method where the available data is divided into two disjoint sets, a training set and a testing set. One user-defined parameter, which also may depend on the application as well, is the percentage of data allocated to training. In some applications, the data is split evenly, that is, 50 percent training and 50 percent testing. Once the data has been partitioned into training and testing datasets, then the classifier can take the results from the feature-optimization block and classify the test samples.

#### 3.1.4.2 $k$ -NN Classifier

The  $k$ -NN classifier is a well-known classifier which uses the  $k$  nearest neighbors of the test sample to determine the class of the test sample [2], where  $k$  is a positive integer.

---

<sup>3</sup> It is noted that in certain medical literature, the term “jackknife” means leave one out analysis.

### 3.1.4.3 Maximum Likelihood Classifier

The maximum likelihood (ML) classifier [72] takes into account class mean and covariance, and is arguably the classifier most often used in many image-processing applications. Most ML classifiers assume that the data is normally distributed, which may not be a valid assumption. There are other constraints as well: the number of training samples must be sufficient to estimate the mean and covariance matrices accurately. The ML algorithm must invert the covariance matrix, and an ill-conditioned covariance matrix can cause poor results.

Define  $\vec{f}_c^k = [f_c^k(1), \dots, f_c^k(M)]^T$ , where  $M$  is the dimensionality of the feature vector; and  $\vec{f}_c^{(k)}$  is the  $k$ -th feature vector for class  $C$ . The ML classifier first estimates the class means using the following equation:

$$\bar{\mu}_c = \frac{1}{N_c} \sum_{k=1}^{N_c} \vec{f}_c^{(k)}, \quad (3.10)$$

where  $N_c$  is the total number of samples for class  $C$ , and the mean vector is  $\bar{\mu}_c = [\mu_c(1), \dots, \mu_c(M)]^T$ . The covariance matrix is estimated with the unbiased estimator

$$\Sigma_c[i, j] = \frac{1}{N_c - 1} \sum_{k=1}^{N_c} (f_c^{(k)}(i) - \mu_c(i))(f_c^{(k)}(j) - \mu_c(j)), \quad (3.11)$$

where  $i, j \in \{1, \dots, T\}$ , and  $T$  is the total number of classes. Assuming the *a priori* probabilities of the class  $k$  is  $P(\omega_k)$ , then the ML decision rule is based on the log-likelihood ratio.

For a two-class case, the decision formula is

$$h(\vec{x}) = \left[ \begin{array}{l} \frac{1}{2}(\vec{x} - \bar{\mu}_1)^T \Sigma_1^{-1}(\vec{x} - \bar{\mu}_1) - \frac{1}{2}(\vec{x} - \bar{\mu}_2)^T \Sigma_2^{-1}(\vec{x} - \bar{\mu}_2) \\ + \frac{1}{2} \ln \left( \frac{|\Sigma_1|}{|\Sigma_2|} \right) - \ln \left( \frac{P(\omega_1)}{P(\omega_2)} \right) \end{array} \right], \quad (3.12)$$

where  $P(\omega_1)$  and  $P(\omega_2)$  are the *a priori* probabilities of classes one and two, respectively, and the decision rule is to assign the unknown sample with feature vector  $\bar{x}$  to class one if  $h(\bar{x}) > 0$  and to class two if  $h(\bar{x}) < 0$  [73]. If there is a tie, then there is no way to determine the class with ML, and the class is then assigned using some predetermined method, such as always choosing class one. This choice is implementation-dependent.

#### 3.1.4.4 Fisher's Linear Discriminant Analysis (FLDA) Classifier

FLDA is previously discussed as a method of dimensionality reduction, but it can also be used as a classifier. In a two-class problem, then from [73], the optimal threshold is zero, and the class decision is given by the following rule: select class one if  $x' > 0$ , and select class two otherwise, where

$$x' = (\bar{\mu}_1 - \bar{\mu}_2)^T S_p^{-1} \bar{x} - \frac{1}{2} (\bar{\mu}_1 - \bar{\mu}_2)^T S_p^{-1} (\bar{\mu}_1 + \bar{\mu}_2), \quad (3.13)$$

and  $S_p$  is the pooled variance given by

$$S_p = \frac{1}{n_1 + n_2 - 2} [(n_1 - 1)S_1 + (n_2 - 1)S_2], \quad (3.14)$$

while  $S_1$  and  $S_2$  are the covariance matrices of classes one and two, respectively [74].

#### 3.1.5 Analysis of Results

Classifier results can be analyzed in many different ways. For a two-class problem, such as deciding whether a suspicious mammographic mass is malignant or benign, overall accuracies (OA), true positives (TP), false positives (FP), false negatives (FN), and true negatives (TN) are all good figures of merit.

First, consider an ATR system with target and non-target classes labeled one and two, respectively. For example, in digital mammography, class one could be malignant, and class two

benign. Assuming there are  $T$  total cases, let the actual class of the  $j$ -th case be  $c_j$  and the classifier results of the  $j$ -th case be  $r_j$ . Thus  $c_j, r_j \in \{1, 2\} \forall j \in \{1, \dots, T\}$ . Then OA, TP, FP, FN, and TN are defined as

$$\begin{aligned}
 OA &= \frac{\#[c_k = r_k \mid k \in \{1, \dots, T\}]}{T} 100 \\
 TP &= \#[c_k = 1, r_k = 1 \mid k \in \{1, \dots, T\}] \\
 TN &= \#[c_k = 2, r_k = 2 \mid k \in \{1, \dots, T\}], \quad (3.15) \\
 FP &= \#[c_k = 1, r_k = 2 \mid k \in \{1, \dots, T\}] \\
 FN &= \#[c_k = 2, r_k = 1 \mid k \in \{1, \dots, T\}]
 \end{aligned}$$

where OA is in percent, and  $\#[x]$  means the total number of cases where  $x$  is true.

When comparing the results of two different image-processing systems, or of one system with two different segmentation methods, a reasonable question to ask is whether the two outputs are statistically different. For a two class ATR system such as a digital-mammography CAD system, one could compare the reduced features using statistical methods for continuous data, or compare the resulting classifications using statistical method for discrete data.

Consider a two-class system such as a digital-mammographic CAD system. Let the final results be class one for malignant and two for benign. Then two acceptable forms of comparison are in order: (1) a comparison between the reduced-feature efficacies, using  $A_Z$  or BD as a metric, and (2) a comparison between final class labels versus the true labels. In either case, consider a system with  $N_1$  instances from class one (malignant) and  $N_2$  instances of class two (benign). Therefore, there are a total of  $T = N_1 + N_2$  cases. If the classification scheme uses LOO analysis and SLDA for feature DR, for example, then for each of  $T$  mammograms, an  $A_Z$  value is calculated.

Assume that there are  $j \in \{1, \dots, J\}$  different systems to be compared, and define  $A_Z^{j(i)}$  as the LOO  $A_Z$  value when the  $i$ -th case is tested (and the other cases are used for training) from system  $j$ . Let the overall system  $A_Z$  value for system  $j$  be defined as the mean of the LOO  $A_Z$  values, that is,

$$OVERALL A_Z^j = \frac{1}{T} \sum_{k=1}^T A_Z^{(k)}. \quad (3.16)$$

Now if system  $m$  is to be compared to system  $n$ , an appropriate statistical test is the two-tailed paired-samples  $t$  test [75]. In this test, the null hypothesis is that the two samples have an average value different from zero. Let

$X_i = A_Z^{m(i)}$  be the LOO  $A_Z$  value for system  $m$  and case  $i$ ,

$Y_i = A_Z^{n(i)}$  be the LOO  $A_Z$  value for system  $n$  and case  $i$ ,

$w_i$  be the weight for case  $i$ ,

$W$  be the sum of the weights, and

$T$  be the total number of cases.

Note that a typical application sets the weights to 1.0. The difference statistic is given by

$$D = \bar{X} - \bar{Y}, \quad (3.17)$$

where

$$\bar{X} = \frac{1}{W} \sum_{i=1}^T w_i X_i, \quad (3.18)$$

and

$$\bar{Y} = \frac{1}{W} \sum_{i=1}^T w_i Y_i, \quad (3.19)$$

are the weighted means of the LOO  $A_Z$  values for system  $m$  and  $n$ , respectively. The variances of  $X$  and  $Y$ , and the covariance of  $XY$  are calculated using the following three formulas:

$$S_X = \frac{T}{T-1} \sum_{i=1}^T \left( w_i X_i^2 - \left[ \sum_{j=1}^T (w_j X_j) \right]^2 \right), \quad (3.20)$$

$$S_Y = \frac{T}{T-1} \sum_{i=1}^T \left( w_i Y_i^2 - \left[ \sum_{j=1}^T (w_j Y_j) \right]^2 \right), \quad (3.21)$$

and

$$S_{XY} = \frac{T}{T-1} \sum_{i=1}^T \left( w_i X_i Y_i - \left[ \sum_{j=1}^T (w_j X_j) \right] \left[ \sum_{k=1}^T (w_k Y_k) \right] \right), \quad (3.22)$$

respectively. The standard error of the difference is calculated using

$$SE_D = \sqrt{\frac{S_X^2 + S_Y^2 - 2S_{XY}}{T}}. \quad (3.23)$$

The  $t$  statistic is given by

$$t = \frac{D}{SE_D}. \quad (3.24)$$

and has  $W-1$  degrees of freedom. The systems are considered statistically different if the null hypothesis does not hold. If a confidence level of  $\alpha$  is used, i.e.  $\alpha=0.05$  corresponds to 95 % confidence interval, then the  $t$  value is used to calculate a probability  $p$  based on the  $t$  statistic with  $W-1$  degrees of freedom. The  $p$ -value is compared to  $\alpha$ , and if  $p < \alpha$  then the results are considered statistically significant.

## CHAPTER IV

### DIGITAL MAMMOGRAPHY BACKGROUND

#### 4.1 Digital Mammography

Digital mammography uses x-rays to project structures in the 3D female breast onto a 2D image [76]. The primary use for digital mammography is for screening for breast cancer. According to the American Cancer Society (ACS), breast cancer is the leading type of cancer in women and the second most fatal type of cancer in women [77].

The following sections (i) define relevant medical-imaging terms, (ii) discuss the basics of breast anatomy and physiology, (iii) discuss the importance of mammography, (iv) lists several other imaging modalities for detection of breast cancer, along with their pros and cons, (v) discuss the basics of digital mammographic imaging analysis, (vi) describes a block diagram of the basic mammographic CAD system, and (vii) provides an overview of mammographic presentation characteristics for benign and malignant tumors, including spiculated tumors.

#### 4.2 Terminology

The following are medical terminology used in the literature and are defined here for clarity of the following sections.

<i>adipose</i> –	Medical terminology for fat tissue.
<i>benign</i> –	Not cancer [77]. Contrast with malignant.
<i>cancer</i> –	A general term for tissue cells that lack a controlled growth pattern [77].

<i>circumscribed</i> –	Confined to a limited area; bounded.
<i>CAD</i> –	Computer aided diagnosis. A system which analyzes digital mammograms, and may produce prompts of suspicious areas, or a benign/malignant decision. CAD systems are used as aids to radiologists.
<i>desmoplastic</i> –	A desmoplastic reaction is the growth of fibrous tissue around a tumor.
<i>fibroadenoma</i> –	A round breast tumor typically found in younger women [78].
<i>fibrosis</i> –	Growth of fiber-like tissue.
<i>hamartoma</i> –	A mass resembling a tumor that represents anomalous development of tissue natural to a part or organ rather than a true tumor [78].
<i>hyperplasia</i> –	An increase in the number of cells in an organ, excluding tumor formation [77].
<i>hypoxia</i> –	Too little oxygen in cells, which can be caused by insufficient blood supply [77].
<i>lipoma</i> –	A tumor consisting of fat cells [77].
<i>lobulated</i> –	A mammographic-shape keyword denoting a knobby shaped lesion.
<i>malignant</i> –	A tumor which is cancerous. Contrast with benign.
<i>metastasize</i> –	A malignant tumor which has spread from its point of origin to a distant site.
<i>necrosis</i> –	Local tissue death [77]. Tumors that grow so fast that they outgrow their blood supply exhibit necrosis.
<i>galactoceles</i> –	A fluid-filled sac in the breast caused by milk duct blockage [77].
<i>palpable</i> –	Capable of being felt.
<i>parenchyma</i> –	The working tissue of an organ, as opposed to the connective tissue [77]. Contrast with stroma.
<i>scirrhous</i> –	Indurated or knotty. This term describes the appearance of some breast tumors.

<i>spicule</i> –	A sharp body with a needle-like point [77]. Spiculations present in digital mammograms as nearly linear filaments extending from the tumor periphery.
<i>spiculated</i> –	A mass with spicules.
<i>stellate</i> –	A star shaped, spiculated mass.
<i>stroma</i> –	The connective tissue of an organ, as opposed to the working tissue [79]. Contrast with parenchyma.
<i>tumor</i> –	Tumor literally means swelling. Tumors refer to any pathological process that produces a lump or mass in the body [75,80].
<i>radiolucent</i> –	Tissue that allows x-rays to pass through with low attenuation. Contrast with radio-opaque.
<i>radio-opaque</i> –	Tissue that wholly or partially blocks x-ray passage. Contrast with radiolucent.
<i>ROI</i> –	Region of interest.

### 4.3 Breast Anatomy and Physiology

The breast is a complex organ composed of adipose tissue (fat), fibroglandular tissue, arteries, veins, lymphatic elements, connective tissue, milk-producing lobules, and ducts [81]. According to Willison, the glandular tissue, or parenchyma, consists of typically 15-20 lobes which contain ductal structures and stroma (connective structures). Each lobe branches into segmental ducts, which further branch into smaller and smaller ducts until the lobules are reached. The lobules are the milk-producing portions of the breast [75].

The connective tissue, or stroma, is composed of the intralobular stroma, which gives the lobule its shape and position, and the extralobular stroma, which holds the larger ductal structures [75]. Cooper's ligaments are fibrous membranes which completely sheath the breast lobes [81].

It is well-known how each type of tissue typically appears mammographically [82]. The resulting image is created from differential attenuation of x-rays passing through the breast

structure [79]. Contrast in the resulting image is achieved by variations in attenuation of different types of breast tissue. Adipose tissue will appear as radiolucent areas on the mammogram, which are darker (i.e. black to gray) portions of the image. Fibroglandular tissue appears light grey to white, and is more radio-opaque. The term fibroglandular includes blood vessels, lymphatics, stroma, and ductal structures. According to Kundel and Dean, mammography can not differentiate between glandular, connective stroma, and malignant tissues unless adipose tissue is present to provide sufficient contrast [9,10].

#### 4.4 Importance of Mammography

Mammography is important for many reasons. First, early detection can increase survival rates [83,84] and decrease the probability that cancer cells are able to infiltrate other parts of the body [85]. The survival rate of breast-cancer patients is inversely related to the tumor size and to the number of auxiliary lymph nodes that are found with malignant cells [86]. The average time for a cancer to grow large enough to be palpable (about 1 cm diameter) is 10-12 years [76,87-89]. Mammography can detect cancer years before physical symptoms occur [90]. Mammography can detect noninvasive, intraductal cancers in some patients [86,91]. Often, early detection finds a minimal cancer, and the cure rate approaches 95 percent [92]. Survival rates by stage at diagnosis are shown in Table 1 (for years 1995-2001 data).

Table 1 Relative breast-cancer survival rates

Stage at Diagnosis	Relative Survival Rate in percent
Local	97.9
Regional	81.3
Distant	26.1

Source: [76]. Local means confined to the breast. Regional means outside of the breast, in the lymph nodes, or both. Distant means the cancer spread to remote parts of the body.

Second, early stage breast cancer typically produces no symptoms when the tumor is small and most treatable [83,93]. When breast tumors are detected in a self-examination by women, most of the tumors have already metastasized [86]. According to Lillé, the average size of a tumor detected by a woman practicing a breast self exam is about 1.0 inch (approximately 2.5 cm), whereas mammography can detect tumors as small as 0.25 inch (approximately 0.50 cm) [11,94].

Third, mammograms are currently considered by the medical community as the best method of detecting breast cancer [95]. Randomized clinical trials have shown that mammography reduced breast cancer mortality by about 18% and about 25-30% for women who are 40 to 50 and 50 to 70 years old, respectively [96]. Barry *et al.* concludes that screening mammography and treatment have reduced the breast cancer death rate in the US [97].

Fourth, breast cancer is costly, both in terms of money spent and loss of life. The ACS reports that reducing the number of mammographic false detections and missed detection of cancer could reduce cancer healthcare costs by \$100 million [98]. According to the National Cancer Institute (NCI), breast cancer expenditures are \$8.1 billion, and the average Medicare payment per individual for the first year following diagnosis is \$11,000, where these figures are in year 2004 projected dollars [76]. The ACS predicted an estimated 211,240 new cases of invasive breast cancer to be diagnosed in 2005, and approximately 40,410 women are expected to die from breast cancer [87]. Every 13 minutes four American women develop breast cancer, and one

woman dies from breast cancer [99]. Table 2 shows relative breast cancer incidence rates versus age for women.

Table 2 Breast cancer incidence rates by age

Age	Probability of Developing Breast Cancer
By age 30	1 out of 2,212
By age 40	1 out of 235
By age 50	1 out of 54
By age 60	1 out of 23
By age 70	1 out of 14
By age 80	1 out of 10
Ever	1 out of 8

Source: [75,100].

#### 4.5 Digital-Mammography Image Analysis

Digital-mammographic analysis is a very difficult problem because of the complexity of digital mammograms, poor contrast, and in many cases, a lack of a clearly defined mass border. First, a digital mammogram is a 2D image of a 3D and highly complex structure [80]. Due to the complex 3D nature of breasts and the view used when taking the mammogram, some tumors may be partially obscured.

Second, it is well-known that digital mammograms often have poor contrast, especially in dense breasts [75]. Many specialized methods have been developed to denoise and enhance digital mammographic images. These methods are discussed in chapter V.

Third, according to Egan, there is a wide variability in the appearance of mammograms of different patients [101]. Adipose tissue has a higher concentration of low-atomic-number elements, such as hydrogen and carbon, and therefore low-energy x-rays are attenuated less in adipose tissue than other tissues [82]. The amount of adipose tissue present in the breast is important, because it provides good contrast with other structures in the breast [75,79]. Furthermore, the size of malignant lesions that can be detected depends on the adipose content of

the breasts, and breasts with more fat provide the ability to detect smaller tumors than breasts with a paucity of fat [75,102]. It is well-known to radiologists that many premenopausal women have denser breasts which make diagnosis more difficult, due to low contrast between masses and parenchyma [75,103].

Fourth, cancerous masses often have a similar appearance to some benign masses, or even normal fibroglandular breast tissue [103], and many masses have irregular or obscured borders [75,103]. Furthermore, most masses do not fit a distinct border type, but have mixtures of border types [75,87,103,104]. Mass borders are a primary method radiologists use to identify benign versus malignant masses [102].

Fifth, many radiologists interpret a large number of mammograms, and often have limited time to identify suspicious masses. Furthermore, most of the mammograms they examine are normal [105]. Cheng *et al.* point out that even expert radiologists can have an interobserver variation rate of 65 to 75 percent [13].

#### 4.6 Computer-Aided-Diagnosis (CAD) Systems

Many digital mammography CAD systems have been previously developed, both as experimental models in academia, and marketed and FDA-approved products for breast-cancer detection. CAD systems serve a variety of purposes, including: (1) providing a prompting system for radiologists to help them locate suspicious areas in the mammogram, (2) providing a second opinion, by analyzing the mammogram and deciding if a mass is malignant or benign, and (3) providing mammographic image enhancement, where digital mammograms can be enhanced for noise removal or to provide better contrast with the overall goal to allow better radiologist interpretation.

Qian *et al.* [106] and Huo *et al.* [14] show that radiologists can benefit from the aid of CAD systems. Sahiner *et al.* demonstrated that a good CAD system is comparable to expert radiologists [107]. Burhenne *et al.* show that CAD can potentially reduce radiologists' false negative rate, which is the rate at which a radiologist falsely detects a malignant mass as benign

[108,109]. Chan *et al.* and Hadjiiski *et al.* determined that CAD can potentially reduce unnecessary biopsies [110]. CAD is able to mark 77 percent of cancers missed by radiologists at a prior screening [111]. Freer and Ulisse found almost twenty-percent increase in radiologist's cancer-detection rate using CAD versus not using CAD [112]. Karssemeijer *et al.* report that CAD provides a good second opinion for radiologists [105]. Cheng *et al.* point out that a digital-mammographic CAD system can increase a radiologist detection sensitivity <sup>4</sup> by around 10 percent [79].

#### 4.7 Tumors

According to Kundel and Dean [79], tumors can be modeled as a mass of abnormal tissue growing in normal tissue. The tumor has a matrix that may be textured or homogeneous, and a boundary with normal tissue that can either be fuzzy, distinct, or combinations of both [79]. The tumor biology determines the characteristics of the tumor matrix as well as the characteristics of the boundary between the tumor and the surrounding tissues [113].

According to Winchester and Winchester, mammographic analysis of a mass is based on its shape, margins, and density. Round or oval-shaped masses are most often associated with benign processes, such as a cyst or fibroadenoma. Masses with radiolucent areas are normally indicative of benign processes such as hamartomas, lipomas, galactoceles, fat necrosis, and lymph nodes. Increasing mass-shape irregularity, lobulations, and spiculations increase the probability of malignancy. Most malignant masses are mammographically dense (that is, radio-opaque) compared to fibroglandular tissue [75,85].

---

<sup>4</sup> In medical terminology, sensitivity is the proportion of truly diseased cases which are identified as being diseased.

#### 4.7.1 Tumor Shapes

Tumor shapes are described by industry standardized keywords. The shapes are classified as oval, irregular, lobulated, or round. Oval masses are shaped like ovals and typically have a smooth, well-defined border. Round masses are similar to oval masses but are shaped more like a circle. Irregular masses may have obscured borders, or borders that are complex in nature [85]. Lobulated masses, which are also known as knobby masses, are composed of multiple tiny masses, which overlap to form a dense, knobby lesion with indistinct borders [85].

Masses that are more regular, such as oval or round shaped masses, have a 98 percent chance of being benign [114]. Most benign tumors have well-defined borders unless they are obscured by fibroglandular tissue [75]. However, there are malignant processes that can present as a round or oval mass.

#### 4.7.2 Tumor Margins

The margins are described as circumscribed, ill-defined, obscured, or spiculated. Egan points out that most masses do not fit exactly one category, but may have a mixture of border types [75]. Circumscribed tumors have a well-defined margin and are confined masses. A mass with a circumscribed margin implies a more regular and smooth margin [85]. Most circumscribed masses are benign [114]. Ill-defined margins indicate the margins are not well-defined. Obscured masses are masses whose borders are partially hidden. These types of tumors can be very problematic for automated systems to analyze properly. Spiculated tumors have long, thin, linear projections emanating from the tumor boundary. These tumors are discussed in section 4.7.4.

#### 4.7.3 Benign Processes

According to Peters and Voegeli, benign processes include fibroadenomas, tension cysts, lipomas, papillomas, and granular-cell myoblastomas [115], or hematomas [114]. Fibroadenomas which arise from lobules are a heterogeneous mix of fibrous and glandular elements. Fibroadenomas present as round, oval, or lobulated masses with well-defined margins [114].

Tension cysts present mammographically as round-to-oval, homogeneous-density masses, and are the result of a partially obstructed cyst [114]. Lipomas present as a lucent area with a surrounding thin capsule, and are a slow-growing, common benign tumor. Lipomas are of no clinical significance, and usually appear in older women [115]. Hematomas are most often caused by blunt force or surgical trauma to the breast, and present mammographically as a ill-defined mass or diffuse area of increased density [80].

#### 4.7.4 Malignant Tumors

According to Love, it is generally accepted by the medical community that breast cancer starts in the lining of the milk ducts [80]. These cancerous cells can originate from the ductal cells or the lobules at the ends of the ducts, and are called lobular or ductal carcinoma, respectively. Cancers that remain near the point of origin and do not spread are called *in situ*, while cancers that invade surrounding areas are called *infiltrating carcinomas*.

An infiltrating ductal cancer forms a hard, firm lump due to scar tissue formation, called fibrosis. This scar tissue is the result of a desmoplastic response to the cancer [80]. Infiltrating lobular carcinomas tend to send small, spiculated projections out from the tumor and tend not to exhibit much of a desmoplastic response from surrounding tissues [80]. These types of cancer are therefore much harder to detect.

According to Love [79], and to Kundel and Dean [80], tumors can cause angiogenesis, which means they cause blood vessels to grow, because of chemicals called tumor angiogenic factor, which are produced by the cancer cells in response to hypoxia. In one extreme, a large amount of blood vessels may indicate that the tumor is growing aggressively. In the other extreme, the tumor grows too fast for its blood supply, and hypoxia and cell necrosis will occur [79]. These changes in the blood supply and reactions of areas outside of the tumor may show up in mammograms as an altered texture near the tumor, and texture features derived from areas outside of the tumor can be very important in determining malignancy. Areas of hypoxia or necrosis contribute to changes in the tumor matrix texture [75,87,104,113,116].

Malignant tumors can present mammographically as non-spiculated or spiculated. Spiculations present in digital mammograms as nearly linear filaments extending from the mass periphery [117] and grow somewhat linearly within  $\pm 45^\circ$  normal to the mass boundary [85]. Spiculated lesions are also called stellate lesions because of their star-shaped appearance.

According to Voegeli [85], a stellate lesion is a central mass whose borders consist of radiating spicules of various lengths. Malignant cells are often found growing along these spicules. Stellate masses are associated with a significant degree of fibrous proliferation and hyperplasia [118].

Spiculations are most often associated with malignant processes, but not always. Franquet *et al.* point out that spiculated lesions can be formed from benign and malignant processes [75], although they are usually a sign of a cancerous mass [119], and Demirkazik *et al.* state that spiculated lesions are most often associated with cancerous pathologies [120]. Furthermore, Jeske, Bernstein, and Stull state that the presence of irregularly-shaped masses and spiculations increase the probability of malignancy [113]. According to Winchester and Winchester, mammographic masses with irregular shapes or spiculations increase the probability of malignancy [104]. Tabár and Dean report that spiculations of scirrhous carcinomas usually present as sharp, dense, fine lines radiating in all directions, and spiculations of sclerosing duct hyperplasia present as fine, low-density bunches (like a broom) [120]. Jeske, Bernstein, and Stull [113] and Winchester and Winchester [98] state that “the classic mammographic presentation of infiltrating ductal carcinoma is a high density mass with spiculated margins”.

Spiculations are very important in detection of malignant masses, and many methods have been developed for enhancing images, detecting spiculations, and segmenting spicules. These algorithms are discussed in detail in chapter V and in section 5.4.

#### 4.8 Cancer Research Funding

Cancer is a very serious problem and is very costly in terms of money and loss of life. Therefore, many government and private agencies fund small to large amounts of cancer research. This section briefly discusses some of these agencies.

According to the NCI, 2004 cancer cost expenditures are approximately \$8.1 billion [121], and the NCI spent approximately \$560.1 million on breast-cancer research in fiscal year 2005 [121]. A summary of breast-cancer research expenditures for the NCI and for the Army is shown in Table 3. The Susan G. Komen breast cancer foundation has awarded over 1000 research grants totaling more than \$180 million<sup>5</sup>. The ACS<sup>6</sup> funded about 29.2 million in extramural and intramural research money for breast-cancer research in fiscal year (FY) 2004-2005. Several Government agencies which provide cancer-research funding include the National Institute of Health (NIH), the Centers for Disease Control and Prevention (CDC), Department of Defense (DoD), Office of Orphan Products Development (FDA), and the Veterans Affairs (VA) Research & Development. Some of the private foundations that fund cancer research include:<sup>7</sup> the American Cancer Society, Burroughs Wellcome Fund, California Breast Cancer Research Program, The Charlotte Geyer Foundation, Damon Runyon Cancer Research Foundation, Robert Wood Johnson Foundation, and the Wendy Will Case Cancer Fund, Inc.

<sup>5</sup> source: <http://cms.komen.org/komen/GrantsAwards/index.htm>

<sup>6</sup> source: [http://www.cancer.org/docroot/RES/content/RES\\_7\\_3\\_Funding\\_By\\_Research\\_Area.asp?sitearea=RES](http://www.cancer.org/docroot/RES/content/RES_7_3_Funding_By_Research_Area.asp?sitearea=RES)

<sup>7</sup> source: <http://www.cancer.gov/researchandfunding/organizations>

Table 3 NCI and Army (DOD) breast cancer research dollars awarded

Year	2001	2002	2003	2004	2005
NCI Research Dollars (in millions)	475.2	522.6	548.7	566.2	560.1

Fiscal Year	2002	2003	2004	2005	2006
Army (DOD) Research Dollars (in millions)	150.0	150.0	150.0	150.0	127.5

Sources: NCI: [16]. Army: <http://cdmrp.army.mil/pubs/factsheets/bcrpfactsheet.htm>

# CHAPTER V

## DIGITAL MAMMOGRAPHY CURRENT STATE OF KNOWLEDGE

### 5.1 Mammography Databases

There are several publicly available mammographic databases used in digital-mammography research. Two of the more commonly used databases are the Digital Database of Screening Mammography (DDSM) [122], provided free of charge from the University of South Florida, and the Mammographic Image Analysis Society (MIAS) database [16], from the U.K. The studies in this dissertation use the DDSM database, and it will be described in detail below.

The DDSM database is a set of digital mammograms which have been analyzed by expert radiologists [123]. The DDSM database has been used in various research papers and is known to contain a variety of easy to difficult cases. Each case consists of digital-mammogram images which have been scanned by a Howtek or Lumisys scanner, a physician-drawn region of interest (ROI) around the suspicious area in the mammogram, and statistics about the case. The statistics include: a unique case number, the patient age, the diagnosis, a Bi-RADS<sup>8</sup> rating, a physician-assigned subtlety rating, a numerical-density rating, a keyword describing the mass margins, a keyword describing the mass shape, a numerical-subtlety rating, and whether the mass is spiculated.

The diagnosis is malignant or benign, and is backed up by biopsies and follow-up visits. The ACR Bi-RADS rating system rates the mammogram on a scale of one to six, where a higher

---

<sup>8</sup> The American College of Radiologists (ACR) breast imaging and reporting data system (Bi-RADS) rating is an industry accepted standard for rating digital mammograms.

number indicates a higher chance of malignancy. The ratings and their meanings are given in Table 4.

Table 4 ACR Bi–RADS assessment categories

Rating	Meaning
1	Negative: There is nothing to comment on. The breasts are symmetric and no masses, architectural distortion or suspicious calcifications are present.
2	Benign Finding(s): Like Category 1, this is a “normal” assessment, but here, the interpreter chooses to describe a benign finding in the mammography report.
3	Probably Benign Finding—Initial Short–Interval Follow–Up Suggested: A finding placed in this category should have less than a 2% risk of malignancy.
4	Suspicious Abnormality—Biopsy Should Be Considered: This category is reserved for findings that do not have the classic appearance of malignancy but have a wide range of probability of malignancy that is greater than those in Category 3.
5	Highly Suggestive of Malignancy—Appropriate Action Should Be Taken: (Almost certainly malignant.). These lesions have a high probability ( $\geq 95\%$ ) of being cancer.

Source: [124].

The subtlety rating is an integer from one to five determined by radiologists working with the DDSM database. This rating is not the same as the ACR subtlety rating often used in digital mammography [16]. A rating of one indicates the mammogram is the least subtle, and a rating of five indicates the mammogram is the most subtle. The scale is defined such that a mass with a subtlety rating of  $N$  is  $N$  times more subtle than a mass with a subtlety rating of one.

The margins and shapes are described by industry accepted keywords. The shapes are classified as oval, irregular, lobulated, or round. The margins are described as circumscribed, ill-defined, obscured, or spiculated. Figure 11 shows example cases for these shapes, and Figure 12 shows example cases for these margin types. In these two figures, the physician ROI is shown in white so that the mass location can be easily seen.

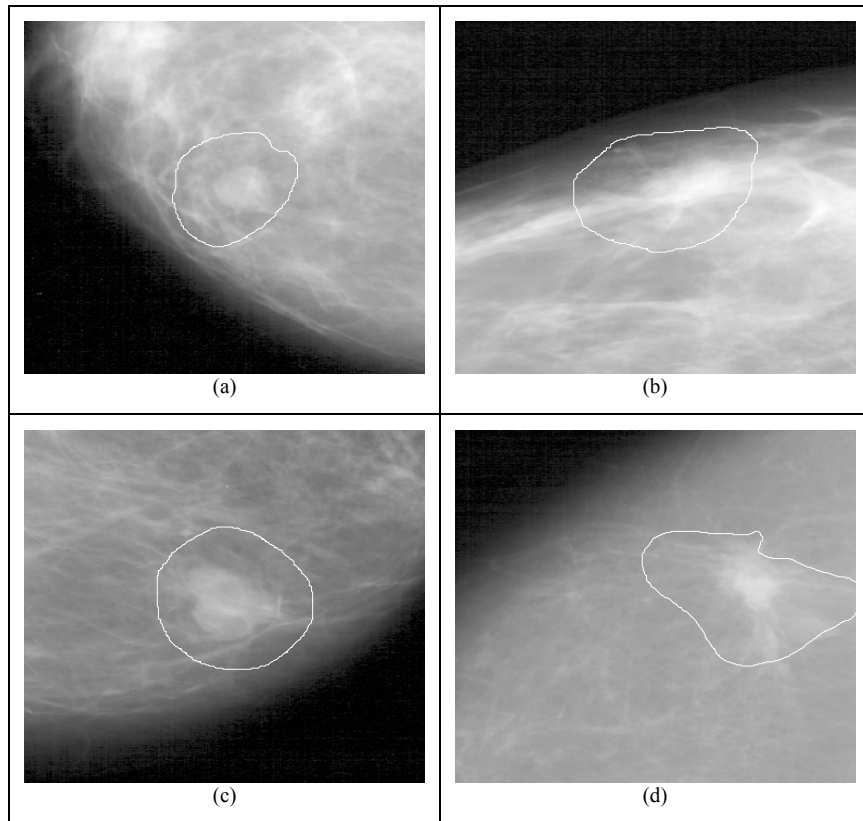


Figure 11 Examples of masses with different shapes

(a) Round. (b) Oval. (c) Lobulated. (d) Irregular.

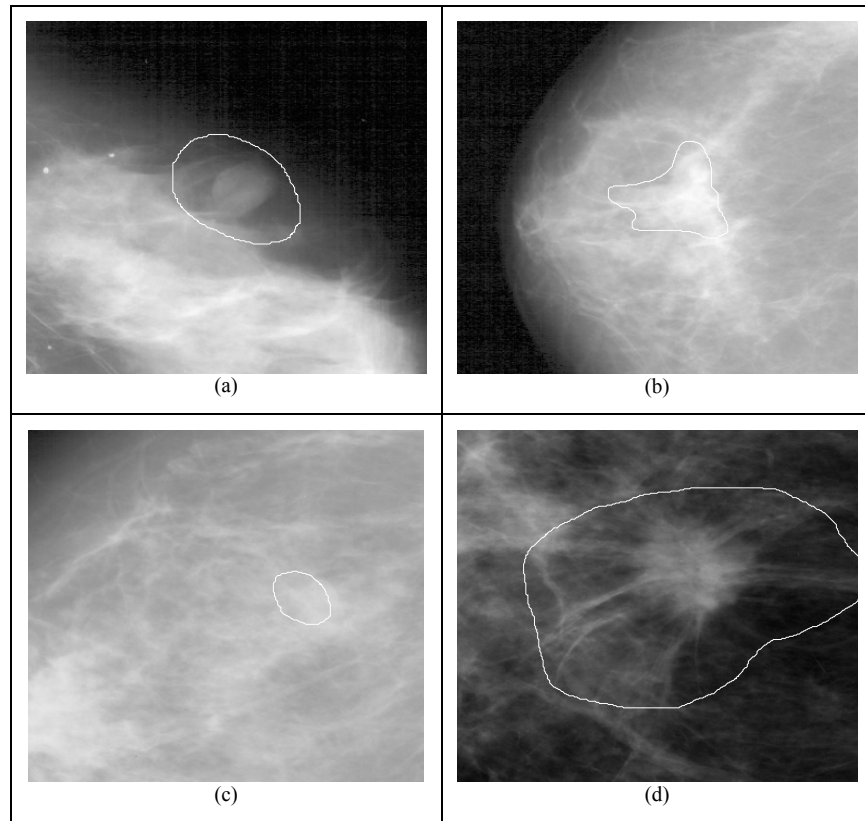


Figure 12 Examples of masses with different margins

(a) Circumscribed. (b) Ill-defined. (c) Obscured. (d) Spiculated.

## 5.2 Case Study from DDSM

For this dissertation, a subset of the DDSM database consisting of 60 test cases is selected. This data subset contains 30 benign and 30 malignant cases, where 17 of the 30 malignant cases are spiculated, and none of the benign cases are spiculated. Table 5 lists the benign and malignant cases in the study dataset.

Table 5 Listing of case numbers for the DDSM database

Benign Cases	Malignant Cases
1305, 1370, 1371, 1372, 1379, 1387, 1389, 1394, 1397, 1408, 1432, 1442, 1443, 1445, 1447, 1453, 1459, 1498, 1512, 1518, 1519, 1554, 1556, 1560, 1566, 1607, 1615, 1679, 1682, 1691	1112, 1132, 1134, 1144, 1147, 1149, 1155, 1156, 1157, 1163, 1168, 1171, 1182, 1215, 1237, 1252, 1262, 1263, 1404, 1468, 1533, 1534, 1537, 1558, 1574, 1622, 1665, 1726, 1827, 1999

Examination of Figure 13 - Figure 17 show that the DDSM-database cases chosen comprise a relatively difficult database in terms of preprocessing, segmentation and classification. Figure 13 shows the ACR density-rating distribution for the test dataset. The ratings are assigned by radiologists who worked on the DDSM database [75]. The density rating is an integer from one to four, where a density rating of one is the least dense, and a density rating of four is the most dense. In general, the higher the density rating, the more difficult segmentation may be because of increased paucity of adipose tissue, which provides mammographic contrast [123]. Figure 13 shows that most of the malignant tumors have density values two and three, while the benign tumors have density three and four. Also, there are mammograms for each density category, from one to four. Therefore, density is probably not a good feature for distinguishing malignant from benign cases. Figure 14 shows the ACR Bi-RADS [124] assessment distribution. The assessment categories and meanings are shown in Table 4. This figure indicates that this dataset is a difficult one, since a large number of the benign cases appear in category 3. Figure 15 shows the subtlety-ratings distribution [75]. A subtlety rating of one indicates least subtle, while a rating of five is the most subtle. Please note that this subtlety-rating system is unique to the DDSM database, and is different from other subtlety-rating systems used in digital mammography. A case with a DDSM subtlety rating of  $N$  is  $N$  times more subtle than a case with a subtlety rating of one. There are 4 benign and 15 malignant mammograms whose subtlety is 5 (the most subtle). There are 24 out of 30 benign cases and 27 out of 30 malignant cases which have a subtlety rating from 3 to 5. This figure shows the database is difficult.

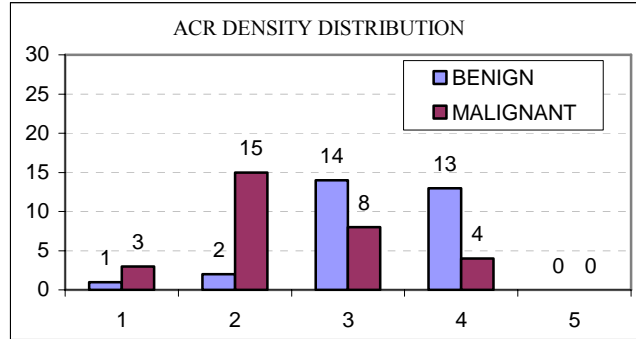


Figure 13 Case study breast density distributions

The least dense is 1 and the most is dense is 5.

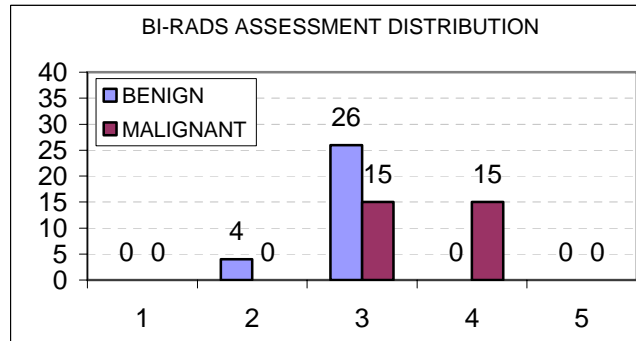


Figure 14 Case study Bi-RADS assessment category distribution

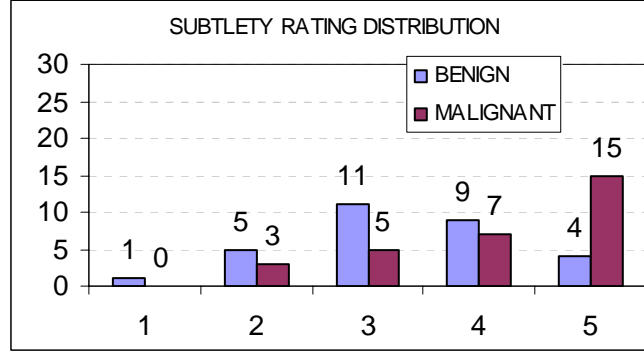


Figure 15 Case study DDSM subtlety rating distribution

Ratings range from 1 (least subtle) to 5 (most subtle).

It is well-known that mass shape plays a very important factor in mammographic analysis. Figure 16 shows the shape distribution. The shape keywords are defined in Table 6. The shapes are assessed by experienced radiologists. As expected, almost all irregularly shaped masses are malignant, while oval and round shapes are benign. Figure 17 shows the margin-keyword distribution. The margin keywords are defined in Table 7. The margins are assessed by experienced radiologists. As expected, the masses with spiculated margins are cancerous, while a majority of the ill-defined margins are malignant. All circumscribed and obscured margins are benign cases. From this figure, 18 of the cases are ill-defined and 15 are obscured, again showing the difficulty of the dataset.

Table 6 Shape keywords and their meanings

Keyword	Meaning	Keyword	Meaning
Oval	Shaped like an oval.	Lobulated	Shaped like breast lobes.
Irregular	Irregular shape.	Round	Circularly shaped.

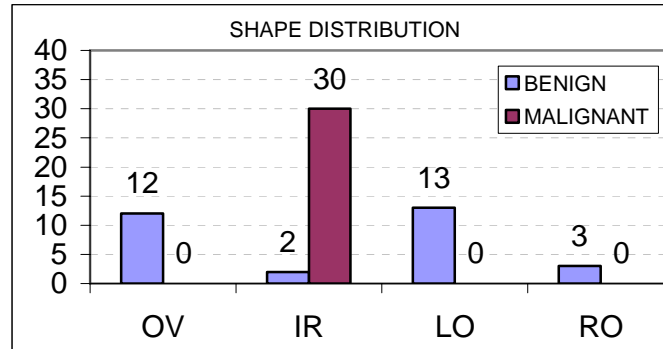


Figure 16 Case study shape distribution

Legend: OV= Oval, IR = Irregular, LO = Lobulated, RO = Round.

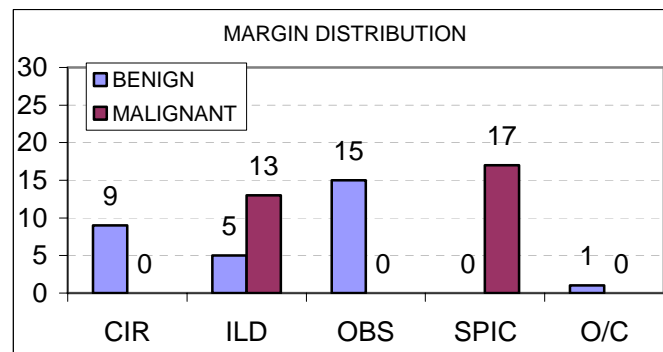


Figure 17 Case study margin distribution

Legend: CIR = Circular, ILD = Ill defined, OBS = Obscured, SPIC = Spiculated, O/C = Obscured and Circumscribed.

Table 7 Margin keywords and their meanings

Keyword	Meaning
Circular	Shaped like a circle.
Ill defined	Margins are not well-defined.
Obscured	Part of margin is not visible.
Spiculated	Has radiating lines from the main mass. These masses are also called stellate masses [103].
Circumscribed	Well localized mass, which typically has completely or partially well-defined borders [75].

### 5.3 Tumors

Tumors present as medium-gray to white areas on digital mammograms [75]. In the breast, adipose tissue is more radiolucent than glandular and fibrous tissue, and thus provides contrast in mammography [75]. According to Egan, the primary signs of carcinoma are related to properties of the tumor mass such as the mass density, shape, borders and whether the tumor is spiculated [75]. Egan further points out that malignant masses typically have irregular and spiculated contours, and circumscribed masses, which in some areas may have well-defined borders [87]. According to Andolina *et al.*, most cancerous masses are more dense than surrounding tissue, and the tissue composition of a mass can be an important indicator of malignancy [105].

#### 5.3.1 Image-Enhancement Techniques

Mammograms often have poor contrast and need specialized noise reduction and image enhancement in order for the CAD system to be able to perform well [125]. There is an abundance of research on mammographic-image preprocessing, using techniques such as gamma correction, adaptive 2D Wiener filtering, contrast-limited adaptive histogram equalization (CLAHE), fuzzy graylevel enhancement, multi-scale wavelet-based enhancement, and 2D isotropic Gaussian filtering. There is clearly no single best method for image enhancement, and the enhancement often depends on the segmentation algorithm [1].

Gamma correction is a well-known image-processing technique and is described in [126]. Baeg and Kehtarnavaz [22] used gamma correction for mammographic enhancement. Based on their texture-analysis method, classification of 150 biopsy-proven masses into benign and malignant classes resulted in ROC  $A_z = 0.91$ . Ball, Butler, and Bruce [16] also used gamma correction for mammographic-image enhancement on the DDSM database [127]. Gamma correction is simple but the effects are localized and not global.

The adaptive 2D Wiener filtering (A2DWF) noise-reduction algorithm [128] estimates the noise in the neighborhood around each pixel and then adjusts the surrounding region based on that noise estimate. Mayo, Rodenas, and Verdú [125] compared A2DWF, a wavelet filter, a filter based on independent component analysis, and finally, a filter based on the diffusion equation. Although they did not extract features, the noise-removal aspects of the methods are similar based on visual observation and mean square error.

Pisano *et al.* [129] examined several digital mammograms using multiple methods of enhancement, including CLAHE. They concluded that image detail is good and, in general, that lesions appeared obvious compared to the background. They also found graininess introduced due to enhancement of image noise, which might mislead a radiologist to thinking that there are false microcalcifications. An advantage of CLAHE is that it is straightforward to implement and runs fairly quickly.

Mekle, Laine, and Smith [130] used an interactive multi-scale enhancement which incorporates dyadic spline wavelet functions and sigmoidal nonlinear enhancement functions. This method yielded improved diagnostic performance in a national mammography database prepared by the University of South Florida and Harvard Medical School. In a similar approach, Sakellaropoulos, Costaridou, and Panayiotakis [131] developed a system for mammographic-image denoising and contrast enhancement based on nonlinear modification of wavelet coefficients with an adaptive soft-thresholding function, followed by wavelet image reconstruction. Laine, Fan, and Yang [1] developed a methodology for image contrast enhancement by using wavelet transform coefficients modified with a nonlinear function followed

by wavelet image reconstruction. The one drawback of these methods is selection of the proper mother wavelet or thresholding parameters may not be an easy task.

Some noise can be removed from an image by lowpass filtering. One common approach is to convolve the image with an isotropic 2D lowpass filter. A Gaussian kernel has the special property of its Fourier Transform also being a Gaussian [132], and therefore there are no artificial bright or dark spots due to ringing are created in the convolved image after filtering with the Gaussian kernel. In contrast, a simple hard-edged lowpass filter will produce ringing because of the sinc-function nature of the Fourier transform of the filter. Moreover, lesions tend to be compact and convex [45], therefore a Gaussian filter is a good choice for filtering mammographic lesions. Bottigli and Golosio [132] used an enhanced image created by convolving the original image with an isotropic 2D Gaussian kernel which has an experimentally determined variance. They utilized level sets, and their speed function incorporated a term containing a power of the image gradient. Kupinski and Giger [17] also enhanced the images prior to segmentation by convolving the original image with an isotropic 2D Gaussian kernel, where the variance of the kernel is experimentally determined. This method is easy to implement using a fast Fourier transform. However, this method assumes that masses are Gaussian shaped and isotropic, which may not be the case.

### 5.3.2 The Rubber Band Straightening Transform (RBST)

The rubber band straightening transform (RBST) is a special method developed specifically for digital mammography by Sahiner *et al.* [75,133]. In the RBST, pixels around a segmentation border are remapped into a rectangular two dimensional array in order to allow features to be extracted from the RBST image. It is well-known in mammography analysis that mass-border characteristics are very important in determining malignancy [75,80] and that many cancerous masses exhibit a desmoplastic response to the surrounding tissue, which alters the normal breast patterns near the mass [134]. Therefore, features derived from the RBST may be important features to determine malignancy.

The RBST algorithm first determines all of the pixels on the image border, and next numbers those pixels by walking around the border in a clockwise fashion, and assigning an incrementing pixel label to each new pixel. Note that some pixels may be assigned more than one pixel label, because the segmentation may contain small areas of one-pixel width extending from the main segmentation area.

An offset parameter,  $K$ , controls estimation of the border normal at each point by determining which previous and following border pixels to use to estimate the normal. Let  $(i_k, j_k)$  be the coordinates of the  $k$ -th border pixel and let  $p(k)$  and  $n(k)$  be the index of the pixel that is  $K$  pixels before (the previous pixel), and  $K$  pixels after (the following pixel) the current pixel, respectively. The coordinates of the previous and following pixels are given by  $(i_{p(k)}, j_{p(k)})$  and  $(i_{n(k)}, j_{n(k)})$ , respectively. The line that joins these two pixels is used to determine the normal to the current pixel by finding the perpendicular extension to that line which is in the direction leaving the mass. Figure 18 shows an example case with parameter  $K = 1$ , where the normal vectors for points 6 and 12 are shown.

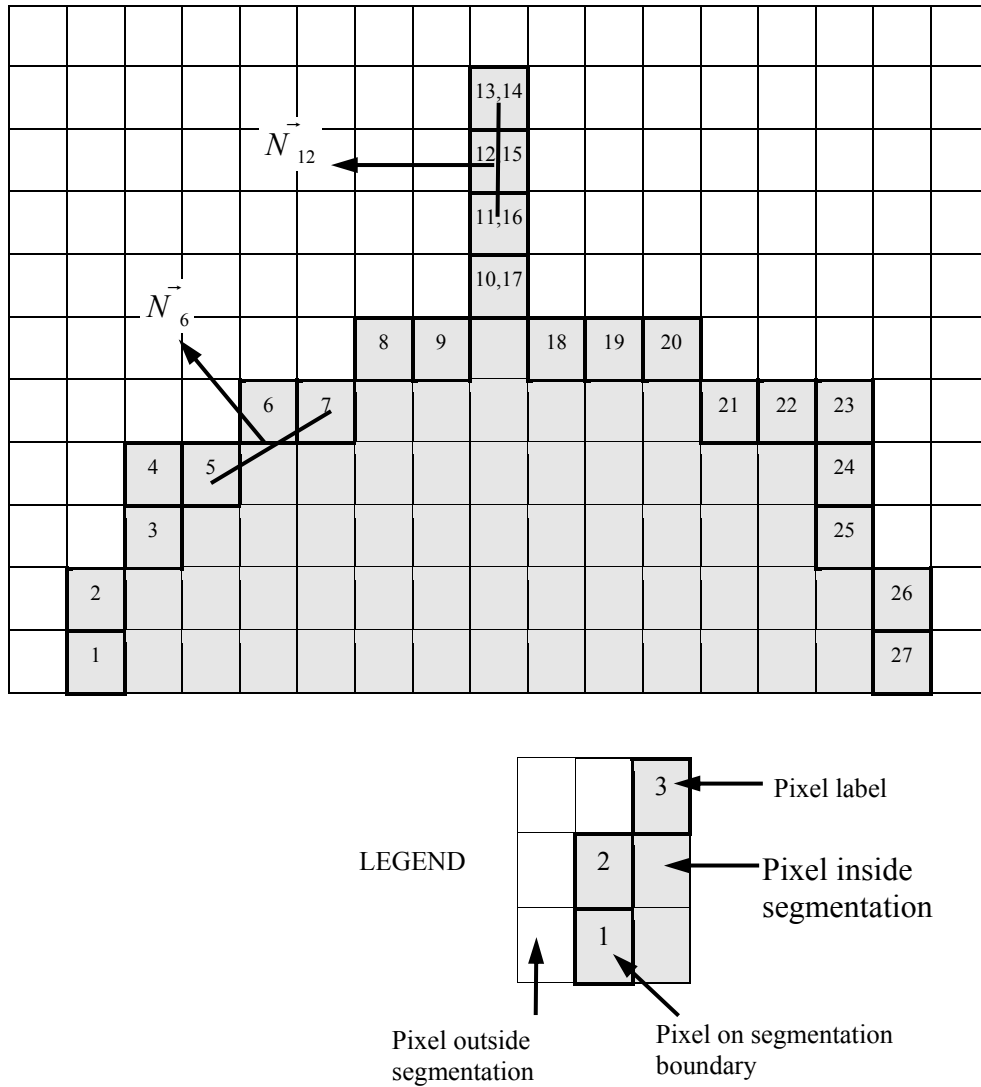


Figure 18 Example showing the normal vectors for several points in the RBST

Two other parameters are used to control the radial distance used in evaluating the RBST transform. The user selects two radii,  $R_{OUT}$  and  $R_{IN}$ , which correspond to how far radially outward and inward, respectively, from each border pixel that the RBST image will reach. The RBST is then generated by starting at  $R_{IN}$  pixels inside the border, and traveling normally to the border and outwards to  $R_{OUT}$  pixels away, and placing the pixel graylevel encountered at these locations in the RBST image. Therefore, if there are  $N_b$  boundary pixels, the RBST image will be

a 2D matrix sized  $(R_{OUT} + R_{IN} + 1)$  rows by  $N_b$  columns. Figure 19 (a) shows an example case with a segmentation of the mass shown as a black line. Figure 19 (b) shows the area where the RBST is extracted from the image. Figure 19 (c) shows the RBST image. In this example, the inward and outward radii are  $R_{OUT} = 40$  and  $R_{IN} = 40$ , respectively, and the normal parameter  $K = 20$ .

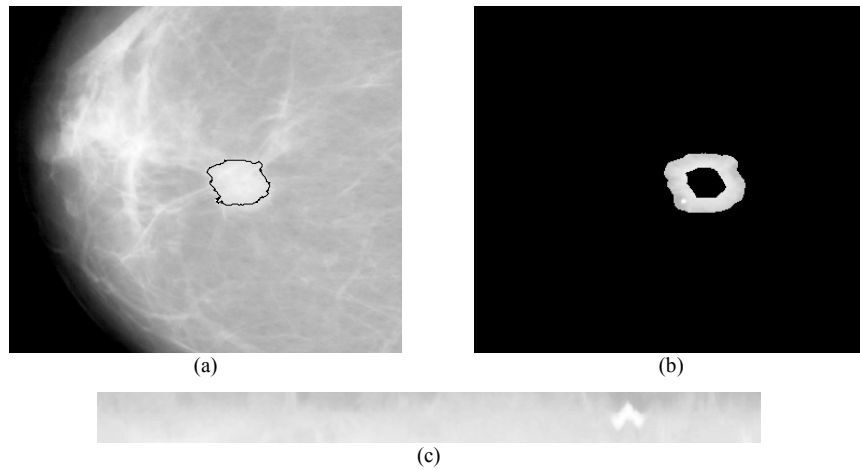


Figure 19 Example case showing a mass segmentation, the area of the RBST, and the RBST image

(a) Mammogram showing mass boundary in black. (b) RBST preimage in the original mammogram. (c) RBST image.

### 5.3.3 Image-Segmentation Techniques

There are a large number of image-segmentation techniques in digital mammography, including morphological processing, statistical thresholding, level sets, bilateral image-pair subtraction, multi-resolution analysis, and specialized filtering.

Baeg *et al.* [2] used morphological texture features to segment mammograms. This system is intended to be a second opinion to radiologists. In this approach, morphological erosion and dilation are carried out in an iterative manner, and the volumes of the opened or closed images change as the structuring elements are increased in size. Based on the changing volumes, a

probability density function called the pattern spectrum is generated, and features are derived from the moments of the pattern spectrum. The Karhunen-Loève transform (KLT) is applied to these texture features, and  $K$ -means clustering is performed to separate regions into skin, fat, fibroglandular tissue, adipose tissue, etc. The main drawback to this approach is that the KLT projects the feature vectors by ordering them in decreasing variance [2]. The KLT is optimal for least mean square coding [22], but may not be optimal for classification.

Ball, Butler, and Bruce [135] used graylevel image statistics to segment mammographic masses. Calder *et al.* [136] used statistical models to segment masses. Christoyianni, Dermatas, and Kokkinakis [137] used statistical segmentation and radial-basis neural networks to segment masses. Catarious *et al.* [137] used iterative pixel graylevel thresholding based on the optimal Fisher's LDA threshold of pixels inside the current region versus pixels outside of the region. The main drawback of statistical segmentation is that the segmentation can be confused by areas outside of the mass which look similar, and thus the segmentation can oversegment easily. Ball, Butler, and Bruce had this issue in some of their cases. Catarious' assumption that the optimal Fisher's threshold to separate two datasets will provide the optimal graylevel threshold for segmenting masses in digital mammograms [138] is not true in general. The algorithm tends to work well when the mass exhibits high contrast compared to the background, but tends to severely oversegment mammograms where the background has similar characteristics to the mass. This behavior will be demonstrated in chapter VIII.

Beller *et al.* [45] segmented stellate (spiculated) lesions using local features and an interactive radiologist system. In this method, a radiologist extracts example regions corresponding to a mass and corresponding to background. The whole image is segmented, and this process is repeated until the radiologist is satisfied with the results. The aforementioned process is repeated on many mammograms. The overall lesion detection rate is 70%. The main issue with this approach is that selecting only one background area may not be sufficient for characterizing the very complex nature of digital mammograms.

Bottigli and Golioso [4] used level sets with the fast marching algorithm to segment lesions. The fast marching implementation is numerically fast, but only allows the segmented region to grow outward [139]. They used a gradient-based stopping term to control the segmentation. The main issue with this method is that mammograms are very noisy, and often mass borders are ill-defined or obscured; therefore, a gradient-based stopping term is inappropriate. This method may only work well for mammograms with a bright central mass with clear borders surrounded by adipose tissue.

Bovis and Singh [75] used bilateral subtraction of breast image pairs. It is well-known that asymmetry between breasts can be indicative of a malignant process [140]. The main drawback to this approach is the difficulty in accurately registering the two breast images.

Brzakovic, Luo, and Brzakovic [141] identified pixel groupings that might correspond to tumors by using fuzzy pyramid linking and multi-resolution analysis. The algorithm, termed automated mammogram analysis (AMA), is found to be good at detecting regions which warrant further analysis, and less successful at target recognition. AMA is therefore a tool more useful for prompting radiologists to aid in identifying possible trouble spots. The images are sized  $256 \times 256$  due to equipment limitations, which is a very small image for mammographic analysis.

Campanini *et al.* [122] used a support vector machine-based segmentation to detect masses. Mammograms from the MIAS database [142] are analyzed using physician-supplied ROI as a basis for analysis. Their algorithm detected 80% of cancers with 1.1 false positives per image (FPPI). Cao *et al.* [143] used a vicinal support vector machine and a clustering algorithm which extended previous work by Vapnik [144] to segment malignant masses. They achieved around 85% overall accuracy with corresponding  $A_z = 0.89$ . The algorithm is found to be sensitive to the ROI and to the number of clusters.

Guliatto *et al.* [145] used seed pixels and fuzzy region growing based on statistical measures to segment masses. This method uses a fuzzy membership function based on the region homogeneity defined by analysis of the region mean, standard deviation, and the coefficient of variation, which is defined as the standard deviation divided by the mean. The main drawback of

this approach is that tumors without a dense (i.e. white area on the mammogram) core area are not detected. The algorithm did work well when the malignant masses did have a bright core.

Gupta and Undrill [146,147] used texture analysis to segment masses. Features derived from Laws texture features [132] are used to segment suspicious masses. This is a preliminary study, and the results are promising.

Kupinski and Giger used the radial gradient index (RGI) and probabilistic methods to segment suspicious masses [105]. The RGI measures how much of each border gradient is pointed in the direction normal to a line extending from the mass centroid. The RGI method also preprocesses the mammograms with an isotropic 2D Gaussian filter, which assumes the masses are distributed in this manner. This method is known to be sensitive to noise [148]. The probabilistic method used integration of a PDF to obtain a better segmentation, but this integration is tedious and computationally expensive. The probabilistic method provided better segmentations than the RGI method.

Székely and Pataki [149] modified the RGI by adding a border-length penalty term. They combined this method with previous work from Székely *et al.* [150] and Székely and Pataki [148]. The method used Bézier histograms and dual binarization techniques along with the modified RGI to segment masses. The RGI method with the addition of the proposed penalty term from [132], as well as the original RGI method from [151] are implemented. In some initial studies, it was found that the modification did not seem to make much difference in the study dataset, and perhaps the combination of all techniques used by Székely and Pataki is required to see improvement over the RGI alone.

There are several approaches that use adaptive or specialized filtering. Lai, Li, and Bischof [152] used modified median filtering and template matching to detect circumscribed masses. The algorithm detected all masses, but there is only one mammogram in the test set which did not have any masses. The main drawback to this method is that it is very computationally intensive, even with only twelve templates to match. Pfisterer and Ahdasi [153] investigated four texture-based algorithms for mass detection and found that the steerable filter approach gave the

best results for mass detection. The algorithms are analyzed on images from the DDSM database. The best results are 73.7% TPF at 3.04 FPPI. The results are preliminary in that the authors suggested several improvements that could be made. The results showed lower accuracy than other current methods.

Heath and Bowyer [9] used a moving filter analyzing graylevel decay at different scales to locate suspicious masses. Using a subset of mammograms from the DDSM database, they obtained 90% TPF at around 8.0 FPPI, and 60% TPF at around 1.0 FPPI. This method is simple to understand, code, and runs quickly. It can find suspicious masses in digital mammograms without relying on a physician-supplied ROI. They also achieved good results on the MIAS database, indicating that the algorithm is not overly tuned to the DDSM dataset.

Kobatake *et al.* [113,116] used an adaptive iris filter and parameterization of region border statistics to distinguish malignant from benign tumors. This is a small preliminary study with promising results. One potential drawback is the adaptive iris filter has a circular region of support, which assumes a circularly shaped tumor.

#### 5.4 Spiculations

Spiculations present in digital mammograms as nearly linear filaments extending from the mass periphery [117], and grow somewhat linearly within  $\pm 45^\circ$  normal to the mass boundary [104]. Spiculated lesions are also called stellate lesions because of their star-shaped appearance. According to Tabár and Dean, spiculations of scirrhous carcinomas usually present as sharp, dense, fine lines radiating in all directions, and spiculations of sclerosing duct hyperplasia present as fine, low-density bunches (like a broom) [120].

Jeske, Bernstein, and Stull [113] and Winchester and Winchester [120] state that “the classic mammographic presentation of infiltrating ductal carcinoma is a high-density mass with spiculated margins”. Based on these expert observations, spiculation presence is a very important clue in analyzing digital mammograms. Jeske, Bernstein, and Stull state that the presence of irregularly shaped masses and spiculations increase the probability of malignancy [113].

According to Winchester and Winchester, mammographic-mass analysis is based on the mass shape, margins, and density, and masses with irregular shapes or spiculations increase the probability of malignancy [154]. Bennett *et al.* show that a poorly marginated, spiculated mass has a 74-percent positive predictive value for breast cancer if it is non-palpable, and a 99-percent positive predictive value for breast cancer if it is palpable [117].

In general, spiculation segmentation is difficult because (1) spiculations are often ill-defined and have poor contrast [75,155], (2) the lack of adipose tissue in young breasts can make spiculation detection difficult [116], and (3) normal breast tissue, such as ligaments, ducts, or blood vessels, often appear as a criss-crossing set of linear structures [156]. Figure 20 shows mammograms of several cases from the DDSM database that have a spiculated mass. The spicules can be seen as small, filament-like appendages extending from the main central mass.

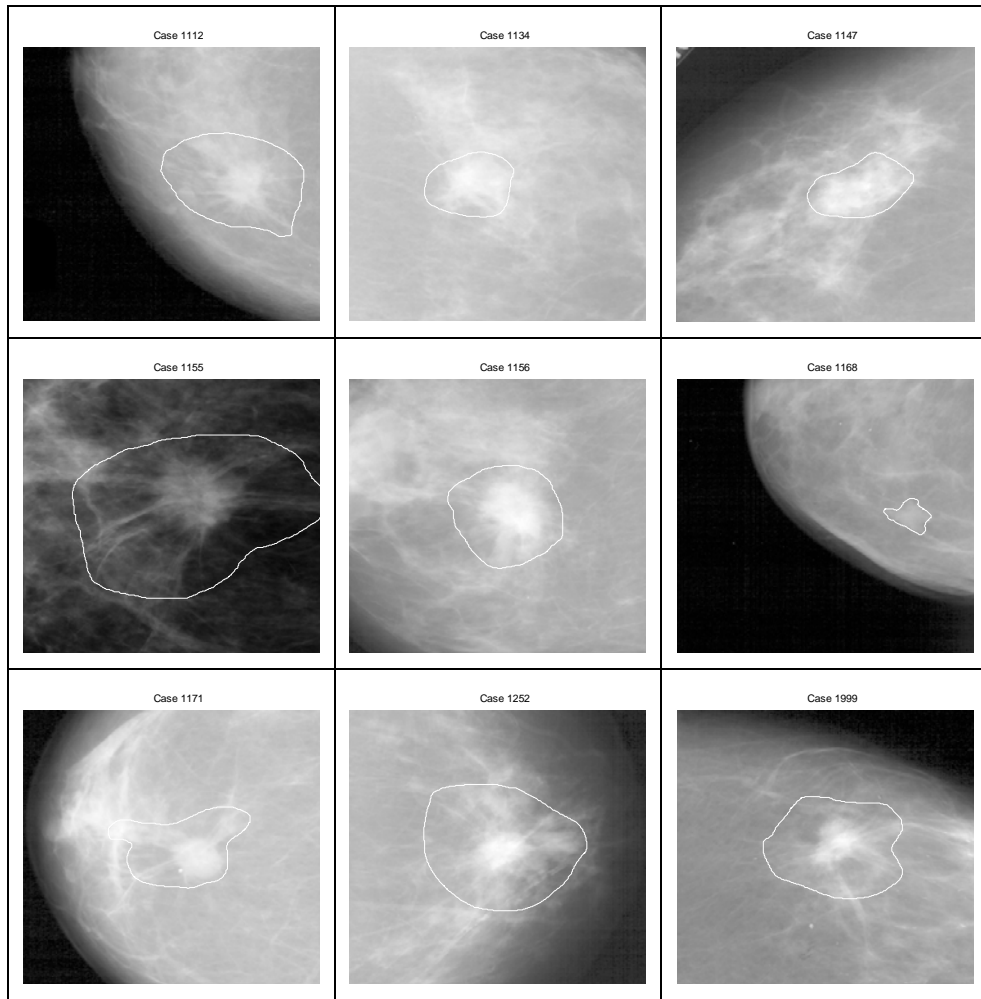


Figure 20 Several DDSM cases which contain spiculated masses

#### 5.4.1 Image-Enhancement Techniques

Spiculation image-enhancement techniques attempt to enhance the images in order to locate spicules, which appear as fine light-gray to white lines on the mammograms. These techniques include using transformations such as the Radon transform, DWT analysis, statistical methods, gradient analysis, morphological operations, recursive filtering, and CLAHE.

Sampat and Bovik [157] used a continuous Radon transform in order to obtain line enhancement. The Radon transform maps lines in an image into points in the transformation domain. Linear filtering is performed in the radon domain, and then a threshold is applied to the

image. The resulting image is then inverse-transformed back into the Cartesian domain, which supplies an image with linear structures enhanced. The results are presented for only three mammograms, so the method is preliminary.

Karssemeijer and te Brake [158] used a statistical method based on pixel orientations to identify spiculated areas. Using scale-space theory and three second-order oriented Gaussian derivative filters, their method creates a map which provides an estimate of the pixel orientations. One advantage of this method is that it requires that the image need to be processed using only three directional filters. A second advantage is that using a second-order Gaussian eliminates the problems of detecting lines of one-pixel width, which are problematic for first-order Gaussian filters. A disadvantage is the high level of noise in mammographic images which can degrade the results.

Jiang *et al.* [159] used morphological operations and specialized graylevel features to detect spicules. Using iterative erosion, the image is dilated iteratively until convergence is reached. In this analysis, four three-pixel linear structuring elements are used, where each is at a different orientation. A morphological top-hat operation and then a morphological opening operation are applied to suppress noise, using eight linear structuring elements, which are 20 pixels long, one pixel wide, and have  $22.5^\circ$  rotation between each element. A direction map is then created from the processed image. The method is fairly simple, and was tested on 24 mammograms, of which seven are spiculated.

Kobatake and Yoshinaga [160] used morphological processing and a modified Hough transform to detect spiculated regions. A morphological skeleton is created and a Hough transform is used, which can detect a line by counting the number of curves at a point in the  $\rho, \theta$  plane, where  $\rho$  and  $\theta$  are polar coordinates used in the Hough transform. The modification is to detect two line segments, which corresponds to a spicule exiting a mass at an angle  $\theta_1$  relative to the centroid, and another spicule exiting at angle  $\theta_1 + \pi$ . A highly spiculated mass could exhibit

characteristics such as these. The main drawback to this method is the extensive processing required to perform morphological operations and to evaluate the Hough transform.

Kegelmeyer *et al.* [146,147] used analysis of local-gradient histograms to detect spiculated areas. The analysis of local-oriented edges (ALOE) algorithm is used to preprocess the image. A subset of Laws texture measures [161] previously shown to perform well in digital-image texture analysis [162], is employed in order to create a probability image, where each pixel contains the probability that that pixel is located in a suspicious mass. The results are very promising, and it is shown that a statistically significant increase in radiologist screening efficacy is attributable to this system. It is noted that the malignant images in the dataset are all spiculated. That is, there are no malignant cases that are not spiculated. They also pointed out that, by using only the ALOE features, most spiculations are detected, but too many false positives (FP) are also detected. By adding the Laws texture features, the system achieved a much lower FP rate.

Liu, Babbs, and Delp [163] used a 2D wavelet transform to enhance images for spiculation detection. They employed a linear-phase nonseparable 2D wavelet and generated feature images at several resolutions coarser than that of the original image using a quincunx lattice. This implementation allows them to use small filters to search large areas because of the multi-scale nature of the wavelet transform. They analyzed images from the MIAS database and were able to detect lesions of different sizes at low false-positive rates.

Zwiggelaar, Astley, Boggis, and Taylor [23] compared the following methods for mammogram-spicule enhancement: (1) the Dixon and Taylor Line Operator (DTLO) [164], originally proposed by Dixon and Taylor for asbestos counting, (2) oriented-bins analysis of Zwiggelaar, Parr, and Taylor [157], (3) a method proposed by Karssemeijer based on Gaussian derivatives [165] which is described above, and (4) a ridge detector by Lindeberg [23]. From their analysis, they chose the DTLO line operator because it provided the best signal-to-noise ratio, the best localization, line-width accuracy, and was only marginally worse than the oriented-bins method for orientation accuracy. It is noted that increasing the DTLO line-detection foreground kernel is suggested, but instead multi-resolution analysis is performed by keeping the kernel static

and using Gaussian filtering and subsampling the images. They achieved  $A_z = 0.746$  for classification of subtle spiculated masses, which is low, but this is achieved on a difficult dataset.

The DTLO [163] spiculation image-enhancement methods in Zwiggelaar *et al.* [166] will be used in Chapter VII, and therefore will be discussed in detail. The DTLO algorithm produces a line-strength map,  $S$ , indicating the potential presence of oriented lines. This method is originally developed to detect asbestos fibers. DTLO requires two parameters:  $K$ , which controls how many angular orientations are analyzed, and  $M$ , the line length parameter, and the method is denoted by  $DTLO(K,M)$ . For instance if  $K=12$  and  $M=5$ , then the set of angular displacements is  $\theta \in \{0^\circ, 15^\circ, \dots, 165^\circ\}$ , which divides the upper half plane into twelve divisions, and the line length is five pixels. The DTLO algorithm works as follows. Let  $\Omega$  be the image region of support. At each pixel  $(x, y) \in \Omega$ , the DTLO algorithm measures the line strength  $S(x, y)$  by calculating the contribution of the foreground minus the contribution of the background. Sample DTLO masks are shown in Figure 21.

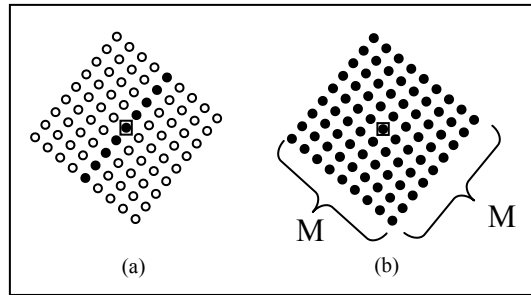


Figure 21 Dixon and Taylor Line Operator (DTLO) masks

DTLO masks are shown in (a) and (b). All masks shown for angular offset of  $\pi/3$  radians. (a) DTLO foreground mask. (b) DTLO background mask. The Pixel being evaluated is marked by square. Black and white circles are on and off pixels in the mask, respectively. The sum of the on pixels is one. The line length  $M=9$  is shown.

The foreground and background masks are shown in Figure 21 (a) and (b), respectively. In this figure, each black circle represents an “on” pixel, and each on pixel has a value of  $1/M$  in the foreground mask, and  $1/M^2$  in the background mask. The white circles are “off” pixels, and are zero valued.

For each angle  $\theta \in \Theta$ , the foreground mask has a line of length  $M$  and width one pixel, oriented at the angle  $\theta$ . The foreground value,  $F(x, y, \theta)$ , is the sum of the pixel values multiplied by the corresponding foreground mask values. Similarly, the background mask is a rectangle of size  $M \times M$ , oriented at the angle  $\theta$ . The background value,  $B(x, y, \theta)$ , is the sum of the image pixels multiplied by the corresponding background mask elements. The line-strength image value,  $S(x, y)$ , is calculated by

$$S(x, y) = \max_{\theta \in \Theta} \{F(x, y, \theta) - B(x, y, \theta)\}. \quad (5.1)$$

Local linear structures which have good contrast and also match the foreground mask will have high values in the line-strength map. Bilinear interpolation is used to create the rotated image for non-zero angles. In order to avoid unnecessary computations, the line-strength map is calculated in only a square image of size  $1200 \times 1200$  pixels ( $52.2^2 \text{ mm}^2$ ) centered at the mass seed point, which is selected automatically in [122]. If the seed point is close to the mammogram border, then the image is padded with zeros.

Zwiggelaar *et al.* used DTLO(12,5), which has 12 angular divisions ( $15^\circ$  displacements) and a line length of 5 pixels (0.25 mm) to analyze synthetic images and images from the MIAS database [167] with spatial resolution of 50  $\mu\text{m}$ .

Parr *et al.* [125] used a multi-scale oriented line detector which provides estimates of the line strength, orientation, and scale. They then applied factor-analysis to separate the random portion of the data from the signal portion. Directional recursive median filtering is then applied with oriented pattern factor-analysis models for the linear structure distortion caused by a spiculated lesion. They obtained a sensitivity of 70% at 0.01 FPPI.

Pisano *et al.* [125] analyzed several image-enhancement techniques, and stated that CLAHE "... might be helpful in allowing radiologists to see subtle edge information, such as spiculations" [15]. CLAHE by itself is probably not adequate for a spiculation-detection system, but does provide good enhancement in general.

#### 5.4.2 Spiculation-Detection Techniques

Several different spiculation-detection techniques have been developed and are presented in the literature. These techniques are discussed below.

Bruce and Adhami [156] used features derived from the wavelet modulus-maxima method to classify mass shapes as round-stellate, round-nodular, and nodular-stellate. This method provided excellent results. Some of the features such as the Lipschitz exponent are very difficult to properly evaluate, and care must be taken to meet the assumptions required for application of the method.

After applying a continuous Radon transform to perform line enhancement, Sampat and Bovik [162] then applied custom radial spiculation filters to detect spiculated areas. This algorithm is fairly easy to implement, but is tested on only three mammograms, and thus the results are unproven.

Liu, Babbs, and Delp [168] used a 2D wavelet transform to enhance images for spiculation detection. They employed a linear-phase nonseparable 2D wavelet and generated feature images at several resolutions coarser than the original image using a quincunx lattice. Features derived from the wavelet decomposition include mean pixel brightness, standard deviation of pixel brightness, standard deviation of gradient-orientation histograms, and standard deviation of the folded gradient-orientation histograms. A folded gradient orientation is used in order to calculate the standard deviations independent of the nominal angle values.

Zwiggelaar, Astley, and Taylor [167] used multi-scale directional recursive median filtering (RMF), principal components analysis, and an artificial neural network to detect the central mass of a spiculated lesion. Parr *et al.* [169] used directional RMF with oriented pattern

factor-analysis models for the linear structure distortion caused by a spiculated lesion. Parr's algorithm achieved 100% sensitivity at 10 FPPI and around 50% sensitivity at 1 FPPI.

#### 5.4.3 Spiculation-Segmentation Techniques

Although there are numerous techniques for main mass (periphery) segmentation, there are relatively few spiculation-segmentation techniques. Some of the proposed techniques include region growing, skeleton analysis, and image-gradient statistical analysis.

Giger *et al.* [158] used region growing with an experimentally determined stopping criteria, and extracted two features based on comparison of a smoothed lesion boundary with the original lesion boundary, and on the differences between the areas of the original lesion and the lesion after morphological processing. A neural network classifier is used to analyze the features.

Jiang *et al.* [160] used morphological spiculation image enhancement followed by direction-map analysis and extraction of specialized graylevel features to detect spicules. Kegelmeyer *et al.* [146,147] examined neighborhoods of every pixel. A binary decision tree classifier was constructed based on features extracted from each pixel, which included Laws texture-energy features [117] and analysis of local oriented edges. This system is intended to be a second reader CAD system used to assist radiologists in mammographic analysis.

Several authors have used analysis of image gradients. Chan *et al.* [170] and Sahiner *et al.* [171] used a search region outside of the mass periphery and used a custom spiculation measure to create a 2D spiculation likelihood map. From this map, an experimental threshold is used to segment one pixel of the suspected spiculated area. This process is repeated 30 times (which creates a 3mm band) in order to segment spicules. If their system classified the mass as spiculated, the spicules are added to the periphery. For each point on the boundary of the mass periphery, the algorithm utilized a circular wedge-shaped search region with radius of 4 mm, with the apex of the wedge located at a given point on the mass periphery, and the wedge size defined by  $\pm 45^\circ$  from the normal to the mass boundary,  $\bar{n}_c$ , where  $c$  indicates the  $c$ -th point on the

boundary. A spiculation measure,  $x(i_c, j_c)$ , is calculated for each point  $(i_c, j_c)$  on the mass periphery. The spiculation measure is the average of the acute angle between  $\vec{n}_c$  and the angle of the image gradient at each point in the search wedge. A final post-processing step removes areas disjoint from the main mass.

Goto *et al.* [117,170] used a similar spiculation search, and called their search area a pendulum filter. They used the pendulum filter to search a wedge-shaped area, segmented the spicules that fell in the pendulum filter region of support, and then repeated this process two more times. Their segmentation also used the image gradients, but segmented a linear subset of the spicules instead of one pixel at a time as done in [105].

## 5.5 Features

This section discusses the various types of features which are typically used in mammography analysis [12]. The type of features include patient information, statistical features from the pixel graylevel values, textural features, normalized radial-length (NRL) feature, based on the segmentation boundary, and morphological features based on the size and shape of the segmentation.

### 5.5.1 Patient-Information Features

It is well-known that age is the most important feature in mammographic analysis [146,147]. Therefore, in this dissertation, age will be included as a feature. The other patient information described in the previous sections will not be used in this dissertation's study.

### 5.5.2 Statistical Features

Statistical features are derived from the segmentation boundary or an extension of the segmentation boundary. The statistical features are graylevel mean value, graylevel standard deviation, and graylevel standard-deviation ratio. The standard-deviation ratio is the ratio of the

graylevel standard deviation in a region from one to 200 pixels outside of the segmentation boundary to the standard deviation of pixels inside the segmentation boundary.

### 5.5.3 Textural Features

Textural features can capture important characteristics of a small area, and thus may be beneficial in image segmentation. The textural features include graylevel co-occurrence-matrix (GLCM) features derived from the RBST image, GLCM features extracted from the segmentation boundary, and Laws texture features [1,172]. The GLCM textural features include energy, variance, correlation, inertia, inverse difference moment, and entropy [146,147]. The Laws texture features include features derived from 2D Laws texture kernels [172]. Each of these is explained in detail below.

#### 5.5.3.1 GLCM Textural Features

In order to calculate the GLCM texture features efficiently, the image is first quantized using  $N$  bins, resulting in a quantized image whose pixel values elements are in  $\{0, \dots, N-1\}$ . In this dissertation, the value for the number of quantized bins is set to  $N=20$ . Distances,  $d$ , and direction angles,  $\theta$ , are selected and the associated relative-frequency matrix  $P=[P_{ij}]$  is calculated, where  $i$  and  $j$  are the pixel intensities. Following [146,147], the following equations are used to calculate the  $P$  matrix values for the distance  $d$  and the angles  $\theta \in \{0^\circ, 45^\circ, 90^\circ, 135^\circ\}$ :

$$P(i, j, d, 0^\circ) = \# \left\{ \begin{array}{l} ((k, l), (m, n)) \in I, \\ \forall |k - m| = 0, |l - n| = d, I(k, l) = i, I(m, n) = j \end{array} \right\} \quad (5.2)$$

$$P(i, j, d, 45^\circ) = \# \left\{ \begin{array}{l} ((k, l), (m, n)) \in I, \\ \forall (k - m = d, l - n = -d) \text{ or } (k - m = -d, l - n = d), \\ I(k, l) = i, I(m, n) = j \end{array} \right\} \quad (5.3)$$

$$P(i, j, d, 90^\circ) = \# \left\{ \begin{array}{l} ((k, l), (m, n)) \in I, \\ \forall |k - m| = d, |l - n| = 0, I(k, l) = i, I(m, n) = j \end{array} \right\} \quad (5.4)$$

$$P(i, j, d, 45^\circ) = \# \left\{ \begin{array}{l} ((k, l), (m, n)) \in I, \\ \forall (k - m = d, l - n = d) \text{ or } (k - m = -d, l - n = -d), \\ I(k, l) = i, I(m, n) = j \end{array} \right\} \quad (5.5)$$

where  $\#\{\}$  denotes the number of elements that satisfy the conditions in  $\{\}$ , and the pixel coordinates of image  $I$  are  $(k, l)$  and  $(m, n)$ .

The GLCM matrices are created from these matrices by normalizing the matrices. The matrices are normalized by dividing by  $R_\theta$  for a given  $\theta$ . That is,

$$P_{i,j} = \frac{P_{i,j}}{R_\theta}. \quad (5.6)$$

The values used for  $R_\theta$  are given in Table 8, where  $n_x$  and  $n_y$  are the number of columns and the number of rows, respectively, in the image, and  $d$  is the user specified distance.

Table 8 Normalizing values

$\theta$ in degrees	$R_\theta$
$0^\circ$	$2(n_x - d)n_y$
$45^\circ, 135^\circ$	$2(n_x - d)(n_y - d)$
$90^\circ$	$2n_x(n_y - d)$

Several of the GLCM features require marginal probability mass functions (PMF). The marginal PMF's,  $p_x$  and  $p_y$ , are defined by the following formulas:

$$p_x = \sum_{j=1}^N P(i, j) / R, \quad (5.7)$$

and

$$p_y = \sum_{i=1}^N P(i, j) / R, \quad (5.8)$$

where  $N$  is the number of graylevels in the quantized image, and  $R$  is the appropriate  $R_\theta$  value.

The GLCM texture features are calculated as follows. The GLCM energy feature is a measure of the image uniformity. A region with little graylevel change will have a low-energy value,

$$f_{ENERGY} = \sum_i \sum_j [p(i, j)]^2. \quad (5.9)$$

The GLCM variance is a measure of the spread of the elements in the matrix. The feature is calculated from

$$f_{VARIANCE} = \sum_i \sum_j (i - \mu)^2 p(i, j), \quad (5.10)$$

where  $\mu$  is the mean value of the elements in  $p$ . The GLCM correlation measure quantifies the quantized graylevel linear dependence. The GLCM correlation is calculated from

$$f_{CORRELATION} = \frac{\sum_i \sum_j (ij) p(i, j) - \mu_x \mu_y}{\sigma_x \sigma_y}, \quad (5.11)$$

where  $\mu_x$ ,  $\mu_y$ ,  $\sigma_x$ , and  $\sigma_y$  are the mean values and the standard deviations of the marginal probability matrices,  $p_x$  and  $p_y$ , respectively. The entropy feature is defined as

$$f_{ENTROPY} = - \sum_i \sum_j p(i, j) \log p(i, j), \quad (5.12)$$

with the convention that  $\log(0) = 0$ . Entropy defines a measure of randomness, and a very uniform area will have very low entropy.

### 5.5.3.2 Laws Textural Features

Laws [146,147] developed a set of one-dimensional (1D) and 2D kernels which are designed to extract small-scale textural information from images. The 1D Laws kernels are given by

$$\begin{aligned} L5 &= [ 1 \ 4 \ 6 \ 4 \ 1 ] & E5 &= [ -1 \ -2 \ 0 \ 2 \ 1 ] \\ S5 &= [ -1 \ 0 \ 2 \ 0 \ -1 ] & W5 &= [ -1 \ 2 \ 0 \ -2 \ 1 ], \\ R5 &= [ 1 \ -4 \ 6 \ -4 \ 1 ] \end{aligned} \quad (5.13)$$

where the first letter stands for Level, Edge, Spot, Wave, and Ripple, respectively [146,147]. The 2D Laws textures are sized  $[5 \times 5]$ , and are created by multiplying the 1D Laws kernel as a row vector by the second kernel as a column vector. Since there are five 1D Laws kernels, there will be 25 2D kernels. As an example, the L5L5 kernel is given by

$$L5L5 = \begin{bmatrix} 1 & 4 & 6 & 4 & 1 \\ 4 & 16 & 24 & 16 & 4 \\ 6 & 24 & 36 & 24 & 6 \\ 4 & 16 & 24 & 16 & 4 \\ 1 & 4 & 6 & 4 & 1 \end{bmatrix}, \quad (5.14)$$

To create the Laws texture features, an image is convolved with each of the Laws 2D kernels. Each image is then normalized by dividing pixel-by-pixel with the  $L5L5$  image, and is termed  $I_m$  for each Laws texture kernel  $m \in \{1, 2, \dots, 25\}$ . For each Laws texture and each pixel in the convolved image, the following equation is used to calculate the texture for that pixel for the  $m$ -th texture:

$$L_m(x, y) = \sum_{j=-D}^D \sum_{k=-D}^D I_m(x + j, y + k), \quad (5.15)$$

where the texture mask size is  $(2D+1)$  by  $(2D+1)$ . As suggested by Laws [160], the variable  $D$  is selected as 7, thus equation (5.15) uses a  $[15 \times 15]$  region centered at each pixel for analysis. Note that some applications take the absolute value before summing in this formula.

Kegelmeyer *et al.* [152], Pfisterer *et al.* [145], and Gupta *et al.* [2] used Laws features for digital mammography analysis.

#### 5.5.4 Morphological Features

Morphological features are derived from the shape characteristics of the segmented region. These features include the area, axis ratio, box ratio, circularity, convex-hull area, eccentricity, equivalent diameter, extent, extent ratio, major-axis length, minor-axis length, perimeter length, solidity, and width-to-height ratio.

The area is the number of pixels in the segmented region. The axis ratio is the ratio of the major-axis length to the minor-axis length. The box ratio is the ratio of the area to the product of the height times the width, where the height and width are defined by the bounding box of the region. Circularity is defined as the product of  $4\pi$  times the region area divided by the square of the perimeter length in pixels. The convex-hull area is the size of the convex hull of the region, where the convex hull  $H$  of an arbitrary set  $S$  is the smallest convex set containing  $S$  [15,170,173]. The equivalent diameter is defined as the diameter of a circle which has the same area as the segmented region. The extent feature is calculated as the area divided by the bounding-box area. The extent ratio is defined as  $\max(\text{height}, \text{width}) / \min(\text{height}, \text{width})$ . The major- and minor-axis lengths are defined as the length in pixels of the major and minor axes of the ellipse that has the same normalized second central moments as the region, respectively. The perimeter length is the number of pixels on the region perimeter. The solidity feature is defined as the region area divided by the convex-hull area. The width-to-height ratio is defined as  $\text{width} / \text{height}$ .

### 5.5.5 Normalized Radial-Length (NRL) Features

The normalized radial-length (NRL) features are derived from a normalized version of the radial-length measure [174]. First, the border pixels of the segmentation are extracted and the centroid of the segmentation region,  $(c_x, c_y)$ , is calculated. Assume there are  $N_B$  border pixels and that the coordinate of the  $k$ -th border pixel is  $(x_k, y_k)$ . For each border pixel, the Euclidean distance between the pixel and the centroid is calculated as  $D_k = \sqrt{(x_k - c_x)^2 + (y_k - c_y)^2}$ . The largest distance,  $D_{MAX}$ , is calculated, and the normalized distance is calculated by dividing the pixel Euclidean distance by the maximum distance:  $NRL_k = D_k / D_{MAX}$ . Table 9 summarizes the NRL features, and was adapted from [174].

Table 9 NRL feature descriptions

Feature	Description
Entropy	<p>A measure of the randomness of the NRL vector values.</p> $f_{NRL\_MEAN} = -\sum_{j=1}^{N_B} p_j \log_2(p_j),$ <p>where <math>\log_2(0) = 0</math> and <math>p_j</math> is the PDF of NRL values. This PDF is estimated with 256 bins.</p>
Length	<p>The length of the NRL distance vector.</p> $f_{NRL\_LENGTH} = N_B$
Mean	<p>The mean value of the NRL distances.</p> $f_{NRL\_MEAN} = \frac{1}{N_B} \sum_{j=1}^{N_B} NRL_k$
Roughness	<p>A measure of border roughness.</p> $f_{NRL\_ROUGHNESS} = \left[ \frac{L}{N_B} \right] \sum_{j=1}^{[N_B/L]} R_j$ <p>where the roughness parameter <math>R_j</math> is given by</p> $R_j = \sum_{i=j}^{L+j}  NRL_i - NRL_{i+1}  \text{ with } j \in \{1, \dots, [N_B/L]\}.$
Standard deviation	<p>The standard deviation of the NRL vector.</p> $f_{NRL\_STD} = \frac{1}{N_B - 1} \sum_{j=1}^{N_B} [NRL_k - f_{NRL\_MEAN}]^2$ <p>Note: Some of the literature uses a biased definition for this feature, i.e. they divide by <math>N_B</math> and not by <math>N_B - 1</math>. This analysis uses the unbiased estimator.</p>
Zero crossing count	<p>The number of times the NRL distance crosses over the NRL mean.</p>

Source: Adapted from [175].

# CHAPTER VI

## DIGITAL MAMMOGRAPHIC COMPUTER AIDED DIAGNOSIS (CAD) USING ADAPTIVE LEVEL SET SEGMENTATION

### 6.1 Introduction

In previous chapters, the level set method was shown to be a flexible and robust image-segmentation method which has applications in many areas of image processing and in many diverse applications. Segmentation in the level set method is controlled by the speed function, which can be a custom-designed function for a specific image-processing task, or a function which is derived from solving the Euler-Lagrange equations associated with functional minimization.

This chapter presents a mammographic computer aided diagnosis (CAD) system, which uses an adaptive level set-based segmentation method (ALSSM). The level set method segments suspicious masses in the polar domain and adaptively adjusts the border threshold at each angle to provide high-quality segmentation results. The segmentation is performed in the polar domain, which gives the speed function fine-grained control over the segmentation. This chapter has been submitted to the IEEE Transactions in Medical Imaging Journal [176].

## 6.2 Methodology

### 6.2.1 Overview

The proposed system is shown as a block diagram in Figure 22, and follows a classic image-processing chain, as in [137,177]. The mammogram is preprocessed to remove noise and to enhance the mass. The suspicious mass is then segmented, features are extracted and optimized, and the classifier makes a benign or malignant decision. A comparison CAD system designed by Catarious [137] is also used. The proposed level set and Catarious segmentation methods are denoted ALSSM and CSM, respectively. The CSM is chosen because it has been previously tested using the DDSM database, it is relatively straightforward to implement, and it has been shown to produce relatively good results [45,132].

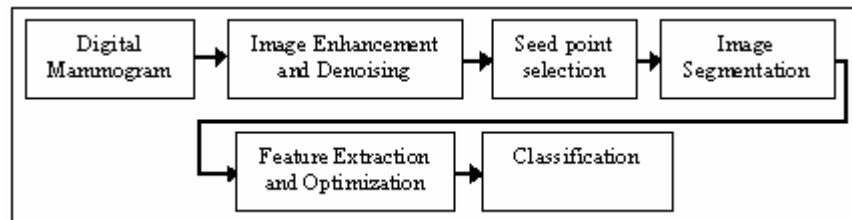


Figure 22 Proposed mammographic CAD system block diagram

### 6.2.2 Proposed CAD System

#### 6.2.2.1 Image Enhancement and Denoising

Since the mammographic images are noisy and in many cases have poor contrast, some form of image enhancement must be performed. First, CLAHE is used to remove noise and enhance the mammographic images. Next, a custom algorithm is used to provide non-linear enhancement. This algorithm is described in pseudo code in Figure 23. Lines 2-4 perform a nonlinear adjustment to the image based on the image graylevel statistics. Line 5 computes a mean

value image using  $16 \times 16$  blocks (size determined experimentally). Lines 6-9 provide further image enhancement. The function *normalize image* (NI) is used because it forces the image pixels to be in the range [0,1]. The enhancement image is created in line 9, and converted to polar coordinates in line 10.

Line 11 gauges the average rate of decay of the pixels radially away from the seed point. The seed-point selection is discussed in section 6.2.2.2. Line 12 determines a standard deviation for the isotropic Gaussian filter. The filter is modified so that pixels within one standard deviation of the seed pixel are not affected, but after one standard deviation, the decay becomes Gaussian. Previous researchers have used a fixed isotropic Gaussian filter [75]. However, better results are achieved in this study when using this modified isotropic filter. The size of the filter adapts to the characteristics of the mass under investigation. The enhanced images can be seen in Cartesian form in the third column in Figure 27. The function '*HistogramEqualize*' is the Matlab function '*histeq*'.

**Image Enhancement Pseudo Code**

**Inputs:**  $I$ -mammogram image, seed point  
**Output:**  $E$ - Cartesian enhanced image,  $P$ -Polar enhanced image

```

1    $I_{CL} \leftarrow \text{CLAHE}(I)$ 
2    $I_2 \leftarrow \text{NI}(I)$  and  $\mu \leftarrow \text{mean of all pixels in } I_2$ 
3    $I_3 \leftarrow \text{NI}(I_{CL}) \cdot \exp(-I_2/\mu)$ 
4    $I_3 \leftarrow \text{NI}(I_3)$ 
5    $M_2 \leftarrow \text{RM}(I_3, [16 \ 16])$ 
6    $I_4 \leftarrow \text{NHEQ}(I_3)$ 
7    $I_5 \leftarrow \text{NI}(I_3 + \text{RM}(M_2, [16 \ 16]))$ 
8    $I_6 \leftarrow \text{NHEQ}(I_5) \cdot I_4$ 
9    $E \leftarrow \text{NI}(I_6)$ 
10   $P \leftarrow \text{Polar}(E)$  with center at seed point
11   $\mu(r) \leftarrow \text{mean}\{P(r, \theta)\}$  for all  $r$ ;  $\mu_{\text{MAX}} \leftarrow \max(\mu)$ 
12   $\sigma \leftarrow \text{smallest radius } r \text{ with } \mu(r) \geq 0.4\mu_{\text{MAX}}$ 
13   $G(r, \theta) \leftarrow \begin{cases} 1 & r \leq \sigma \\ \exp\left(-\frac{1}{2}\left[\frac{r-\sigma}{\sigma}\right]^2\right) & r > \sigma \end{cases}$ 
14   $P(r, \theta) \leftarrow P(r, \theta)G(r, \theta)$  for all  $r, \theta$ 
15   $P \leftarrow \left(\frac{P - \text{mean}(P)}{\text{std}(P)}\right)$ 

function  $N = \text{NI}(X)$  % Normalize image
     $N \leftarrow X - \min(X)$ 
     $N \leftarrow N / \max(N)$ 

function  $N = \text{NHEQ}(X)$  % Normalize and histogram equalization
     $N \leftarrow \text{HistogramEqualize}(\text{NI}(X))$ 

% Function to compute the regional mean
function  $N = \text{RM}(X, [b1, b2])$ 
     $M \leftarrow \text{image where each pixel is mean value of a } b1 \text{ by } b2 \text{ block } B \text{ in}$ 
     $\text{image } X, N \leftarrow M \text{ resized to size of } X \text{ using 2D bilinear interpolation}$ 

```

Figure 23 Image-enhancement pseudo code

### 6.2.2.2 Seed-point Selection

A semi-automated algorithm for seed-point selection is used to determine the starting point for mass segmentation. A simple image-thresholding algorithm with graylevel regression is then run to detect areas in the image that are larger than a predefined minimum area and minimum graylevel. These constraints are introduced because masses are typically medium- to large-sized objects in the cropped image, and masses typically appear as brighter areas on the digital mammograms [27]. The algorithm is shown in Figure 24. The parameters  $N=40$  quantization bins,

$A_{MIN}$ =5000 pixels, and  $R=4$  levels are experimentally determined. The function *imregionalmax* is a Matlab image-processing toolbox function. Line 13 is optional, and allows user intervention if desired.

**Seed-point selection Algorithm Pseudo Code**

**Inputs:**  $I$ -mammogram image;  $ROI$ -ROI image;  $N$ - Quantization bins;  $R$ -Regression levels;  $A_{min}$ - Minimum segmentation area.  
**Output:**  $(x, y)$  - Seed point

- 1  $P \leftarrow$  Quantize  $I$  to  $N$  bins
- 2  $R_{MAX} \leftarrow$  All zero image same size as  $I$
- 3 **For**  $r = 1 : R$
- 4     Set  $R_{MAX} = \max(R_{MAX}, \text{imregionalmax}(q))$
- 5     Set  $q = q - R_{MAX}$
- 6 **End**
- 7 Fill holes in  $R_{MAX}$
- 8 Remove areas smaller than  $A_{min}$  in  $R_{MAX}$
- 9 Remove areas in  $R_{MAX}$  that don't overlap  $ROI$
- 10  $R_{MAX} \leftarrow \text{sign}(R_{MAX})$
- 11  $ROI \leftarrow ROI$  shrunk by 20 pixels
- 12 Select seed point as brightest pixel in region and in  $ROI$  closest to centroid of  $ROI$
- 13 Show user seed point and allow user to select from another region in  $R_{MAX}$  if desired

Figure 24 Seed-point selection algorithm pseudo code

### 6.2.2.3 Mass Segmentation

The following criteria are used to produce a good mass segmentation. First, the mass should grow outwards from a bright seed point. Second, the mass boundary should have some form of boundary regularization, and not include spurious background areas near the mass boundary. However, this regularization should not overly interfere with segmentation of small border details, which may be important for classification. Third, the segmentation should try to capture the mass and neither over-segment nor under-segment the boundary.

In the proposed approach, the narrowband level set method [4] is used since the speed function is non-Eikonal (time-varying) [14], and since this method provides a fast and flexible level set implementation. The segmentation is performed in the polar domain. Using the seed point as the center of the polar image (i.e. radius=zero), a circular region from the enhanced

mammographic image is converted to the polar domain. The polar image,  $P(r, \theta)$ , has dimensions of  $R_{MAX}$  by  $N$ . The term  $R_{MAX}$  is set to 500 pixels (approximately 21.8 mm) to accommodate the images with larger masses, and the discrete angles used to create the polar image are  $\theta \in \Theta = \left\{ \frac{2\pi n}{N} \mid n \in \{0, 1, \dots, N-1\} \right\}$ , where  $N=2880$  is the number of angles sampled in the polar image. This sampling scheme gives a 1/8 degree angular sampling rate.

The segmentation algorithm uses the enhanced-image pixel properties and varies the speed function according to an adaptive threshold,  $t(\theta)$ ,  $\theta \in \Theta$ , which is adaptively adjusted as the level set segmentation proceeds. In order to quantify the border mathematically, a scalar border complexity measure (BCM) and is defined as follows. Let  $r(\theta)$  and  $r_p(\theta)$ , be the current- and previous-iteration border radius, respectively, for  $\theta \in \Theta$ . Then define the BCM as

$$BCM = \text{mean}_{\theta} \left( \left\| \Delta r(\theta) \right\| \right), \quad (6.1)$$

where the mean value is taken over  $\theta \in \Theta$ ,  $\Delta r(\theta) = r(\theta) - r_p(\theta)$  is the change in the border radius, and  $\|\cdot\|$  is the absolute-value operator. This method is similar to the border regularization term used in [4]. In order to provide some regularity to the segmentation procedure, a smoothed version of the border-radius difference,  $\Delta r_{SM}(\theta)$ , is created by filtering  $\Delta r(\theta)$  with a simple order  $(N_S - 1)$  scaled boxcar smoothing filter with impulse response  $h[n] = \frac{1}{N_S}$ ,  $n \in \{0, 1, \dots, N_S - 1\}$ . The filter parameter  $N_S = 41$  is selected since it provides smoothing over approximately five degrees. Values much smaller than 41 caused erratic border behavior since the smoothing filter support is so small, and values much larger caused the border to be too smooth. Values from 21 to 61 produced acceptable results, so a middle value is chosen. Care is taken to ensure startup transitions of the filter and edge effects are removed.

The ALSSM uses an adaptive pixel threshold in order to segment the enhanced images created from the algorithm in Figure 25. A DC threshold and an AC threshold are summed to

create the overall pixel threshold. Initially, only a DC threshold is used, but this method tended to undersegment many of the mammograms, and also allowed small “blobs” to extend from the mass border. These small blobs are caused by background tissue or neighboring bright areas.

**Level Set Periphery Segmentation Pseudo Code**

**Inputs:**  $I$ -Enhanced mammogram image, seed point  
**Outputs:**  $S$ -Segmented image

- 1  $P \leftarrow I$  converted to polar domain
- 2 Set initial segmentation to circle of radius 10 pixels centered at seed point
- 3 Initialize SDF
- 4 Set threshold  $T_{DC}$  and  $T(\theta)$  to 0.2
- 5 **Repeat**
- 6     Set speed function using equation (6.6)
- 7     Propagate level set and reinit  $\phi$
- 8     Remove unconnected regions
- 9     Calculate new threshold
- 10 **Until** stopping criteria met
- 11  $S \leftarrow$  Convert segmentation to Cartesian domain

Figure 25 Level set segmentation pseudo code

To remedy this behavior, an AC threshold is added. The AC threshold is a function of angle and the DC threshold is a constant across all angles. Both thresholds can vary as the segmentation iterations progress. The AC threshold is adjusted using

$$T_{AC}(\theta) = \alpha_{AC} \cdot \text{sign}(\Delta r_{SM}(\theta)) \left[ 1 - \exp\left(-0.5 \cdot \frac{\Delta r_{SM}(\theta)^2}{\sigma_{AC}^2}\right) \right], \quad (6.2)$$

where  $\text{sign}(x) = 1$  if  $x > 0$ , 0 if  $x = 0$ , and -1 otherwise, and the parameters  $\sigma_{AC} = 4.0$  and  $\alpha_{AC} = 0.1$  are experimentally determined. The exponential term penalizes the areas changing rapidly more than the areas with little change. The DC threshold is adjusted using

$$T_{DC} = T_{DC\_PREV} - \left( \frac{\text{clip}(\Delta BCM, \beta)}{\alpha_{DC}} \right), \quad (6.3)$$

where  $T_{DC\_PREV}$  is the DC threshold at the previous iteration, and the parameters  $\alpha_{DC} = 0.1$  and  $\beta = 0.1$  are experimentally determined. The function  $clip(a,b)$  clips the input  $a$  at  $\pm b$ . Running the segmentation without the clipping function caused instability in some of the masses for the  $T_{DC}$  component. The overall segmentation threshold is given by

$$T(\theta) = T_{DC} + T_{AC}(\theta). \quad (6.4)$$

The level set embedded function  $\phi$  is a signed distance function (SDF), which means that  $\phi_{x,y}$  is the signed distance to the nearest segmentation boundary point from point  $(x,y)$ , with a negative (positive) sign for points inside (outside) of the boundary. The SDF is a commonly used choice for level set methods [16]. Let an auxiliary function be defined as

$$\psi_{r,\theta} = H(\phi_{r,\theta} - \gamma). \quad (6.5)$$

where  $H(x)$  is the Heaviside step function, defined as  $H(x) = 1$  if  $x \geq 0$ , and 0 otherwise, and  $\gamma = 20$ . This function is used to keep the level set from propagating outwards more than  $\gamma$  pixels from the current border during one iteration of the algorithm. The speed function is defined as

$$F_{r,\theta} = \text{sign}(P_{r,\theta} - T_{r,\theta})\psi_{r,\theta}. \quad (6.6)$$

where  $T_{r,\theta} = T(\theta)$  for all  $r \in \{0, 1, \dots, R_{MAX}\}$ . Note that the  $\psi_{r,\theta}$  term keeps the level set from segmenting radially more than  $\gamma$  pixels outwards from the current segmentation, but it does not constrain the level set if the boundary is moving radially inwards toward the seed point.

The algorithm for level set segmentation is summarized in Figure 25. Figure 26 provides a snapshot at various times of the level set segmentation, the BCM, and the threshold  $T(\theta)$ . The segmentation completes after 40 iterations, or if the segmentation boundary changes by ten pixels or less. The rightmost columns of Figure 27 show the segmentation results for several mammograms.

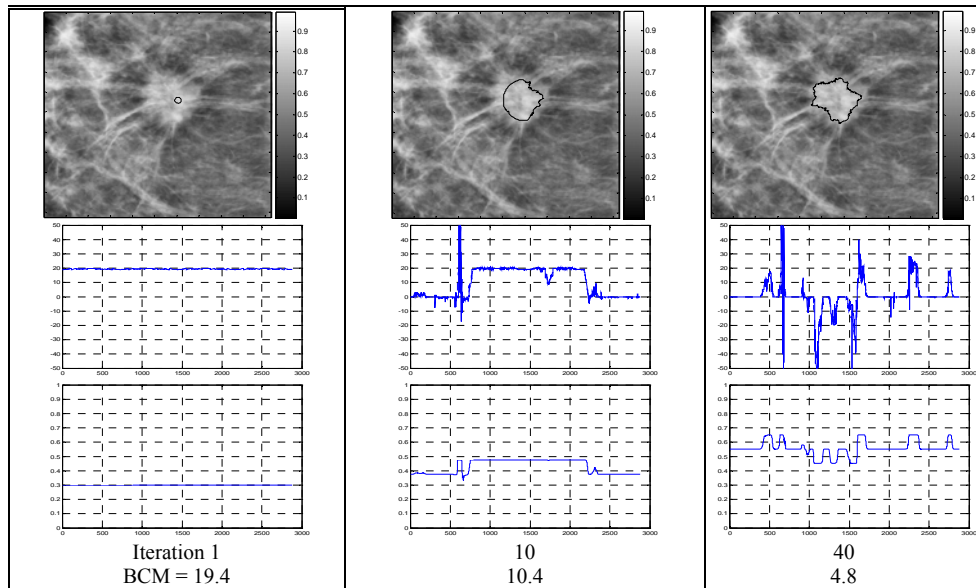


Figure 26 Example level set segmentation

The first row is the segmentation (after conversion to the Cartesian domain) superimposed over the CLAHE enhanced mammogram. A graylevel bar showing pixel levels is shown for reference purposes. The segmentation boundary is a black line. The second row shows  $\Delta r_{SM}(\theta)$ , the third row shows the threshold,  $T(\theta)$ . The fourth and fifth rows show the iteration number and the border complexity measure (BCM) for that iteration, respectively. Note in iteration 10 how the segmentation needs to advance to the left, and how the threshold had adjusted to allow this to occur.

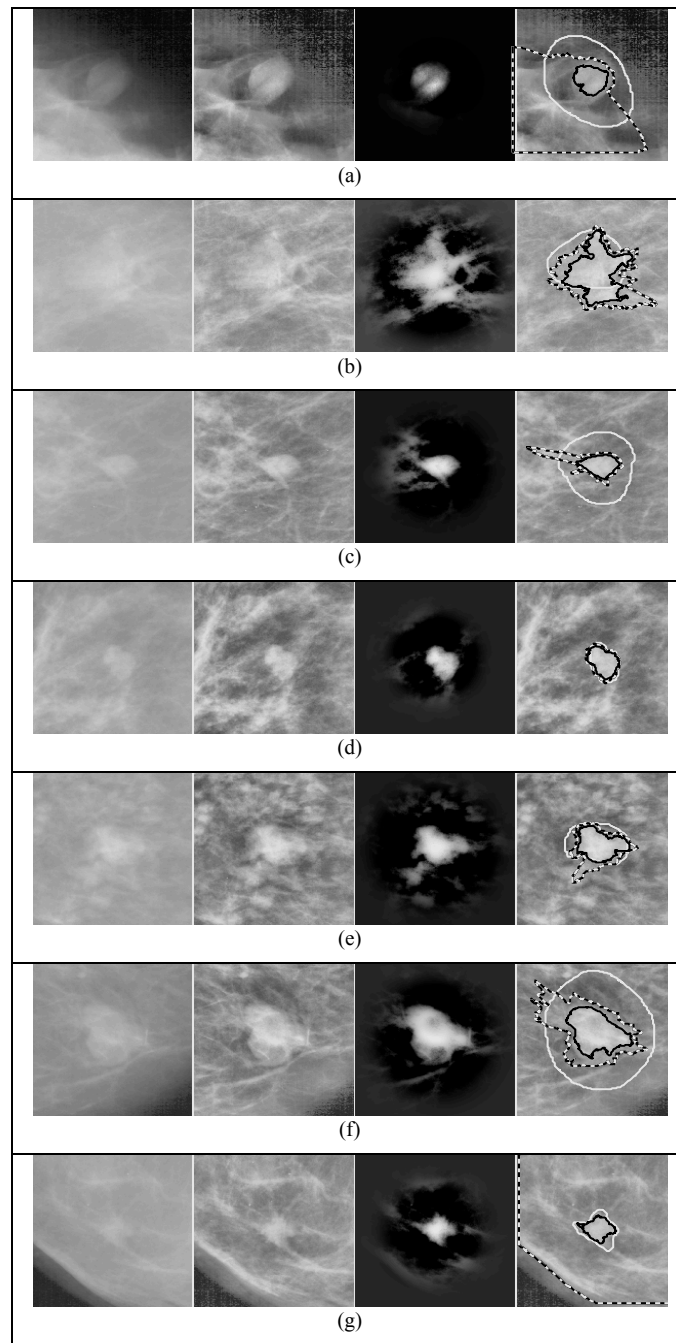


Figure 27 Enhancement images and segmentation results for selected cases

Left-to-right columns: Original mammogram image, CLAHE enhanced image, Level set segmentation enhanced image, CLAHE enhanced image with overlays of the DDSM ROI (white line), ALSSM segmentation (black line) and CSSM segmentation (black and white dashed line).

#### 6.2.2.4 Feature Extraction

Feature extraction is performed using the original mammographic image after level set segmentation is completed and the segmentation has been converted from the polar to the Cartesian domain. Two feature sets are extracted, feature set I and feature set II. These features are detailed in Table 10. Feature set I contains patient features, morphological features, features extracted from the normalized radial length (NRL), and statistical graylevel features. Feature set II contains the features in feature set I plus the textural features created from the segmentation boundary (spatial greylevel dependence (SGLD) SB features) and the rubber band straightening transform (RBST) (SGLD RBST features).

The RBST is generated with an outward and inward radius of 40 pixels. In order to create the GLCM features, the mammograms are quantized with  $N=20$  quantization levels. Details of standard features may be found in the citations listed in Table 10. Details for the SGLD SB and GLCM RBST feature are listed in reference [14].

Table 10 Feature list

Feature Set		Feature Type and source <sup>1</sup>	Features	Num. Features <sup>4,5</sup>	References
I	II				
•	•	Patient age (DDSM)	Patient Age	1	[137,177]
•	•	Morphological (SB)	Area, Axis ratio, Box ratio, Circularity, Convex hull area, Eccentricity, Equivalent diameter, Extent, Extent ratio <sup>2</sup> , Major axis length, Minor axis length, Perimeter length, Solidity, Width to height ratio	14	[105]
•	•	Statistical (SB)	Graylevel mean, Graylevel std. dev, Graylevel std. dev. ratio <sup>3</sup>	3	[105]
•	•	NRL (SB)	Entropy, Length, Mean, Roughness, Std. dev., Zero crossing count	6	[105,172,174]
	•	GLCM (SB)	(Note <sup>4</sup> ) Energy, Variance, Correlation, Inertia, Inverse Difference Moment, Entropy	144	[17,105,172,174]
	•	GLCM(RBST)	(Note <sup>5</sup> ) Energy, Variance, Correlation, Inertia, Inverse Difference Moment, Entropy	864	[17]

<sup>1</sup> This column denotes the region from which the features are extracted. DDSM=DDSM database (there is no region, as the patient age is part of the database). SB=segmentation boundary. NRL stands for Normalized Radial Length. RBST=Rubber Band Straightening Transform [17]. GLCM stands for graylevel co-occurrence matrix. GLCM is also known as spatial graylevel dependence (SGLD). <sup>2</sup> The extent ratio is  $\max(\text{length, height}) / \min(\text{length, height})$ . <sup>3</sup> the Graylevel std. dev. ratio is the ratio of the std. dev. of the graylevels inside the segmentation to the std. dev. of graylevels outside the segmentation boundary and within 200 pixels of the segmentation boundary. <sup>4</sup> The GLCM SB features are calculated at distances  $d=\{1,2,4,6,8,10\}$  and directions  $\theta=\{0^\circ,45^\circ,90^\circ,135^\circ\}$ . There will be a total of 6 GLCM features x 6 distances x 4 angles for 144 features. <sup>5</sup> The RBST features are the same features as the GLCM SB features. The RBST uses a parameter k to choose how many pixels before and after are used to create the normal vector to the boundary [174]. The RBST features are calculated for distances  $k=\{2,4,6,8,10,12\}$  For each value of k, there will be 144 features generated. Therefore there are  $864 = 144 \times 6$  features.

#### 6.2.2.5 Classification

A leave-one-out (LOO) methodology is used to perform classification [174,178,179]. In this method, one patient's data is used for testing, while all of the other patients' data form a training set which is used to train the classifier. This process repeats in a round-robin order for each patient. In this study, there are 60 mammograms, and each of the mammograms are analyzed one at a time, while the other 59 images are used for training.

A set of near-optimal features are selected from the training set and are analyzed using stepwise linear discriminant analysis (SLDA), with forward selection and backwards rejection,

using the ROC  $A_z$  metric [14,17,22,105,173] to select a combination of features that maximizes this metric [174]. The SLDA implementation details may be found in [70]. Although this method does not use an exhaustive search, the SLDA method provides a good compromise for feature selection. Once the training features are selected, SLDA provides a list of the optimal features and a weight vector, which is used to project the features into a line which best separates the classes, with zero weighting for features that are not selected. Since a LOO methodology is used, for each case there are 59 training cases. The “rule of 10,” states that for each dimension in the feature space, there needs to be at least 10 training samples [2]. Therefore, the maximum number of features SLDA is allowed to use at any time during feature analysis is six.

A  $k$ -nearest neighbor (K-NN) classifier [178,179] is used to classify the SLDA optimally weighted features from the LOO testing sample, and the system efficacy is measured with ROC analysis, overall accuracy, and the number of true positives and negatives and false positives and negatives [137,177]. The performance measures used to analyze the CAD systems are the number of true positives (TP), false positives (FP), true negatives (TN), false negatives (FN), overall accuracy (OA) and ROC  $A_z$ . The values of  $k$  are varied using  $k \in \{1,2,\dots,10\}$  in order to assess the role this parameter played.

### 6.2.3 Comparison CAD System (Catarious)

The Catarious method (CSM) is implemented as described in [137,177]. The overall implementation is the same as the proposed ALSSM method with two exceptions: (i) instead of the proposed image-enhancement method, unsharp masking is used (as defined in Catarious system in [137,177]) and (ii) CSM segmentation is used. The unsharp-masking enhancement is used, since it is used in [137,177], and it is found that the CSM method performed better with unsharp-masking enhancement, rather than the proposed enhancement scheme. Feature extraction is performed using the same features previously discussed. Classification is performed using the  $k$ -NN classifier. This allows for a direct comparison of the two segmentation schemes. The

following paragraphs provide an overview of the comparison method. For more details on Catarious' methodology, please refer to [137].

The original mammogram is passed through an unsharp-masking filter [137,177]. The algorithm uses the DDSM supplied ROI containing a suspicious region and creates a new, square ROI sized approximately  $112.6 \text{ mm}^2$  ( $245^2$  pixels) centered around the seed point. The interior pixels of the square ROI are then extracted from the unsharp masked image, where the center of the square is the seed pixel selected in section 6.2.2.2. Note that both the CSM and ALSSM use the same seed pixels.

A circular region of radius 16 mm is selected as the initial segmentation, where interior pixels are segmented, and pixels outside of the circle are considered outside of the segmentation. Fisher's LDA (FLDA) is used to select a graylevel threshold for selection of the new boundary, which is the connected region containing the ROI centroid. Boundary constraints are applied according to the Catarious algorithm, such as interior pixels on each ray emanating from the center must not have gaps of more than  $d$  pixels, and border pixels must be within a specified city-block distance  $n$  of their immediate neighbors. This analysis is performed in the polar transform. If the stopping criteria (the boundary does not change from the previous iteration) is met, then the segmentation stops; otherwise, a new iteration is performed. It is discovered that the CSM could get in a loop wherein there will not be a state during which the segmentation does not change, and no proof of convergence is given in [177]. Thus, a 40-iteration limit is added to the segmentation method. For the segmentation stage,  $n=2$ ,  $d=3$ , and the unsharp-masking weighting is 0.9, which are the original parameters proposed in [137].

The CSM system performed very well on Catarious' database: 49/50 (98%) of malignant masses are detected, and 44/50 (92%) of benign masses are classified correctly [137], which is why this method was chosen as a comparison method. It provided a "successful" segmentation method against which to compare the proposed method, and also had a straightforward implementation.

#### 6.2.4 Implementation Details for the Catarious System

The original mammographic images are downsampled by a factor of four to follow Catarious method [137]. Then, a preprocessing step using unsharp masking is applied, and the segmentation is performed on the unsharp-masked image. After the segmentation completes, the segmentation is upsampled to the original-image resolution, and pixels within three pixels of the segmentation border that are within the segmentation threshold are added to the segmentation. Feature extraction is performed on the original mammographic image using the upsampled segmentation. It is noted that there is a slight error in the description of the Fisher's linear discriminant equation on pp. 1514 of [73]: The variable  $t$  is a vector, because  $\bar{x}$  is a vector and the other terms on the right hand side are scalars. The actual threshold is zero, and the correct equation is given in [137].

Catarious set the maximum polar radius in his segmentations step to 80 pixels (16 mm) [177], because only masses with radii smaller than 16 mm are used [137]. Many of the masses in this analysis are larger, so the maximum polar radius is set to 245 pixels (49 mm), to match the maximum ROI radius in [177]. The parameters used are listed on pp. 102 of [4].

#### 6.2.5 General Implementation Details

Both the proposed and the Catarious segmentations are run on an Intel 2.0 GHz Pentium™ M processor PC, with Windows™ XP Professional, 2.0 GB RAM, in Matlab™ 7.0 release 14, SP 1, with the Matlab Image Processing Toolbox version 5.0.1. The level set code is built using Microsoft Visual C++ 2005 Express edition. The level set method is implemented using finite-difference discrete PDE evaluation, and has the following parameters. The grid spacing is  $\Delta x = \Delta y = 1$ , and the time step  $\Delta t = 1.0$ . The narrowband width is 6, and a first-order convex Hamiltonian approximation method is used for moving the front [180]. The  $k$ -NN classifier used is part of the Statistical Pattern Recognition Toolbox for Matlab™ [137]. All other code is customized code written in Matlab™.

## 6.3 Experimental Results

### 6.3.1 Qualitative Visual Comparison

Figure 27 shows representative cases, along with the segmentation results of the ALSSM and CSM, as well as the physician-supplied ROI. In Figure 27 (d) and (e), the ALSSM and CSM are almost the same. The CSM over-segments in Figure 27 (a),(c),(f), and (g). When comparing these results to those reported in [181], it can be seen that the study database of test cases is relatively challenging. This behavior explains why the system is able to catch most cancers, while having relatively more false positives. As a simple example, consider a dim mass wherein parts of the border are bright and areas around that border are also bright due to breast parenchyma and stroma. The ALSSM performs better, although it tends to slightly undersegment in some cases.

### 6.3.2 Quantitative Comparison

Note that in mammographic analysis, a FN, which is a case where the mass is malignant but the system reports it as benign, is very bad, because a patient with cancer would be told that there is no cancer. Therefore, it is critical for mammographic CAD systems to have high TP and FP ratings, and low FN ratings. The analysis results of the ALSSM and CSM methods are listed in Table 11.

Table 11 Overall results

$k^1$	Segmentation Method →	ALSSM (Proposed Method)						CSM					
$k^1$	Feature Set	OA %	TP	TN	FP	FN	Overall $A_z$ and CI	OA %	TP	TN	FP	F N	Overall $A_z$ and CI
1	I	82	25	24	6	5	0.9687 ± 0.0014	77	23	23	7	7	0.9520 ± 0.0015
2		82	25	24	6	5		77	23	23	7	7	
3		80	25	23	7	5		78	24	23	7	6	
4		85	27	24	6	3		78	24	23	7	6	
5		85	27	24	6	3		82	25	24	6	5	
6		<b>87</b>	<b>28</b>	<b>24</b>	<b>6</b>	<b>2</b>		78	25	22	8	5	
7		<b>87</b>	<b>28</b>	<b>24</b>	<b>6</b>	<b>2</b>		<b>80</b>	<b>25</b>	<b>23</b>	<b>7</b>	<b>5</b>	
8		<b>87</b>	<b>28</b>	<b>24</b>	<b>6</b>	<b>2</b>		<b>80</b>	<b>25</b>	<b>23</b>	<b>7</b>	<b>5</b>	
9		85	27	24	6	3		<b>80</b>	<b>25</b>	<b>23</b>	<b>7</b>	<b>5</b>	
10		85	27	24	6	3		<b>80</b>	<b>25</b>	<b>23</b>	<b>7</b>	<b>5</b>	
1	II	85	25	26	4	5	0.9708 ± 0.0017	80	24	24	6	6	0.9640 ± 0.0008
2		85	25	26	4	5		80	24	24	6	6	
3		82	24	25	5	6		82	25	24	6	5	
4		82	24	25	5	6		83	26	24	6	4	
5		82	24	25	5	6		82	26	23	7	4	
6		83	25	25	5	5		80	25	23	7	5	
7		85	26	25	5	4		82	26	23	7	4	
8		<b>87</b>	<b>27</b>	<b>25</b>	<b>5</b>	<b>3</b>		82	26	23	7	4	
9		<b>87</b>	<b>27</b>	<b>25</b>	<b>5</b>	<b>3</b>		<b>83</b>	<b>27</b>	<b>23</b>	<b>7</b>	<b>3</b>	
10		<b>87</b>	<b>27</b>	<b>25</b>	<b>5</b>	<b>3</b>		82	26	23	7	4	

CI = Confidence interval. OA = Overall accuracy. The best results shown in bold (best = highest overall accuracy, with lowest number of FN). The feature sets are defined in Table 10.

### 6.3.3 Comparisons to Previous CAD Systems

Table 12 shows comparisons of the proposed results (ALSSM), the CSM, and several previous studies that used the DDSM database. Overall, the ALSSM results outperformed most of the CAD systems listed in the table. However, for a truly fair comparison, each system should be tested on the same set of mammograms.

Table 12 Results for previous studies using the DDSM database

Author and Reference	Results	Author and Reference	Results
ALSSM (Proposed method)	87% OA, 2 FP	Eltonsy <i>et al.</i> [153]	85.7% TPF
CSM (In this paper)	83% OA, 3 FP	Heath and Bowyer [137,177]	~ 0.7 TPF @ 2 FPPI
CSM in Catarious <i>et al.</i> [182]	93% OA	Kinnard <i>et al.</i> [138]	$A_z = 0.66$ to 0.84
Beller <i>et al.</i> [183]	70% OA	Sample [184]	~ 80% @ 2.68 FPPI
Bilska-Wolak <i>et al.</i> [149]	At 98% sensitivity, spares ~50% of benign biopsies	Szekely <i>et al.</i> [185]	0.90 TPF
Weng and Cui [186]	0.92 TPF @ 1.33 FPPI	de Brake <i>et al.</i> [137,177]	0.90 TPF @ 1.0 FPPI

OA=Overall accuracy in percent. TPF=True Positive Fraction. FPPI=False Positives Per Image.

## 6.4 Discussion

Mass segmentation in digital mammography is a difficult task. A semi-automated procedure is performed to determine the original seed point in the mammogram based on the physician ROI. Two methods, the ALSSM and the CSM are implemented and compared. Two sets of features are extracted, and a  $k$ -NN classifier is used to classify the results as malignant or benign.

The best results are found using the ALSSM segmentation with feature set I (Patient Age, morphological, statistical, and NRL features) and  $k=6,7,8$ . The ALSSM outperformed the CSM both visually and in the overall accuracies, ROC scores, and, in almost all cases, the number of FN. Catarious' idea of using LDA for segmentation is sound, and LDA theory can generate an optimal threshold for two-class separation as claimed in [113,116]. However, the optimal LDA threshold for graylevel segmentation is not necessarily the optimal threshold for mammographic mass segmentation. Furthermore, simply unsharp masking does not sufficiently remove noise in mammographic images. The inherently noisy nature of digital mammograms, poor contrast of some suspicious areas, and the fact that most masses have a mixture of border characteristics make mass segmentation a hard problem. The CSM approach tends to oversegment in cases where the

mass has lower contrast relative to the background, and performs relatively well when the mass has high contrast. Since the CSM approach uses a single scalar threshold, it may not perform well when the mass and background blend together. On the other hand, the ALSSM proposed method uses a polar-based segmentation approach with a threshold as is a function of angle, and is adjusted dynamically as the segmentation proceeds. This method provides a more robust segmentation which is less sensitive to lower differences in the mass and background contrast.

The following chapters will build on this segmentation method by: (1) performing spiculation analysis and segmenting spiculations (when present), and (2) segmenting the mass core, that is, the low-variance portion of the mass. The periphery plus spiculation segmentations provide a two-stage analysis of mammographic images, and adding the core provides a three-stage segmentation. The core and spiculation segmentations will also be based on level set segmentation.

# CHAPTER VII

## DIGITAL MAMMOGRAM SPICULATED MASS DETECTION AND SPICULE SEGMENTATION USING LEVEL SETS

### 7.1 Introduction

This chapter presents an automated mammographic computer aided diagnosis (CAD) system to detect and segment spicules in digital mammograms, termed spiculation segmentation with level sets (SSLS). The proposed hypothesis is that overall results can be improved by segmenting the spicules of stellate lesions, rather than segmenting the lesion periphery (the main mass without spiculations) only. SSLS begins with a segmentation of the suspicious mass periphery. For this study, the periphery segmentation is created using a previously developed adaptive level set segmentation algorithm (ALSSM). The mammogram is then analyzed using features derived from the Dixon and Taylor Line Operator (DTLO), which is a method of linear structure enhancement. If a spiculated mass is detected, then the spicules are segmented using the SSLS methodology. Features are extracted, optimized, and then the suspicious mass is classified as benign or malignant. This chapter has been submitted to the IEEE Transactions in Medical Imaging Journal [187].

## 7.2 Background

### 7.2.1 Spiculation Segmentation

Giger *et al.* used region growing with an experimentally determined stopping criterion, and extracted two features based on comparison of a smoothed lesion boundary with the original lesion boundary, and on the differences between the areas of the original lesion and the lesion after morphological processing. A neural network classifier is used to analyze the features [158]. Jiang *et al.* used morphological spiculation image enhancement followed by direction map analysis and extraction of specialized graylevel features to detect spicules [160]. Kegelmeyer *et al.* examined neighborhoods of every pixel. A binary decision tree classifier is constructed based on features extracted from each pixel, which included laws texture energy features and analysis of local oriented edges. This system is intended to be a second reader CAD system used to assist radiologists in mammographic analysis [117,170].

Since the proposed method will be loosely based on the work of Sahiner *et al.* and Chan *et al.* [171], as well as Goto *et al.* [117,170], these methods will be discussed in detail. Chan *et al.* and Sahiner *et al.* [171] used a search region outside of the mass periphery and used a custom spiculation measure to create a 2D spiculation likelihood map. From this map, an experimental threshold is used to segment one pixel of the suspected spiculated area. This process is repeated 30 times (a 3mm band) in order to segment spicules. If their system classified the mass as spiculated, the spicules are added to the periphery. For each point on the boundary of the mass periphery, it utilized a circular wedge-shaped search region with radius of 4 mm, with the apex of the wedge located at a given point on the mass periphery, and the wedge size defined by  $\pm 45^\circ$  from the normal to the mass boundary,  $\vec{n}_c$ , where  $c$  indicates the  $c$ -th point on the boundary. A spiculation measure,  $x(i_c, j_c)$ , is calculated for each point  $(i_c, j_c)$  on the mass periphery. The spiculation measure is the average of the acute angle between  $\vec{n}_c$  and the angle of the image gradient at each point in the search wedge. A final post processing step removes areas disjoint from the main mass.

Goto *et al.* [117,170] used a similar spiculation search approach, and called their search area a pendulum filter. They used the pendulum filter to search a wedge shaped area, segmented the spicules that fell in the pendulum filter region of support, and then repeated this process two more times. Their segmentation method also used the image gradients, but segmented a linear subset of the spicules instead of one pixel at a time as done in [166].

### 7.2.2 Mass-periphery Segmentation

Ball and Bruce previously developed a digital mammographic CAD system for mass-periphery segmentation [4]. In this chapter, periphery segmentation denotes segmentation of the main cancerous mass, but not the spiculated portions. The system used the narrowband level set methodology [166] with an adaptive segmentation threshold controlled by a border complexity term. This method is denoted the adaptive level set segmentation method (ALSSM). This chapter uses the segmentations from this method as a basis for segmenting the spiculations in spiculated masses. The same dataset is used in this paper. Further details can be found in [2].

## 7.3 Methodology

The proposed hypothesis is that overall results can be improved if the spicules of stellate lesions are also segmented versus segmenting only the periphery, because extracting the spicule segmentations can give a more complete representation of the suspicious mass. The following sections discuss the proposed system in detail. To the best of my knowledge, this dissertation presents the first spiculation segmentation of digital mammograms using level sets.

### 7.3.1 Overview of the Proposed CAD System

Referring to Figure 28, the proposed CAD system uses the mass-periphery segmentation via ALSSM (reference chapter VI) as a starting point for spiculation detection. Features extracted from DTLO analysis of the area around the seed point are analyzed and a decision of spiculation presence or absence is made. If spicules are present, then the spicules are segmented using the

proposed level set methodology, and the new segmentation becomes the union of the previous mass periphery and the spiculation segmentations. Based on the new segmentation, features are extracted and then classified. In the proposed approach, both the  $k$ -nearest-neighbor ( $k$ -NN) [2] and maximum-likelihood (ML) [163] classifiers are used to make a benign or malignant decision. The proposed system will be evaluated for correct identification of spiculated masses, as well as overall performance compared to the ALSSM method.

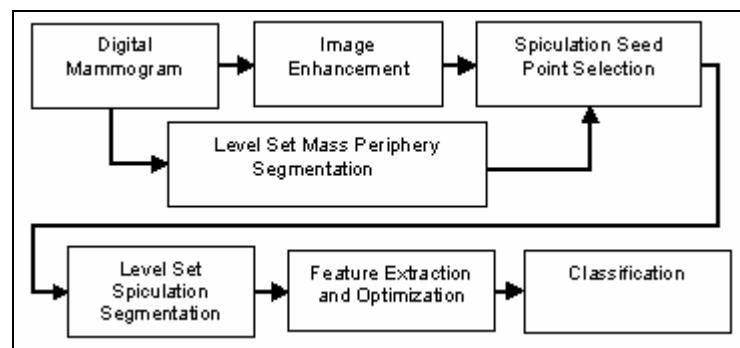


Figure 28 Proposed mammographic CAD system block diagram

In Figure 28, SSSL uses features from the DTLO image to classify the suspicious mass as spiculated or non-spiculated. Features extracted from a DTLO image analysis are analyzed by a kernel classifier. The proposed method is an extension to Zwiggelaar *et al.* [23]. The DTLO algorithm is enhanced to provide a more robust detection of spiculations, which is an extension of Dixon and Taylor [117,170]. Finally, a search area and spiculation detection method similar to Sahiner *et al.* and Chan *et al.* [171], and by Goto *et al.* [125] are used, except instead of image gradients, pixel values from an enhanced GDTLO are used.

### 7.3.2 Image Enhancement

Based on the conclusions of Pisano *et al.* on the efficacy of CLAHE (reference chapter 5.3.1) [166], the original mammographic images are first processed using CLAHE to remove

noise, and then are normalized. This enhancement image is denoted  $E_1$ . Note that this image is available from the ALSSM method [155].

### 7.3.3 Generalized Dixon and Taylor Line Operator (GDTLO)

The second preprocessing step is enhancement of linear structures. After examining several images processed using the DTLO method, it was determined that the DTLO produced good results, but the results could be improved by a slight modification of the DTLO algorithm and by employing image-enhancement techniques on the line-strength image,  $S$ .

According to Hagay, spicules may be very numerous, or spread in an irregular manner around the mass, and may have thicknesses from a tenth of a mm up to three to four mm, and lengths from several cm up to eight cm [188]. In order to better capture linear structures that are more than one pixel thick, a modified version of DTLO, called generalized DTLO (GDTLO), is proposed. The main difference in GDTLO and DTLO is that the former has a foreground kernel with a line of width  $N$ , while the latter has a foreground kernel with a line of width one. The GDTLO analysis will be denoted with the following nomenclature:  $GDTLO(K,M,N)$  denotes GDTLO where  $K$  is the number of angular orientations,  $M$  and  $N$  are the line length and width parameters, respectively. Note that  $GDTLO(K,M,1)$  is the same as  $DTLO(K,M)$ . Figure 29 shows DTLO and GDTLO foreground and background masks.

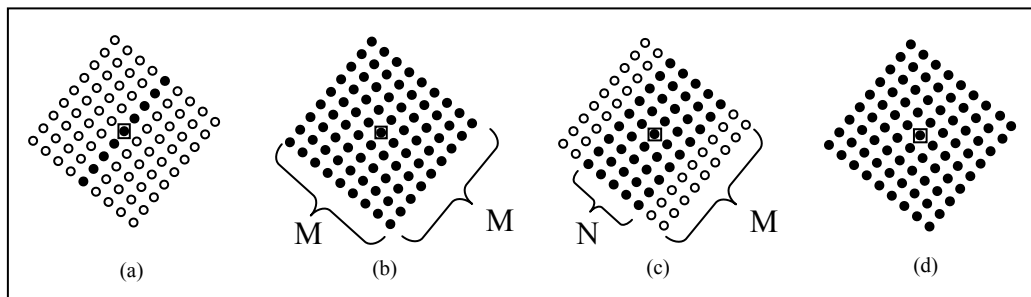


Figure 29 Dixon and Taylor Line Operator (DTLO) and generalized DTLO (GDTLO) masks

DTLO masks are shown in (a) and (b), and GDTLO masks are shown in (c) and (d). All masks shown for angular offset of  $\pi/3$  radians. (a) DTLO foreground mask. (b) DTLO background mask. The Pixel being evaluated is marked by square. Black and white circles are on and off pixels in the mask, respectively. The sum of the on pixels is one. The line length  $M=9$  is shown. (c) GDTLO foreground mask. A line width of  $N=5$  is shown, compared to a line width of one for DTLO, as shown in (a). (d) GDTLO background mask.

Three additional steps are performed once the strength map,  $S$ , is created. This process is outlined in Figure 30. First, the strength map is normalized. This image is denoted  $S_N$ . Second,  $S_N$  is processed by histogram equalization, using the Matlab function *histeq* [189]. The image resulting from both these preprocessing steps is denoted  $S_{NEQ}$ . The GDTLO parameters are set to  $M=19$ ,  $N=7$ , and  $K=12$ , which is experimentally determined. Third, a final enhancement image is created by element-by-element multiplication of  $S_{NEQ}$  with the CLAHE enhancement image. This final step further enhances bright linear areas in the image.

```

Pseudo code for spiculation enhancement image,  $E_2$ 

1. Create  $S$  from  $E_1$  using  $GDTLO(12,19,7)$ 
2.  $S_N \leftarrow \text{Normalize}(S)$ 
3.  $S_{NEQ} \leftarrow \text{Histogram Equalize}(S_N)$ 
4.  $E_2(x,y) \leftarrow S_{NEQ}(x,y)E_1(x,y)$ 

```

Figure 30 Pseudo code for generation of spiculation-enhancement image

### 7.3.4 Determination of Initial Spiculation Presence

In order to determine which mammograms are spiculated, statistical features are extracted from the  $S_{NEQ}$  image. The image graylevel histogram is analyzed using a logarithmic scale, since there can be large differences in bin values. The convention that  $\log(0)=0$  will be used, and the number of bins is 256. The feature vector is the log histogram. This feature vector is analyzed using generalized discriminant analysis (GDA) to provide a non-linear classification. GDA is the non-linear extension of linear discriminant analysis, and is described in detail in [180], and the Statistical Pattern Recognition toolbox for Matlab implementation is used [180].

In GDA, the input training dataset and class labels are  $\mathbf{R} = \{\vec{f}_k \mid k \in \{1, \dots, D\}\}$ , where there are  $D$  training instances. The data is mapped by a kernel function  $\phi: R \rightarrow F$  to a high dimensional feature space  $F$ , and LDA is applied to  $\mathbf{R} = \{\phi(\vec{f}_k) \mid k \in \{1, \dots, D\}\}$  efficiently by using dot products to perform the projections. The radial-basis function (RBF), or Gaussian, kernel is chosen. The RBF kernel for two vectors,  $\vec{a}$  and  $\vec{b}$ , and the variance parameter  $\sigma$ , is defined as

$$k(\vec{a}, \vec{b}; \sigma) = \exp\left(-\|\vec{a} - \vec{b}\|^2 / 2\sigma^2\right). \quad (7.1)$$

where  $\|\cdot\|$  is the vector-norm operator. The RBF kernel is chosen since two similar vectors will have a small response, while dissimilar vectors will have a relatively high response. The following kernel values are evaluated:  $\sigma = 10^{-2}, 10^{-1}, \dots, 10^2$ .

The GDA algorithm generates the optimal  $[D \times 1]$  projection vector,  $\vec{\alpha}$ , and the bias scalar,  $\beta$ , such that the projection  $s_m$  maximizes the class separation. The projection is given by

$$s_m = \vec{\alpha}^T \vec{K}(\vec{r}_m) + \beta. \quad (7.2)$$

where  $\vec{K}(\vec{r}_m) = [k(\vec{r}_m, \vec{r}_1; \sigma), \dots, k(\vec{r}_m, \vec{r}_D; \sigma)]^T$  is the  $[D \times 1]$  vector of kernel projections for feature vector  $\vec{r}_m$  [117,170].

The mammograms are analyzed using a leave-one-out (LOO) methodology. In a round-robin fashion, one case is sequestered for testing, while the others are used for training. The distances to the nearest malignant and nearest benign neighbor are used to classify the test case, using the reduced features from equation (7.2). If the mass is not classified as spiculated, then no spiculation segmentation is performed. Otherwise, the procedure listed in section 7.3.6 is performed to segment the spiculations.

### 7.3.5 Selection of Spicule Segmentation Seed Points

The proposed seed-point selection is closely based on the concepts proposed in [17]. For each point  $(i_c, j_c)$  on the mass periphery, the outward normal,  $\vec{n}_c$ , is calculated using the method outlined on pp. 518-519 of [17] with a parameter of  $K=20$ . Referring to Figure 31 (a), a rectangular search area,  $R_C$ , is defined such that the rectangle extended from the periphery at  $(i_c, j_c)$ , and  $R_C$  is oriented with the long axis along the direction of  $\vec{n}_c$ . Next, the pixels in  $R_C$  are extracted such that the pixel at the analysis point,  $(i_c, j_c)$ , is located at the top center pixel in  $R_C$ , and pixels radially outward from the mass boundary are filled in from top to bottom (i.e.,

larger radii are closer to the bottom of  $R_C$ ). The size of  $R_C$  is set to 150 pixels (6.53 mm) along the normal direction, by 80 pixels (3.48 mm) wide.

Next, a DTLO-based analysis is performed. The angles analyzed,  $\Theta_S$ , is a set of equally spaced angles in the range of  $\pm 45^\circ$  with a step size of  $2^\circ$ . A line with a fixed point at the top center of  $R_C$  is used for foreground analysis, and the other pixels are used for background analysis, as shown in Figure 31 (a) and (b), respectively. Since the gradients are very noisy in the DDSM mammograms, a measure based on the enhanced GTDLO image pixel values,  $S_{NEQ}$ , is adopted.

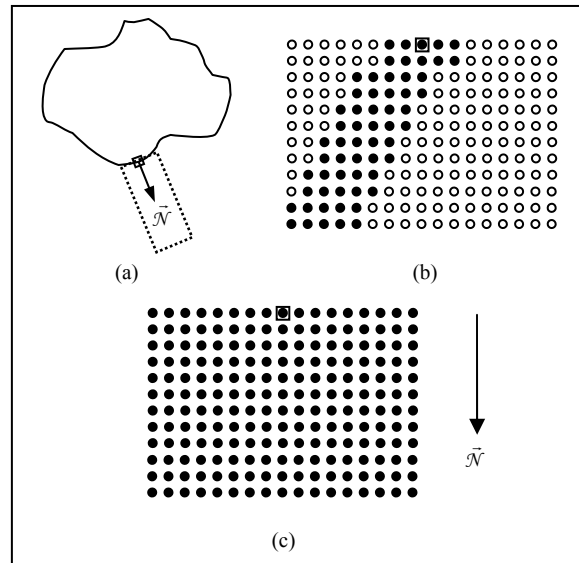


Figure 31 Representation of masks used in spiculation seed point determination

Note that the actual masks are larger. (a) Mass-periphery border (solid line) with black square indicating the border pixel being analyzed. The arrow represents the normal to the border at the point, and the dashed box is the region of support of the foreground and background masks. (b) Foreground line mask. Black pixels are on and white pixels are off, and the sum of all on pixels is one. The border pixel is shown by the black square. The top of the mask is the mass border, and pixels further down in the mask are a larger radius from the border. (c) Background mask. Black pixels are on and white pixels are off. The sum of all on pixels is one.

For each angle  $\theta_m$ ,  $S_F(\theta_m, c)$  and  $S_B(\theta_m, c)$ , the sums of the enhanced image pixels times the corresponding foreground- and background-mask pixels, respectively, are calculated,

where the notation  $(\theta_m, c)$  indicates the angle,  $\theta_m$ , and the periphery pixel index,  $c$ . The spiculation feature,  $f_c$ , is then set to

$$f_c = \max_{\theta_m \in \Theta_s} \{S_F(\theta_m, c) - S_B(\theta_m, c)\}. \quad (7.3)$$

Next, two experimentally determined thresholds,  $T_1 = 0.4$  and  $T_2 = 0.1$ , are applied as follows, in order to remove areas with low contrast or extremely low background mask values:

$$f'_c = \begin{cases} f_c & f_c > T_1 \text{ and } S_B(\theta_m^{OPT}, c) > T_2 \\ 0 & \text{otherwise} \end{cases}. \quad (7.4)$$

where  $\theta_m^{OPT}$  is the optimum angle selected.

For each set of consecutive nonzero values in  $f'_c$ , the index with the maximum  $f'_c$  value is chosen as a seed point. Since the search areas of nearby pixels could potentially point to the same spicule, redundant seed points could be detected. Therefore, any seed point which had a neighboring seed point within ten border pixels with a lower value of  $f'_c$  is removed from the seed point list. Finally, any seed points which have an optimal direction such that a straight line in that direction would leave and then re-enter the periphery are discarded, which could happen for areas that are very convoluted.

Let  $ns$  be the final number of seed points detected. The results of the spiculation seed point detection are: (1) a set of spiculation seed points,  $SP = \{\vec{P}_1, \dots, \vec{P}_{ns}\}$ , (2) a set of optimal angles for each seed point,  $\Theta_{OPT} = \{\theta_1^{OPT}, \dots, \theta_{ns}^{OPT}\}$ , and (3) a set of optimal unity-magnitude vectors pointing in the optimal spiculation direction,  $D_{OPT} = \{\vec{D}_1^{OPT}, \dots, \vec{D}_{ns}^{OPT}\}$ , where  $ns$  is the number of seed points. Figure 32 (a) shows a the spiculation feature after thresholding,  $f'_c$ . The seed points are shown as circles on the graph of  $f'_c$ . Figure 32 (b) shows the enhancement image, with crosshairs showing the seed points, and the corresponding optimal vectors shown as arrows.

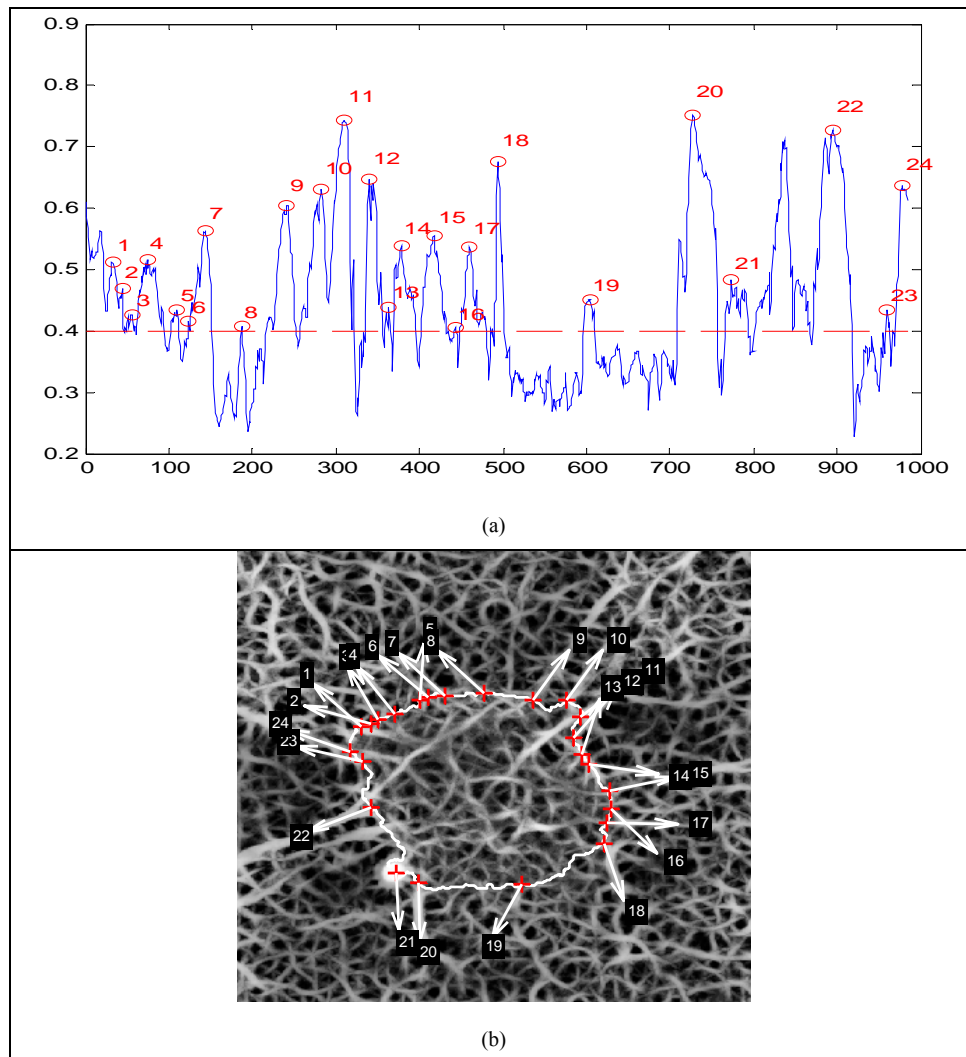


Figure 32 Graph of spiculation feature showing seed points and spiculation enhancement image

(a) The spiculation feature,  $f_s$ , which is the difference of the foreground mask and background mask responses. The spiculation seed points are numbered. The threshold  $T_l$  is shown as a dashed horizontal line. (b) The spiculation enhancement image, showing optimal angles. The numbers correspond to the graph in (a). This case is also shown on the bottom row of Figure 8.

### 7.3.6 Level Set Spicule Segmentation

From sections 7.3.4 and 7.3.5 above, a set of spiculation seed points and optimal angles are generated, which are locations on the periphery where the line-detector response across the optimal angles is maximized. A simple but effective method is to examine the magnitude of the

GDTLO spiculation enhancement image,  $E_{SPIC}$ , in combination with the direction difference between the optimal spiculation vector,  $\vec{D}_c^{OPT}$ , and the GDTLO angle,  $\vec{D}_{DT}$ , for each point in a rectangle oriented with the long part in the direction of  $\vec{D}_c^{OPT}$ , as follows:

$$F_c(x, y) = E_{SPIC}(x, y) \left| \left\langle \vec{D}_c^{OPT}, \vec{D}_{DT}(x, y) \right\rangle \right|. \quad (7.5)$$

where  $||$  denotes absolute value and  $\langle \cdot, \cdot \rangle$  denotes the inner (dot) product. The absolute values are required since the Dixon Taylor optimal angle is limited to the range  $[0, \pi)$  and the optimal angle has range  $[0, 2\pi)$ . Please refer to Figure 33 (a) and (b).

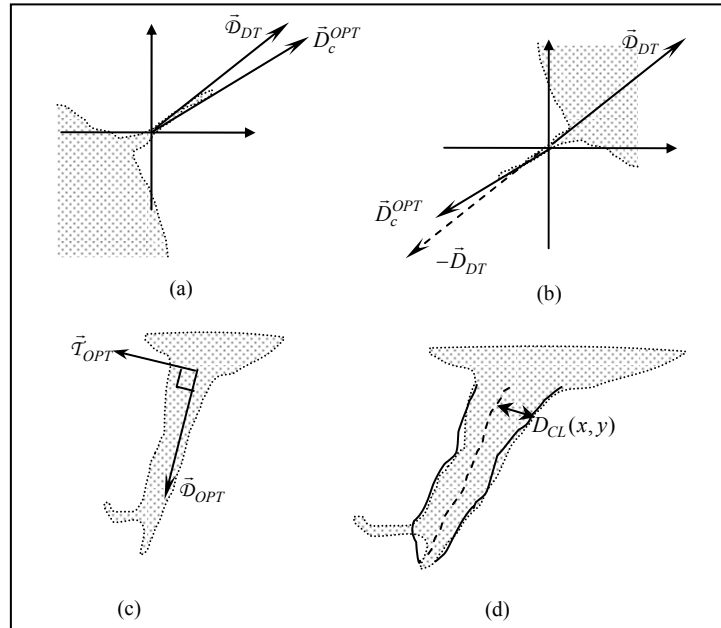


Figure 33 Diagrams for GDTLO analysis

(a),(b): Diagram of the optimal spiculation vector, the Dixon and Taylor (DT) angle vector. A segment of a mass is shown as the dotted region, with a spiculation protruding. (a) Case where the optimal angle is in  $[0,\pi)$ . (b) Case where the optimal angle is in  $[\pi,2\pi)$ . (c),(d): Smoothing prior to level set segmentation. (c) The optimal direction,  $\vec{D}_c^{OPT}$ , and tangent direction,  $\vec{T}_c^{OPT}$ . (d) Boundary after smoothing filter has been applied (dark lines) and smoothed center line (dashed line). Also shown is the distance from a point  $(x,y)$  on the smoothed boundary line to the center line.

A threshold is applied to the result from equation (7.4). In order to remove small spurs from the image, for each pixel in  $F_c(x,y)$  which is  $\geq T_3$ , the orthogonal projection to the optimal angle vector,  $\vec{D}_c^{OPT}$ , is calculated. The threshold value is experimentally determined as  $T_3 = 0.4$ . Values greater than twelve pixels away are clipped at twelve pixels. Then, for each set of pixels in the direction of the optimal tangent  $\vec{T}_c^{OPT}$ , the values are filtered with a lowpass filter with impulse response  $h[n] = \frac{1}{15}$  for  $n \in \{0, \dots, 14\}$ . The filter length is experimentally determined.

Reference Figure 33 (c). The lowpass filtering smooths the edges. For each pixel along the

optimal angle vector  $\vec{D}_c^{OPT}$ , the mean pixel distance in the direction of  $\vec{T}_c^{OPT}$  and  $-\vec{T}_c^{OPT}$  is calculated, and is shown as the dashed line in Figure 33 (d). Let  $D_{CL}(x,y)$  be the smallest distance from the point  $(x,y)$  to the mean pixel distance center line. The final speed functions is

$$F'_c(x,y) = F_c(x,y) \exp\left(-\frac{1}{8}D_{CL}(x,y)\right) - T_3. \quad (7.6)$$

where the constant in the exponential term is chosen to allow the spiculation to grow to a certain size tangentially. Once all of the spicules have been segmented, the spiculation segmentation becomes the union of the original mass periphery and each spiculation segmentation.

The narrowband level set method requires an initial segmentation to form the narrowband. A small square centered at the spiculation seed point is used as the initial segmentation. The results of the level set segmentation for several example cases are shown in Figure 34, as well as the spiculation enhancement image, and the ALSSM periphery segmentation.

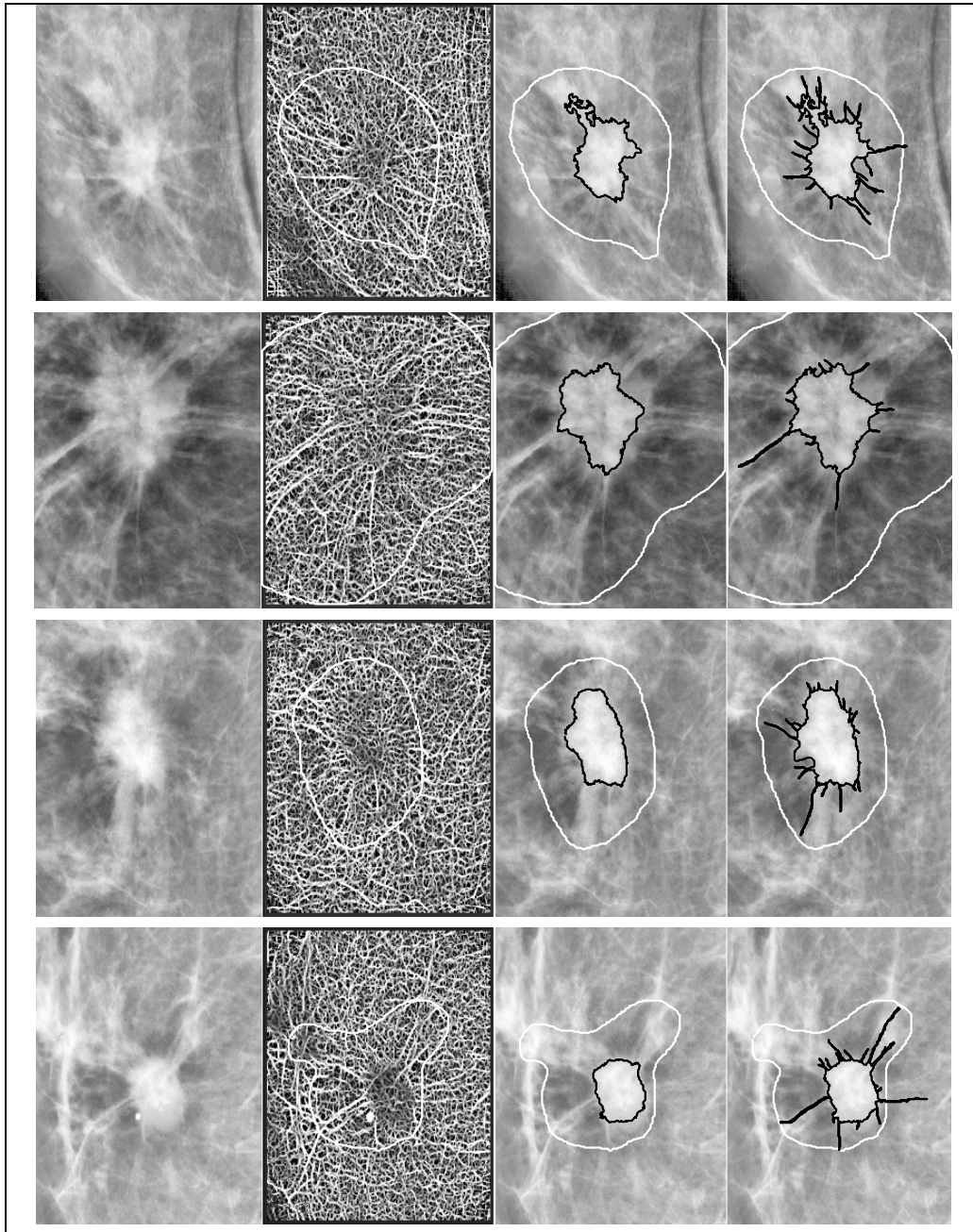


Figure 34 Selected spiculated mammograms showing images in spiculation processing

Left to right columns: CLAHE enhanced image, GTDLO image, ALSSM periphery segmentation, and the proposed spiculation segmentation, respectively. In the two rightmost images, the physician-supplied ROI is shown in white. If the ROI is larger than the portion of the image shown, then it is clipped. The segmentations are shown in black.

### 7.3.7 Feature Extraction, Optimization, and Classification

The features extracted include patient age, morphological features, statistical graylevel features, and features based on the segmentation boundary and the rubber band straightening transform (RBST) [166]. The features are described in Table 13, and detailed descriptions may be found in the references in the table. All features are extracted from the original mammogram image after cropping. Feature sets A and B are feature sets I and II in [166]. There are a large number of features, and the feature set must be reduced due to the limited training samples available. Stepwise linear discriminant analysis (SLDA) using receiver operating characteristics (ROC) area under the curve ( $A_z$ ) with forward selection and backward rejection is used to optimally select up to ten features and project them to maximize class separation. The SLDA implementation is described in [16]. The maximum number of features is limited to ten, in order to avoid overtraining. After feature optimization, the  $k$ -NN and ML classifiers are used to classify the tumor as malignant or benign.

Table 13 Feature list

Feature Set			Feature Type and Source <sup>1</sup>	Feature List	Number of Features	References
A	B	C				
•	•	•	Patient age (DDSM)	Age	1	[137,177]
•	•		Morphological (SB)	Area, Axis ratio, Box ratio, Circularity, Convex hull area, Eccentricity, Equivalent diameter, Extent, Extent ratio <sup>2</sup> , Major axis length, Minor axis length, Perimeter length, Solidity, Width to height ratio	14	[105]
•	•		Statistical (SB)	Graylevel mean, Graylevel std. dev, Graylevel std. dev. ratio <sup>3</sup>	3	[105]
•	•		NRL (SB)	Entropy, Length, Mean, Roughness, Std. dev., Zero crossing count	6	[105,172,174]
	•	•	GLCM (SB)	(Note <sup>4</sup> ) Energy, Variance, Correlation, Inertia, Inverse Difference Moment, Entropy	144	[17,105,172,174]
	•	•	GLCM (RBST)	(Note <sup>5</sup> ) Energy, Variance, Correlation, Inertia, Inverse Difference Moment, Entropy	864	[17]

Feature sets A and B are the same as feature sets I and II from the previous chapter. <sup>1</sup> This denotes the region from which the features are extracted. DDSM=DDSM database (there is no region, as the patient age is part of the database). SB=segmentation boundary. NRL stands for Normalized Radial Length. RBST=Rubber Band Straightening Transform [17]. GLCM stands for graylevel co-occurrence matrix. GLCM is also known as spatial graylevel dependence (SGLD). <sup>2</sup> The extent ratio is  $\max(\text{length, height}) / \min(\text{length, height})$ . <sup>3</sup> the Graylevel std. dev. ratio is the ratio of the std. dev. of the graylevels inside the segmentation to the std. dev. of graylevels outside the segmentation boundary and within 200 pixels of the segmentation boundary. <sup>4</sup> The GLCM SB features are calculated at distances  $d=\{1,2,4,6,8,10\}$  and directions  $\theta=\{0^\circ,45^\circ,90^\circ,135^\circ\}$ . There will be a total of 6 GLCM features x 6 distances x 4 angles for 144 features. <sup>5</sup> The RBST features are the same features as the GLCM SB features. The RBST uses a parameter  $k$  to choose how many pixels before and after are used to create the normal vector to the spiculation boundary [104]. The RBST features are calculated for distances  $k=\{2,4,6,8,10,12\}$  For each value of  $k$ , there will be 144 features generated. Therefore there are  $864 = 144 \times 6$  features.

### 7.3.8 Analysis of Results

Two analyses are run. In analysis I, the classifier results are not modified based on the spiculation detection. According to Tabár and Dean, histological examination is required to definitively diagnose a stellate lesion, and "...the only stellate lesion which may be followed conservatively is postoperative traumatic fat necrosis" [190]. This opinion is shared by Vyborny *et al.* [155] and Hagay [174,178,179]. Therefore, in analysis II, all cases that are detected as spiculated are classified as malignant, regardless of the classifier results, while the non-spiculated cases will be classified according to the classifier result. This method is similar to what could

happen in a situation when a radiologist uses a CAD system as a second opinion. The radiologist can overrule the CAD classification as benign when they believe that a mass is spiculated.

The results are evaluated using the area under the ROC curve ( $A_z$ ) [178], the  $A_z$  confidence intervals (95% confidence level), as well as overall accuracy (OA), number of true positives (TP), false positives (FP), true negatives (TN), and false negatives (FN) [191]. A statistical analysis is performed to compare the classification results. A two-tailed paired samples  $t$ -test at the 95% confidence level is used. The resulting  $p$  value is then compared to 0.05, where  $p < 0.05$  is statistically significant. The percentage of variance accounted for by adding the additional segmentation features,  $r^2$ , is also calculated. Values of  $r^2$  such that  $0.09 < r^2 < 0.25$  and  $r^2 > 0.25$  are considered medium and large effects, respectively [74]. Reference pp. 333-343 and pp. 285-289 of [163] for discussion of the  $t$ -test and the  $r^2$  statistics, respectively.

## 7.4 Results and Discussion

### 7.4.1 Example Cases

Figure 34 shows several example cases. In this figure, the CLAHE enhanced image and the GDTLO enhanced image are shown. The two rightmost images show the physician ROI (white line), and the periphery and spiculation segmentations, both shown in black lines. Overall, the spiculation method tended to perform very well.

### 7.4.2 Results of GDA Spiculation-Feature Analysis

The GDA feature analysis is performed, and all of the spiculated masses are detected. All spiculated masses are correctly identified, with no false positives, for an overall accuracy of 100%. These results are very encouraging and validate the intuition and stated desire of Zwiggelaar *et al.* to use a more sophisticated classifier [163]. The overall  $A_z=1.0$ , indicating that the training data are perfectly separable. The best results are obtained with  $\sigma = 10^{-2}$ .

### 7.4.3 Comparison of SLS to ALSSM

In Table 14, the “best” results are shown in bold, where “best” means the highest overall accuracy with lowest number of FN. The feature sets are defined in Table 13. FS=Feature Set, CL=Classifier, OA=Overall accuracy, TP=True Positives, TN=True Negatives, FP=False Positives, and FN=False Negatives,  $A_z=A_z$  value and 95% confidence interval. Overall accuracies are rounded up to the nearest integer percentage value.

From Table 14, it can be seen that in general, the SLS (based on periphery plus spiculation segmentation) outperforms the corresponding ALSSM (periphery-only segmentation) in terms of higher overall accuracy, lower number of FN, and higher  $A_z$  values. For feature set A, which contains patient age, morphological, statistical, and NRL features, the results increased the highest  $k$ -NN accuracy from 87% to 88% and 90% for analysis I and II, respectively. Analysis II provided the best results, with 2 FN for  $k=5$ . The ML classifier had a striking difference in accuracies, going from 80% with ALSSM to 88% and 90% respectively, with analysis I and II. In general, the ML classifier had more FN and fewer FP than the  $k$ -NN classifier, which is an undesirable result. Feature set B, which includes the features in feature set A as well as the SGLD texture features, showed improvements in analysis I and II. The best results are for  $k=5$ , which improved the overall accuracies from 82% for ALSSM to 88% and 90%, and reduced the FN from 6 for ALSSM to 3 and 2, respectively, for analysis I and II. Analysis II ML improved by reducing the FP from 4 to 2. ML achieved 90% and 88% overall accuracies, for analysis I and II, versus 87% for ALSSM. For feature set C, which is the patient age and the SGLD features, the results are the best. One striking difference is the large increase in overall accuracy for  $k=1$  and 2: ALSSM has 77% overall accuracy, and analysis I and II results are both 93% overall accuracy. The number of FN is reduced from 5 to 1 for both analysis I and II. The ML classifier had similar results.

Table 14 Overall results

Feature Set	SSLS (spiculation) analysis I						SSLS (spiculation) analysis II						ALSSM (periphery only)						
	CL	OA	TP	TN	FP	FN	A <sub>Z</sub>	OA	TP	TN	FP	FN	A <sub>Z</sub>	OA	TP	TN	FP	FN	A <sub>Z</sub>
A	1-NN	82	25	24	6	5	0.9862 ± 0.0006	87	28	24	6	2	0.9862 ± 0.0006	82	25	24	6	5	0.9687 ± 0.0014
	2-NN	82	25	24	6	5		87	28	24	6	2		82	25	24	6	5	
	3-NN	83	25	25	5	5		88	28	25	5	2		80	25	23	7	5	
	4-NN	82	24	25	5	6		87	27	25	5	3		85	27	24	6	3	
	5-NN	<b>88</b>	<b>27</b>	<b>26</b>	<b>4</b>	<b>3</b>		<b>90</b>	<b>28</b>	<b>26</b>	<b>4</b>	<b>2</b>		85	27	24	6	3	
	6-NN	87	27	25	5	3		88	28	25	5	2		<b>87</b>	<b>28</b>	<b>24</b>	<b>6</b>	<b>2</b>	
	7-NN	87	27	25	5	3		88	28	25	5	2		<b>87</b>	<b>28</b>	<b>24</b>	<b>6</b>	<b>2</b>	
	8-NN	87	27	25	5	3		88	28	25	5	2		<b>87</b>	<b>28</b>	<b>24</b>	<b>6</b>	<b>2</b>	
	9-NN	87	27	25	5	3		88	28	25	5	2		85	27	24	6	3	
	10-NN	87	27	25	5	3		88	28	25	5	2		85	27	24	6	3	
	ML	88	25	28	2	5		90	26	28	2	4		80	21	27	3	9	
B	1-NN	82	25	24	6	5	0.9862 ± 0.0007	87	28	24	6	2	0.9862 ± 0.0007	85	25	26	4	5	0.9708 ± 0.0017
	2-NN	82	25	24	6	5		87	28	24	6	2		85	25	26	4	5	
	3-NN	83	25	25	5	5		88	28	25	5	2		82	24	25	5	6	
	4-NN	82	24	25	5	6		87	27	25	5	3		82	24	25	5	6	
	5-NN	<b>88</b>	<b>27</b>	<b>26</b>	<b>4</b>	<b>3</b>		<b>90</b>	<b>28</b>	<b>26</b>	<b>4</b>	<b>2</b>		82	24	25	5	6	
	6-NN	87	27	25	5	3		88	28	25	5	2		83	25	25	5	5	
	7-NN	87	27	25	5	3		88	28	25	5	2		85	26	25	5	4	
	8-NN	87	27	25	5	3		88	28	25	5	2		<b>87</b>	<b>27</b>	<b>25</b>	<b>5</b>	<b>3</b>	
	9-NN	87	27	25	5	3		88	28	25	5	2		<b>87</b>	<b>27</b>	<b>25</b>	<b>5</b>	<b>3</b>	
	10-NN	87	27	25	5	3		88	28	25	5	2		<b>87</b>	<b>27</b>	<b>25</b>	<b>5</b>	<b>3</b>	
	ML	88	25	28	2	5		90	26	28	2	4		87	26	26	4	4	
C	1-NN	<b>93</b>	<b>29</b>	<b>27</b>	<b>3</b>	<b>1</b>	0.9849 ± 0.0006	<b>93</b>	<b>29</b>	<b>27</b>	<b>3</b>	<b>1</b>	0.9849 ± 0.0006	77	25	21	9	5	0.9679 ± 0.0018
	2-NN	<b>93</b>	<b>29</b>	<b>27</b>	<b>3</b>	<b>1</b>		<b>93</b>	<b>29</b>	<b>27</b>	<b>3</b>	<b>1</b>		77	25	21	9	5	
	3-NN	92	29	26	4	1		92	29	26	4	1		80	25	23	7	5	
	4-NN	92	29	26	4	1		92	29	26	4	1		82	26	23	7	4	
	5-NN	92	29	26	4	1		92	29	26	4	1		83	26	24	6	4	
	6-NN	92	29	26	4	1		92	29	26	4	1		83	26	24	6	4	
	7-NN	90	28	26	4	2		90	28	26	4	2		85	26	25	5	4	
	8-NN	92	29	26	4	1		92	29	26	4	1		85	26	25	5	4	
	9-NN	90	28	26	4	2		90	28	26	4	2		85	26	25	5	4	
	10-NN	92	29	26	4	1		92	29	26	4	1		<b>87</b>	<b>26</b>	<b>26</b>	<b>4</b>	<b>4</b>	
	ML	90	27	27	3	3		92	28	27	3	2		<b>87</b>	<b>26</b>	<b>26</b>	<b>4</b>	<b>4</b>	

Comparing all of these results, some of the features selected by SLDA in feature sets A and B had some class confusion. This also points out that adding more features may not necessarily improve results, which may be a result of the limited training-set size (59 images in each LOO iteration). Furthermore, SLDA is used, which did not provide an exhaustive search for best-feature selection. The best results occurred using the  $k$ -NN classifier, analysis II, feature set C, and  $k=1$  or 2, although all of the  $k$ -NN results for feature set C are very similar.

The  $A_z$  values for SSLS analysis improved for feature sets A, B, and C, indicating that the spiculation features are more powerful discriminators than the periphery features alone. From Table 15, it can be seen that the results using feature sets A and B are statistically different for the spiculation segmentation versus the periphery. Also from Table 15, the  $r^2$  values indicate that a significant portion of the change is related to the change from the periphery to spiculation features. Note that some of the  $z$ -statistic values are very close to the critical value, but are still significant. From the previous discussion, it is clear that the SSLS method improved the performance of the CAD system.

Table 15 Statistical analysis results comparing the periphery (SSLS) segmentation to the periphery only segmentation (ALSSM)

Feature Set	p value	$r^2$ value
A	<b>&lt;0.001</b>	0.74
B	<b>0.008</b>	0.92
C	0.285	0.94

Statistically significant results ( $p < 0.05$ ) are shown in bold.

During LOO analysis, SLDA processes each feature and determines an  $A_z$  value for each feature. Since there are sixty mammograms in the study database, each feature will have sixty LOO  $A_z$  values, which are referred to as SLDA LOO  $A_z$  values. Figure 35 and Figure 36 show the mean and  $\pm$  one standard deviation of the SLDA LOO  $A_z$  values for each feature, for both the periphery and spiculation feature sets. The most drastic changes are expected in the NRL features, and this is clearly shown in Figure 35 for many of the morphological and NRL features, since

these features are directly related to the shape of the segmentation. Figure 36 shows the changes for the statistical and GLCM features, most of which are relatively small.

## 7.5 Conclusions

The proposed SSLS method is based on the spiculation image enhancement of Zwiggelaar *et al.* [23], by the DTLO line enhancement algorithm of Dixon and Taylor [117,170], and by the spiculation segmentation methods of Sahiner *et al.* and Chan *et al.* [171] and Goto *et al.* [11,94], and provides an important extension of their work. The level set methodology provided a fast and efficient means of segmenting the spiculated regions. Fortunately, since spicules are fairly linear and grow outwards from the periphery, a simple speed function could be generated to segment the spicules.

The GDA method proved to be very effective in analyzing the images for spiculation presence. For the DDSM images in this study, each spiculated image is detected properly, and no non-spiculated images are falsely classified as spiculated. The GDTLO enhancement algorithm proved to be very effective at highlighting linear structures. This can clearly be seen in Figure 32 (b) and Figure 34. The proposed method performed very well, and in almost all cases, performed better than segmentation of the periphery alone. The best results are obtained from feature set C (patient age and the SGLD features), analysis I or II, for  $k=1$  and 2 with the  $k$ -NN classifier, where the OA are 93%, 3 FP and 1 FN. In general, the  $k$ -NN classifier outperformed the ML classifier slightly in terms of higher OA and fewer FN.

From Table 14, Analysis II reduced the number of FN by one for feature set A (patient age, morphological, statistical, and NRL features) and B (patient age, morphological, statistical, NRL, and GLCM features), and had the same number of FN for feature set C (patient age, GLCM features). From Table 15, the LOO  $A_Z$  values for the SSLS (periphery + spiculations) compared to the ALSSM (periphery only) are statistically different for feature sets A (patient age, morphological, statistical, and NRL features) and B (patient age, morphological, statistical, NRL, and GLCM features) at 95% confidence level. Feature set C (patient age, GLCM features) is not

statistically significant. This is expected, due to the large changes in the morphological and NRL features, as shown in Figure 35, and the small changes in GLCM features, as shown in Figure 36

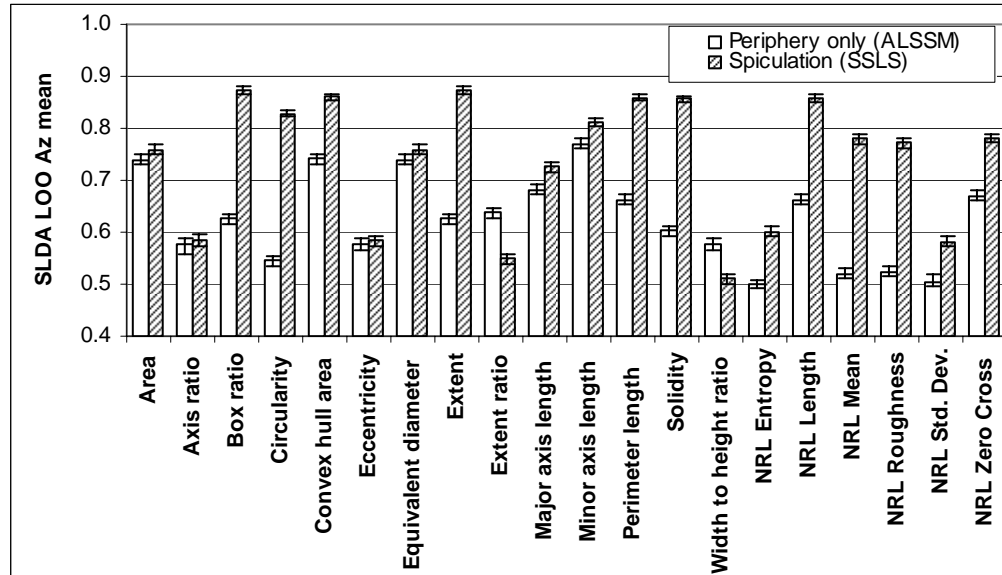


Figure 35 SLDA LOO  $A_z$  analysis results for morphological and NRL features

Error bars show  $\pm$  one standard deviation.

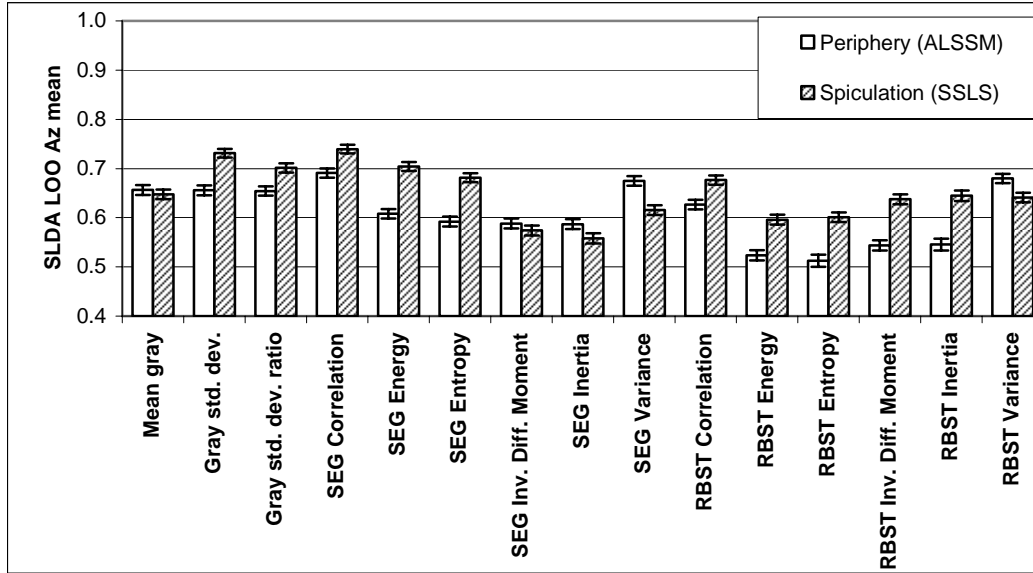


Figure 36 SLDA LOO  $A_z$  analysis results for statistical, GLCM segmentation (SEG) and GLCM RBST (RBST) features.

Error bars show  $\pm$  one standard deviation.

# CHAPTER VIII

## LEVEL SET-BASED CORE SEGMENTATION OF MAMMOGRAPHIC MASSES FACILITATING THREE-STAGE (CORE, PERIPHERY, SPICULATION) ANALYSIS

### 8.1 Introduction

This chapter discusses a mammographic mass core segmentation method based on the Chan-Vese level set method, which is a minimal variance segmentation method. The core segmentation method is analyzed via resulting feature efficacies. Additionally, the core segmentation method is used to investigate the idea of a three stage segmentation approach, i.e. segment the mass core, periphery, and spiculations (if any exist) and use features from these three segmentations to classify the mass as either benign or malignant. The definitions of the three segmented regions are as follows. The mass core is defined as the brightest central parts of the tumor, which also have low variance. The mass periphery is defined as the main tumor area, which typically appears as light gray to white on the mammogram. The mass spiculations, if they are present, are small, linear projections extending from the tumor peripheries. Figure 37 illustrates these types of segmentation for a benign mass, a non-spiculated malignant mass, and a spiculated malignant mass. Note that most benign masses and some malignant masses are not spiculated and, thus, will not require a spiculation segmentation; however, all masses will have a periphery and a core segmentation.

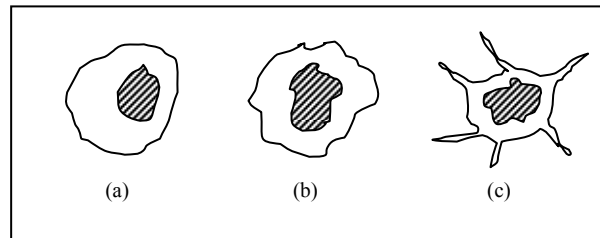


Figure 37 Three stage segmentation model

Notes: (a) Benign mass showing core (striped) and periphery (solid) segmentations. (b) Malignant non-spiculated mass core and periphery segmentations. (c) Malignant spiculated mass core, periphery, and spiculation segmentations.

To the best of my knowledge, published mammography CAD systems do not use a three stage approach as proposed in this letter, i.e. a core, periphery, and spicules (Some CAD systems may segment the periphery and spicules, and also look for microcalcifications). Most segment the periphery only, some segment spicules only, and a very small number segment the periphery and spicules. The motivation for the core segmentation is that features derived from the core and from the region between the core and periphery segmentation borders may provide important information which could improve classification results, especially when these features are combined with the periphery or spiculation features. This chapter has been submitted to the IEEE Transactions in Medical Imaging Journal [192].

## 8.2 Methodology

The proposed hypothesis is that overall results may be improved if multiple segmentations of the mass are analyzed. The periphery segmentation in [166] is designed to accurately segment the main mass. The spiculation segmentation is designed to detect and segment the spicules for spiculated masses. This chapter discusses the core segmentation, and what effects it has on the classification results and feature efficacy. The following sections discuss the proposed system and analysis methods in detail.

### 8.2.1 Overview of the Proposed CAD System

In previous work, the author has developed a level set-based digital mammogram periphery-segmentation (using ALSSM method) [80] and spiculation detection and segmentation (using the SSLS method). Combining these two level-set based systems gives a two-stage system, potentially providing two segmentations and two separate feature sets. This work is extended in this paper to include a third stage, which is the mass core, which is defined as the largest bright connected area inside the main mass. Furthermore, the core is restricted such that it must stay a small distance from the main mass periphery, in order to facilitate feature extraction in the region between the core and the main mass. Some tumors, such as an infiltrating ductal cancer, forms a hard, firm lump due to scar tissue formation, called fibrosis. This scar tissue is the result of a desmoplastic response to the cancer [16]. The features extracted between the periphery and the core may be important in the classification stage of the CAD system.

The proposed system block diagram is shown in Figure 38. The mammogram is first analyzed via the ALSSM periphery-analysis system. The periphery is segmented, and the results are passed to a feature-extraction stage. Next, if spicules are detected by the SSLS system, then the spicules are segmented. These results are then passed to a feature-extraction stage. If no spicules are detected, then the spicule segmentation defaults to the periphery segmentation. The features extracted from the periphery and spiculation segmentations include combinations of standard mammographic features such as morphological features, graylevel statistical features, normalized-radial length (NRL) features, and graylevel co-occurrence matrix features (GLCM). These features are listed in Table 17, which includes references.

The periphery-segmentation result is also passed to the core-segmentation algorithm. Once the core has been segmented, then those results are passed to a feature-extraction stage. This feature set contains the standard features used in the periphery and spiculation segmentations, respectively. The core features also contain some specialized features based on the core and the periphery segmentations.

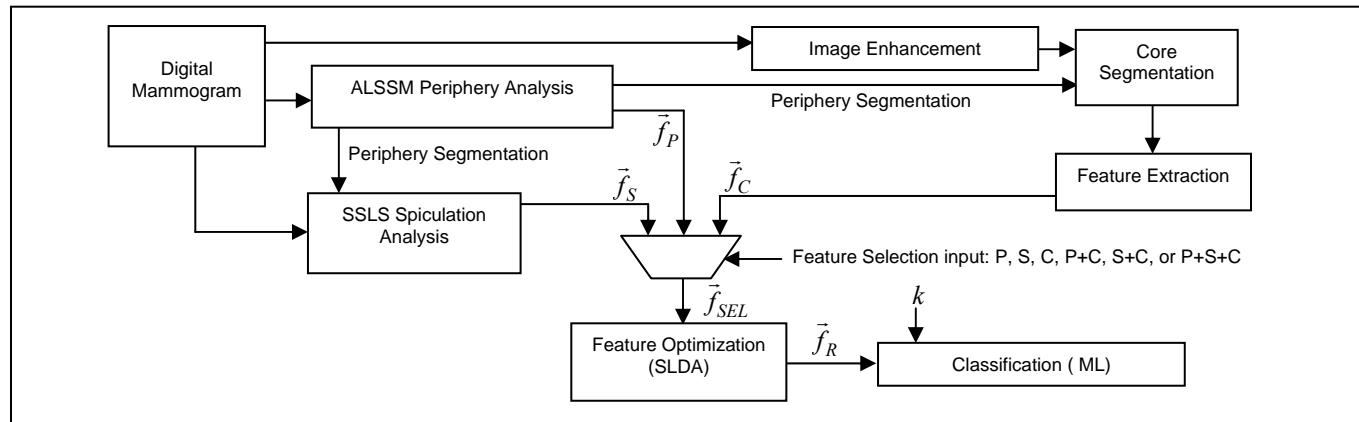


Figure 38 Proposed mammographic CAD system block diagram

The features are  $\vec{f}_p$  = periphery features,  $\vec{f}_s$  = spiculation features,  $\vec{f}_c$  = core features,  $\vec{f}_{SEL}$  = features after feature selector,  $\vec{f}_R$  = SLDA reduced feature. The feature sets all include the patient age as a feature. The feature combiner can select: periphery features (P), spiculation features (S), core features (C), periphery + core (P+C), spiculation + core (S+C), and periphery + spiculation + core (P+S+C), according to the feature selector input.

Table 16 Feature list for extended core features

Feature Set			Feature Type	Feature List	Number of Features
A	B	C			
•	•	•	Morphological	Ratios of standard morphological features	14
	•		Statistical	Ratios of statistical features (Graylevel std. Dev., Graylevel std. dev. ratio)	2
•	•		NRL Delta	Delta NRL Entropy, Length, Mean, Roughness, Std. dev., Zero crossing count	6
	•	•	Laws Texture	Laws features (reference section 8.2.4) for core, areas between core and periphery, and periphery.	153

Table 17 Feature list

Feature Set			Feature Type and Source <sup>1</sup>	Feature List	Number of Features	References
A	B	C				
•	•	•	Patient age (DDSM)	Age	1	[137,177]
•	•		Morphological (SB)	Area, Axis ratio, Box ratio, Circularity, Convex hull area, Eccentricity, Equivalent diameter, Extent, Extent ratio <sup>2</sup> , Major axis length, Minor axis length, Perimeter length, Solidity, Width to height ratio	14	[105]
•	•		Statistical (SB)	Graylevel mean, Graylevel std. dev., Graylevel std. dev. ratio <sup>3</sup>	3	[105]
•	•		NRL (SB)	Entropy, Length, Mean, Roughness, Std. dev., Zero crossing count	6	[105,172,174]
•	•	•	GLCM (SB)	(Note <sup>4</sup> ) Energy, Variance, Correlation, Inertia, Inverse Difference Moment, Entropy	144	[17,105,172,174]
•	•	•	GLCM (RBST)	(Note <sup>5</sup> ) Energy, Variance, Correlation, Inertia, Inverse Difference Moment, Entropy	864	[17]

Feature sets A and B are the same feature sets I and II in chapter IX. <sup>1</sup> This denotes the region from which the features are extracted. DDSM=DDSM database (there is no region, as the patient age is part of the database). SB=segmentation boundary. NRL stands for Normalized Radial Length. RBST=Rubber Band Straightening Transform [17]. GLCM stands for graylevel co-occurrence matrix. GLCM is also known as spatial graylevel dependence (SGLD). <sup>2</sup> The extent ratio is  $\max(\text{length}, \text{height}) / \min(\text{length}, \text{height})$ . <sup>3</sup> the Graylevel std. dev. ratio is the ratio of the std. dev. of the graylevels inside the segmentation to the std. dev. of graylevels outside the segmentation boundary and within 200 pixels of the segmentation boundary. <sup>4</sup> The GLCM SB features are calculated at distances  $d=\{1,2,4,6,8,10\}$  and directions  $\theta=\{0^\circ,45^\circ,90^\circ,135^\circ\}$ . There will be a total of 6 GLCM features x 6 distances x 4 angles for 144 features. <sup>5</sup> The RBST features are the same features as the GLCM SB features. The RBST uses a parameter  $k$  to choose how many pixels before and after are used to create the normal vector to the spiculation boundary [2]. The RBST features are calculated for distances  $k=\{2,4,6,8,10,12\}$  For each value of  $k$ , there will be 144 features generated. Therefore there are  $864 = 144 \times 6$  features.

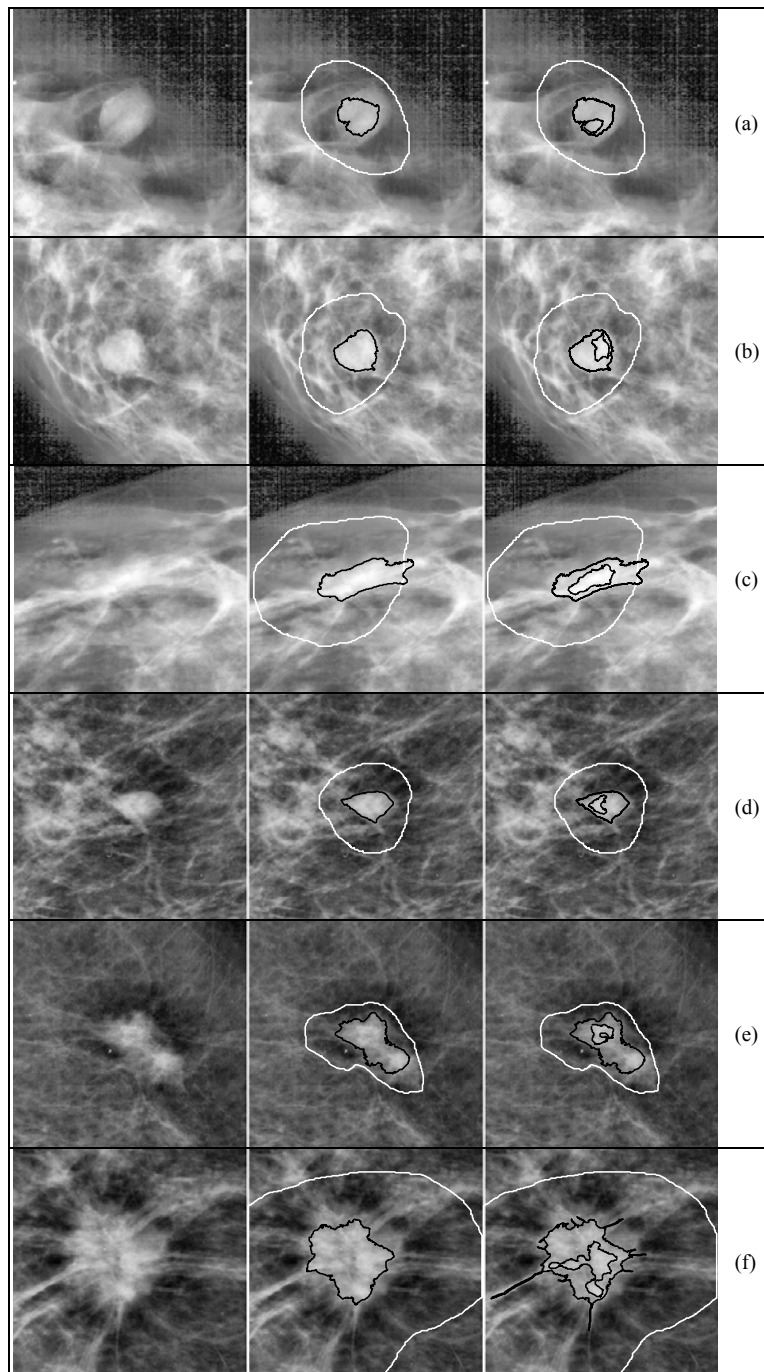


Figure 39 Example segmentations

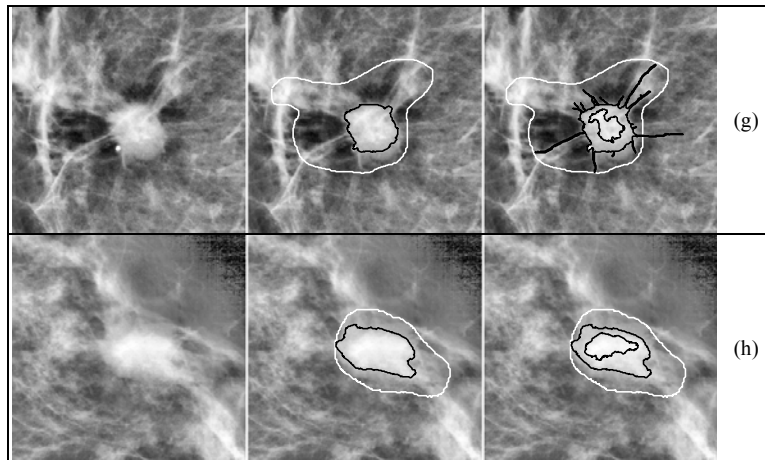


Figure 39 (continued)

For each set of images, on the left is the original mammogram, in the middle is the periphery and spiculation (if spiculated) segmentations (outer dark lines), and the physician ROI (white line), and on the right is the core (inner dark line), periphery and spiculation segmentations (outer dark lines), and the physician ROI (white line). (a)-(d) are benign cases, (d)-(h) are malignant cases.

Table 18 Features considered in this analysis

Feature Set	P	S	P+S	C+P	C+S	C+P+S
Periphery	•		•	•		•
Spiculation		•	•		•	•
Core				•	•	•

The user can then select which combinations of features to use, i.e. periphery only, spiculations only, core only, periphery and core, etc. For multiple segmentations, the features are concatenated into a larger feature set. Stepwise linear discriminant analysis (SLDA) with forward selection and backwards rejection is used to reduce the large number of potential features to a scalar feature. A limit is set so SLDA could select at most ten features. This limit is set because of the limited amount of training data available in this study. Since only 60 mammograms total are used, and a LOO method is employed, each iteration of the system testing is based on a training set of 59 cases. Limiting the SLDA feature selection to ten avoid overtraining and ensures proper covariance-matrix and inverse-matrix calculations in the SLDA implementation.

The last stage of an end-to-end CAD system is a classifier. The optimized features are passed to the classifier, and the mass is labeled as benign or malignant. In this study, a maximum-likelihood (ML) classifier is used to make a benign or malignant decision. Details on the ML classifier may be found in [193]. ML classifiers were used by [194] and [17] for digital mammography analysis, and are usually referred to as Bayesian classifiers in the medical literature.

### 8.2.2 Image Preprocessing for Core Segmentation

The mammogram image is preprocessed by a transformation to the polar domain around the geometric centroid of the periphery segmentation. The pixel mean values are calculated. A square mean filter sized five pixels radially by five degrees in the theta direction is applied to the polar image at each pixel. The filtered polar image is then multiplied pixel by pixel with the unfiltered polar image, in order to enhance the contrast. This enhanced image is then transformed back into the Cartesian domain. The final Cartesian enhanced image is denoted  $I_E$ , and this image is used by the core-segmentation system.

### 8.2.3 Level Set Core Segmentation

The level set segmentation starts by calculating the cumulative distribution function (CDF) of pixels in the periphery segmentation, using 200 bins. Let  $\phi_p(x, y)$  be the signed distance function (SDF) of the periphery segmentation. The SDF is defined as the smallest Euclidean distance to the segmentation boundary, with a positive (negative) sign inside (outside) the segmentation. Thus, the SDF on the periphery segmentation border or inside the periphery-segmentation area are less than or equal to zero. The initial core candidate region is defined by pixels satisfying the condition  $S_C(x, y) = 1$ , where

$$S_C(x, y) = H(C_p(x, y) - \alpha)H(\phi_p(x, y) - \beta). \quad (8.1)$$

and  $H(x)$  is the Heaviside step function, defined as  $H(x)=1$  if  $x \geq 0$  and  $H(x) = 0$  otherwise;  $C_p(x,y)$  is the CDF at location  $(x,y)$ ; the CDF threshold  $\alpha = 0.7$  is chosen experimentally; and  $\beta = -10$  is a constant used to force the core at least  $|\beta|$  pixels away from the periphery-segmentation border. This restriction forces a small gap between the core-segmentation boundary and the periphery boundary, which allows texture features to be calculated in the region between the core and periphery boundaries. Because of the step-function thresholding, this initial segmentation can contain more than one region, and can also contain small islands. For that reason, the initial core segmentation is set to the largest connected region defined by  $S_C = 1$ . The SDF  $\phi_C$  is then calculated from this region.

The Chan-Vese method is applied, with the inner region  $R$  set to the initial region described above, and the outer region set to the periphery segmentation. That is,  $\Omega = H(\phi_p - \beta)[1 - H(\phi_C)]$ . The level set is propagated with a time step  $\Delta t = 0.1$  and will stop if either (i) 500 iterations complete, or (ii) the segmentation changes less than four pixels in three consecutive iterations; these values are determined experimentally. Once the core segmentation stops, features are extracted.

#### 8.2.4 Feature Extraction, Optimization, and Classification

The features extracted include morphological features, statistical graylevel features, and texture features based on the segmentation boundary and the rubber band straightening transform (RBST) [146,147], as well as patient age. The features are described in Table 17, and detailed descriptions may be found in Table 17's references and in chapter IX. All features are extracted from the original mammogram image after cropping.

In addition to these standard features, a set of features based on the core and periphery segmentation are extracted, and are denoted extended core features. These features include morphological and statistical-feature ratios, a delta normalized radial length (DRNL) feature set,

and a set of texture features. All of these features are based on both the core and periphery segmentations. These core features are listed in Table 16.

For the morphological and statistical features, the ratios of the periphery features to the corresponding core features are calculated. For example, the morphological feature referred to as major-axis length ratio is the periphery major-axis length divided by the core major-axis length. The DNRL is the NRL of the periphery minus the NRL of the core. Note that the NRL vectors are usually not the same length, so the shortest NRL vector is interpolated using bilinear interpolation to have the same length of the longer vector. The DNRL features are differences in the core NRL and periphery NRL features. For example, the DNRL length feature is calculated as the length of the original core NRL vector minus the length of the original periphery NRL vector. A final set of texture features are created via the application of the 25 2D Laws texture kernels. The Laws texture features are described in section 5.5.3.2. To create the Laws texture features, a small image containing the core segmentation is extracted from the mammogram image. The image is convolved with each of the Laws 2D kernels. The L5L5 feature is a special Laws feature image is used to normalize all of the other laws feature images [178]. Thus, each image is then normalized by dividing pixel by pixel with the L5L5 image, and is termed  $I_m$  for each 2D Laws texture kernel  $m \in \{1, 2, \dots, 25\}$ . For each 2D Laws texture and each pixel in the convolved image, the following equation is used to calculate the texture for that pixel for the  $m$ -th texture:

$$L_m(x, y) = \sum_{j=-D}^D \sum_{k=-D}^D I_m(x+j, y+k), \quad (8.2)$$

where the texture mask size is  $(2D+1)$  by  $(2D+1)$ . The variable  $D$  is selected as 7, thus eq. (8.2) uses a  $15 \times 15$  region centered at each pixel for analysis. The Laws features are extracted for three regions: the core only, the periphery, and the region between the core and periphery. The laws features include three features for the mean value of the L5L5 image pixels for the three regions, and the standard deviation and entropy for each laws texture kernel for each region.

Therefore there are three mean features plus  $(25 \text{ kernels}) * (3 \text{ regions}) * (2 \text{ feature types}) = 3+150 = 153$  laws texture features.

Table 18 shows the various combinations of analysis. For instance, the features for the P+S case include the periphery features and the spiculation features. It is noted that age is included only once. That is, age is only allowed to be selected by SDLA once, even though age is in each feature set.

There are a large number of features, and the feature set must be reduced due to the limited training samples available. SLDA uses the area under the ROC curve ( $A_Z$ ) [191] with forward selection and backward rejection to optimally select up to ten features and project them to maximize class separation. The optimized features are then passed to the ML classifier to label the mass as malignant or benign.

#### 8.2.5 Analysis of Results

In this study, the performance of the core-segmentation features as compared to the features obtained with the periphery and spiculation segmentations is analyzed. These comparisons are conducted prior to classification using ROC  $A_Z$  values and paired  $t$ -test. Assuming an end-to-end system that uses a ML classifier, results are analyzed in terms of the overall accuracies (OA) in percent, as well as the number of false negatives (FN). For both analysis approaches, the LOO training/testing method is employed.

The  $t$ -test analysis is conducted in the following manner. Two segmentation approaches are selected for comparison. For each approach, LOO testing is conducted such that one mammogram is removed for testing. Then segmentation and SLDA is performed on the remaining 59 cases to determine an optimum scalar feature, and an  $A_Z$  value is calculated for the feature. The final result is 60  $A_Z$  values for each segmentation approach. A two-tailed paired samples  $t$ -test at the 95% confidence level is then conducted for the two sets of  $A_Z$  values. The resulting  $p$  value indicates whether or not the features resulting from the two segmentation approaches are significantly different, where  $p < 0.05$  indicates statistical significance.

The percentage of variance accounted for by adding the additional segmentation features,  $r^2$ , is also calculated. Values of  $r^2$  such that  $0.09 < r^2 < 0.25$  and  $r^2 > 0.25$  are considered medium and large effects, respectively [74]. The  $r^2$  value can also be interpreted as a percentage, i.e. 0.25 corresponds to 25 percent. This statistical measure shows how much of the variance is due to the combination of features versus features from a single segmentation. Reference pp. 333-343 and pp. 285-289 of [137,177] for discussion of the  $t$ -test and the  $r^2$  statistics, respectively.

### 8.3 Results and Discussion

#### 8.3.1 Segmentation Results

The following notation is used for the different combinations of features extracted from the three different segmentations: P denotes the periphery, C denotes the core, and S denotes Spiculations. A “+” will be used to indicate that features from multiple segmentations are utilized, e.g. P+C = Periphery and Core.

Figure 39 shows several example cases, with Figure 39 (a)-(d) showing benign cases and Figure 39 (e)-(h) showing malignant cases. In this figure, the core segmentations are shown along with the physician ROI and the periphery segmentations. In some cases, this is a simple nearly round region in the image, and in other cases the core is a more complicated shape, especially in many malignant images, which are shown in Figure 39 (e)-(h). The Chan-Vese method provides a robust framework for binary segmentation using level sets, and it provides an easy way to generate a segmentation where the variance is minimized, which is the goal of the proposed core segmentation algorithm.

#### 8.3.2 Feature Efficacies

The feature efficacies in terms of their  $A_Z$  values determined from SLDA during LOO analysis are shown in Figure 40 (a)-(c). Since LOO is used to train/test the system, and 60 mammogram masses are included in the study, 60  $A_Z$  values will result for each

segmentation/feature combination. Thus, the figures show the mean  $A_Z$  values as well as  $\pm$  one standard-deviation error bars. Note that the minimum  $A_Z$  value is 0.5, the maximum is 1.0, and a higher value is better than a lower value. Figure 40 (a) shows the morphological and NRL feature results. Figure 40 (b) shows the results of the statistical, SGLD segmentation and SGLD RBST features. Figure 40 (c) shows the extended core features. From Figure 40, the best features from the periphery are the area, convex-hull area, equivalent diameter, major- and minor-axis lengths, and length (of perimeter). The core features that provided some improvement are the major-axis length, perimeter length, and the NRL entropy, length, and roughness. The spiculation features in some cases provided a drastic improvement, such as the morphological-features box ratio, circularity, convex-hull area, extent, perimeter length, solidity, and in the NRL length, mean, roughness, and zero cross-count features.

Figure 40 (b) shows most of the statistical features are similar for the periphery, core, and spiculation segmentations. It should be noted from Figure 40 (a) and (b) that most of the core segmentation features are performing on par, or better, than the periphery features. Thus, the core approach could be useful in situations where the periphery segmentation is questionable, such as when the mass is not well-circumscribed. Figure 40 (c) shows the extended core feature  $A_Z$  values, and the most effective of these are the area ratio, equivalent diameter ratio, length delta, and Laws features.

From Figs. 4-6, it is clear that the best individual features are several of the spiculation morphological and NRL features. Since a spiculated mass has a central solid area and small, fingerlike projections, this behavior is expected. A few of the spiculation segmentation features result in  $A_Z$  values approaching 0.9, which is very impressive. However, it should be noted that in this study about half of the malignant masses are spiculated, and this is not indicative of what would be encountered in a typical clinical study.

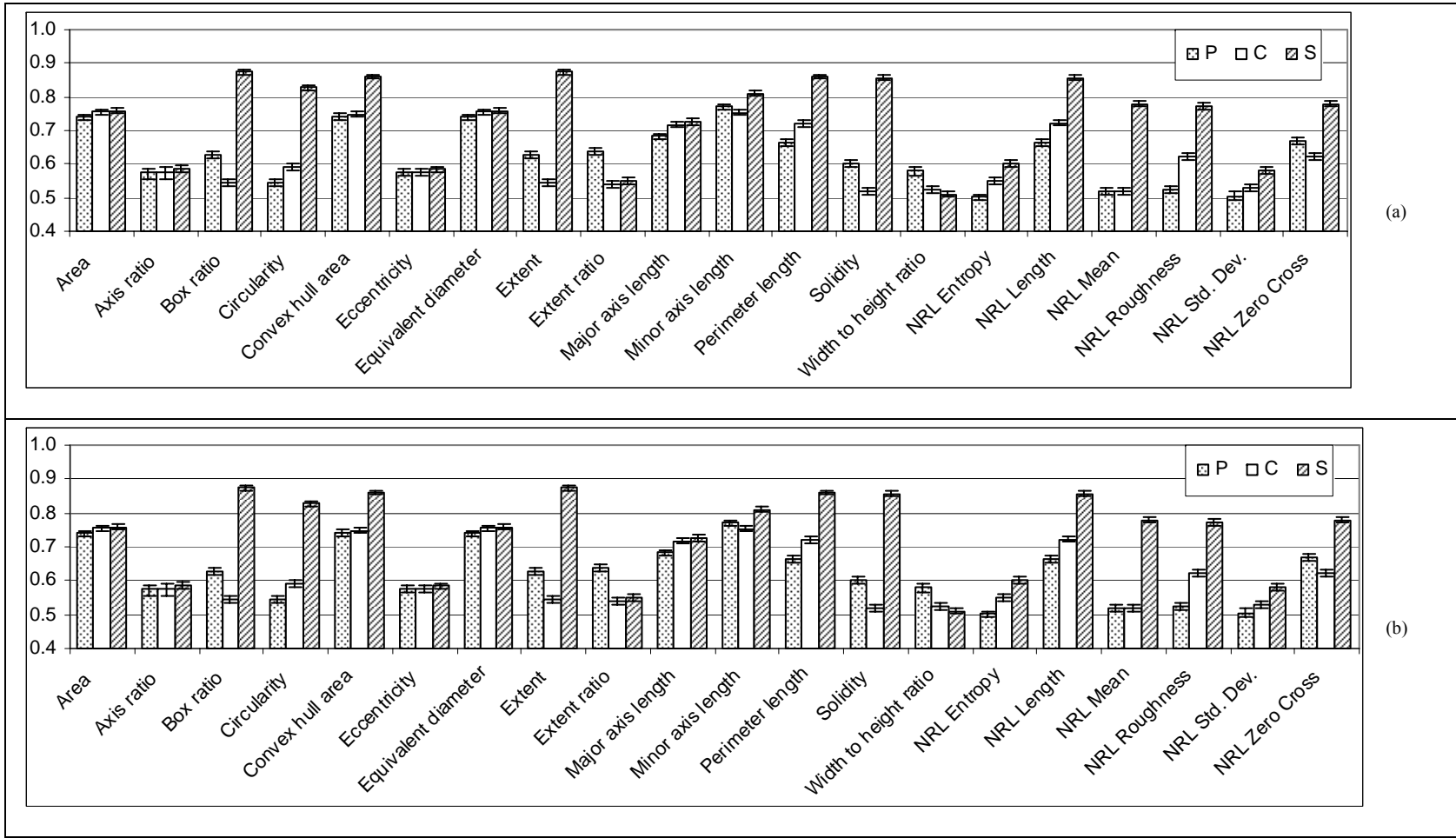


Figure 40 SLDA LOO  $A_z$  values

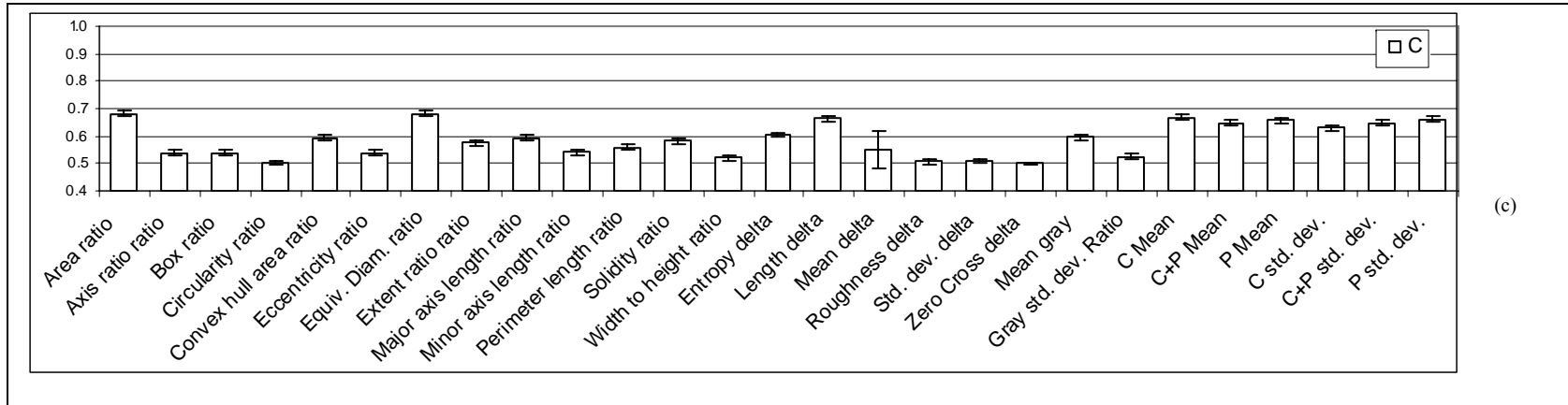


Figure 40 (continued)

C=Core, P=Periphery, S=Spiculations. Features shown: (a) Morphological and NRL. (b) Statistical and SGLD. (c) Extended core. Error bars show  $\pm 1$  std. dev. The y-axis is LOO ROC  $A_Z$ .

Table 19 Mean LOO ROC  $A_Z$  values and 95 % confidence interval

Segmentation	A	B	C	Segmentation	A	B	C
C	0.9702 $\pm$ 0.0010	0.9716 $\pm$ 0.0012	0.9717 $\pm$ 0.0022	C+P	0.9645 $\pm$ 0.0008	0.9674 $\pm$ 0.0010	0.9717 $\pm$ 0.0022
P	0.9787 $\pm$ 0.0011	0.9708 $\pm$ 0.0011	0.9679 $\pm$ 0.0013	C+S	0.9861 $\pm$ 0.0007	0.9861 $\pm$ 0.0007	0.9827 $\pm$ 0.0014
S	0.9862 $\pm$ 0.0011	0.9862 $\pm$ 0.0013	0.9849 $\pm$ 0.0011	C+P+S	0.9858 $\pm$ 0.0007	0.9858 $\pm$ 0.0007	0.9827 $\pm$ 0.0014

Segmentations: C=Core, P=Periphery, S=Spicules, C+P=Core and Periphery, C+S=Core and Spiculations, C+P+S=Core, Periphery, and Spiculations

Table 19 compares the  $A_Z$  values for the optimum scalar feature (obtained with SLDA) for six segmentation approaches: core, periphery, spiculation, core+periphery, core+spiculation, and core+periphery+spiculation. These results are shown for the three different feature sets (A,B,C) as defined in Table 17. Note that the  $A_Z$  values are very high for all test combinations. This makes it quite difficult to determine which combinations are truly outperforming the others, i.e., whether the addition of the core segmentation features improve the results.

To aid analysis, a paired  $t$ -test of the LOO  $A_Z$  values are shown in Table 20. From Table 20, it can be seen that all feature set comparisons are statistically significant except for core versus spiculation segmentation with feature-set C (patient age, GLCM features, and the core extended morphological and laws texture features). There are several cases where the paired samples show improvement in the mean feature efficacy, and are shown in bold in the rightmost column of Table 20. For feature sets B and C, adding the core features slightly enhances the overall LOO  $A_Z$  values. Most of the difference category values are small, since the overall LOO  $A_Z$  values are all very high.

Table 20 Paired *t*-test statistical results for LOO ROC  $A_z$  values

FS	Seg 1	Seg 2	p	$r^2$	mean of difference
A	C	P	<0.001	<b>0.78</b>	-0.0085
	C	S	<0.001	<b>0.54</b>	-0.0160
	C+P	P	<0.001	<b>0.92</b>	-0.0143
	C+S	S	<0.001	0.06	-0.0001
	C+P+S	P+S	<0.001	<b>0.48</b>	<b>0.0032</b>
B	C	P	<0.001	0.11	<b>0.0038</b>
	C	S	<b>0.005</b>	0.08	-0.0132
	C+P	P	<0.001	0.11	<b>0.0038</b>
	C+S	S	<b>0.008</b>	0.15	-0.0021
	C+P+S	P+S	<0.001	0.08	-0.0018
C	C	P	<b>0.024</b>	0.02	<b>0.0008</b>
	C	S	0.328	0.01	-0.0146
	C+P	P	<0.001	<b>0.39</b>	-0.0034
	C+S	S	<0.001	0.04	-0.0001
	C+P+S	P+S	<0.001	<b>0.48</b>	<b>0.0032</b>

FS = Feature Set (Reference Tables I and II). Segmentations: C=Core, P=Periphery, S=Spicules. The *t*-test compares the differences of LOO ROC  $A_z$  values: i.e.  $D = (\text{LOO ROC } A_z \text{ Seg 1}) - (\text{LOO ROC } A_z \text{ Seg 2})$ . The mean of difference column is the mean of  $D$ , and mean values where the core increases  $A_z$  are shown in bold. Statistically significant results are when  $p < 0.05$  and are shown in bold. A large effect in percentage of variance explained ( $r^2 > 0.25$ ) is in bold.

### 8.3.3 Overall Results

Table 21 shows the overall classification accuracies (OA) and number of FN when using a ML classifier. Generally, combinations of segmentations are not considered (i.e. core only, periphery only, spiculation only), since the core-segmentation features do not perform as well as the periphery or spiculation features. However, combining the core features with periphery or spiculation features often provides added value. For example, when using feature set A, adding the core features to the periphery features increases the overall classification accuracy from 80% to 83% and reduces the FN from 9 to 7.

Table 21 Overall accuracies (OA) in percent and number of false negatives (FN)

Feature Set	Overall Accuracy (%)						Number of False Negatives					
	C	P	S	C+P	C+S	C+P+S	C	P	S	C+P	C+S	C+P+S
A	78	80	88	83	88	90	8	9	5	7	4	4
B	83	87	88	82	90	90	4	4	5	7	4	4
C	88	87	90	88	88	90	5	4	3	4	2	2

P=Periphery, C=Core, S=Spicules, C+P=Core + Periphery, C+S=Core + Spiculations, C+P+S=Core + Periphery + Spiculations. Features A, B, and C are defined in Table 18 and Table 20.

However, it should be noted that in some instances the OA is decreased by adding the core features. In fact, in several cases the OA does not follow the trend of the  $A_z$  values shown in Table 19. The decrease in OA due to an increase in the number of features is a classic example of the well-known Hughes phenomenon. This is due to the fact that the limited number of training images in this study (59 during a given iteration of the LOO testing) is significantly restricting the ability of the system to select a true optimum feature set via SLDA. In order to ensure proper SLDA calculations, the SLDA feature selection was restricted to a maximum of ten features. If more training images are included, then SLDA could be allowed to select more features to form the optimum scalar, and a more stable and reliable scalar feature could be achieved.

#### 8.4 Conclusions

This chapter presented a mammographic mass-core segmentation method based on the Chan-Vese level set method, which produces a segmentation based on a minimal-variance criterion. The method is shown to be well-suited for core segmentation, since mass cores typically have a high graylevel mean and low variance. The core-segmentation method is analyzed via resulting feature efficacies. Additionally, the core segmentation method is used to investigate the idea of a three-stage segmentation approach, i.e., segment the mass core, periphery, and

spiculations (if any exist), and use features from these three segmentations to classify the mass as either benign or malignant.

Morphological and texture features extracted from the core segmentation are shown to be effective and comparable to those extracted from a periphery segmentation. The ROC  $A_z$  values for most of the core features are on par, or better, when compared to the periphery-segmentation features. The efficacy of the core features when combined with the periphery and spiculation features are feature-set dependent. However, all feature combinations that are investigated resulted in  $A_z$  values that are very high and made comparisons difficult.

In this study, however, the feature efficacies are limited because of the small number of training images, i.e. small relative to the very large number of potential features, which are particularly large when the three segmentation approaches are combined. Since SLDA is used for feature selection and optimization, the number of selected features are limited to ten, and as a result the overall classification accuracies are relatively low and unstable, i.e., suffering from the Hughes phenomenon. With a much larger dataset, more features could be used to form the feature vector resulting in a more stable and reliable feature vector (or scalar feature if using a reduction technique like SLDA). As a result, CAD systems that segment the mass periphery only could benefit from adding a core segmentation and resulting core features.

# CHAPTER IX

## CONCLUSIONS

### 9.1 Conclusions

In this dissertation, level set methods are employed to segment masses in digital-mammographic images. The focus of this dissertation is level set based segmentation. End-to-end image-processing systems are implemented and tested. These systems included stages for image preprocessing, image segmentation, feature extraction, feature reduction and optimization, and classification. The proposed level set methods are embedded in these end-to-end systems for analysis and validation purposes. Standard features are used in the mammography analysis and new features based on spectral discrimination metrics are designed and validated for the hyperspectral analysis.

In digital mammography, a three-stage method is developed for analyzing digital mammograms. The stages are segmentation of the mass periphery, mass spicules, and mass core. The periphery segmentation started from a seed point and used the narrowband level set method in conjunction with an adaptive speed function based on a measure of the boundary complexity in the polar domain. The boundary complexity term allowed the mass to be delineated even when the masses had ill-defined and irregularly shaped borders. Segmentation is performed in the polar domain because it facilitates the creation of the adaptive speed function used to control the level set propagation. To the best of my knowledge, this method is the first method to use narrowband level sets to segment mammographic mass peripheries, and the first to perform periphery segmentation in the polar domain. The proposed method outperformed a well-known previously published method [166] and compared favorably to other state-of-the-art methods.

For mammographic mass-spiculation segmentation, a modified form of the Dixon and Taylor Line Operator (DTLO), denoted generalized DTLO (GDTLO), is developed and used to analyze mammographic images to determine if spicules are present. If spicules are detected, then the areas around the mass border are analyzed, and if they met the criteria for a spicule, then the linear filaments are segmented using the narrowband level set method. The spiculation features proved to be very beneficial in classification and results improved dramatically when comparing the periphery only to the spiculation-segmentation results. The main improvements are seen in the morphological, normalized radial length, and statistical features, which is expected, since many of these features are heavily influenced by the shape of the segmented mass.

In the core segmentation, the Chan-Vese method is employed to extract a high graylevel mean and low graylevel variance portion from within the periphery. The Chan-Vese level set method enabled a simple segmentation of the core. The core features are effective and comparable to periphery features when analyzed independently. Most mammographic CAD systems use only a periphery segmentation, so they could potentially benefit from core features. Also, in some cases, adding core features is able to lower the number of false negatives.

When analyzing combinations of features, adding the spiculation features is very beneficial. The efficacies of the combined methods are feature-set dependent and classifier dependent. Since there are only sixty mammograms in this test study, this limited the number of features that the feature-reduction and optimization method, namely stepwise linear discriminant analysis, is able to use. In a system where there is much more training data, then the combination of core, periphery, and spiculation features could provide substantial improvements to systems that use the periphery alone. Several of the core morphological and NRL features showed improved leave-one-out ROC  $A_z$  values compared to the corresponding periphery features.

In all of these methods, using the narrowband level set method provided a fast implementation, which is also flexible, allowing regions to grow, merge, split, appear, disappear, etc. This is handled naturally by the level set method. The exact same level set code is used in each segmentation study, and the main contributions for the periphery, spiculation, and

hyperspectral classification chapters are in design and validation of customized speed functions to control the level set propagation and force vicinal areas to be more homogeneous.

## 9.2 Suggested Future Work

Suggested future work for the mammographic mass-periphery segmentation includes: (1) modifying the speed function so that under-segmentation is minimized, (2) using more powerful classifiers such as kernel-based general discriminant analysis or support vector machines, (3) using automated seed-point determination routines instead of using the physician ROI, in order to create a more automated CAD system, (4) replacement of the initial isotropic Gaussian filter with a filter which models the natural shape of the tumor, such as a 2D Gaussian aligned along the principal axes of the mass PDF.

For the mammographic mass-spiculation segmentation, suggested future work includes: (1) investigating the robustness of the detection algorithm to variations in the periphery segmentation (i.e. undersegmentation to oversegmentation), and (2) conducting more extensive validation with a larger dataset or on digital mammograms from other databases.

For the mammographic mass-core segmentation, suggested future work includes the following. (1) Instead of applying Chan-Vese on the pixels (after denoising) alone, a vector version could be applied, where each pixel is now a vector based on local texture analysis. This textural analysis could be from wavelets, for instance. (2) Modify the method to not require an initial periphery segmentation. This would require the addition of terms to penalize area and border length, such as those employed in the periphery section. This could be beneficial in cases where the mass periphery is difficult to delineate.

For the combined three stage segmentation approach (periphery, spiculations, and core), suggested future work is to try a multiclassifier-based decision-fusion system, rather than simply stacking all the features into one large feature vector. An intelligent system which groups certain similar features together could provide better classification results.

## REFERENCES

- [1] R.C. Gonzalez and R.E. Woods, *Digital Image Processing*, 2nd ed. Upper Saddle River, NY: Prentice Hall, 2002.
- [2] R.O. Duda, P.E. Hart, and D.G. Stork, *Pattern Classification*, 2nd ed. New York: John Wiley & Sons, 2001.
- [3] J.A. Sethian, "A fast marching level set method for monotonically advancing fronts," *Proc. of the National Academy of Sciences*, vol. 93, no. 4, pp. 1591-1595, 1996.
- [4] J.A. Sethian, *Level Set Methods and Fast Marching Methods: Evolving Interfaces in Computational Geometry, Fluid Mechanics, Computer Vision, and Materials Science*, 2nd ed. Cambridge, UK: Cambridge University Press, 2002.
- [5] S.C. Zue and A. Yuille, "Region competition: unifying snakes, region growing, and Bayes/MDL for multiband image segmentation," *IEEE Trans. on Pattern Analysis and Machine Intelligence*, vol. 18, no. 9, pp. 884-900, Sept. 1996.
- [6] R. Kimmel, "Fast Edge Integration," in *Geometric Level Set Methods in Imaging, Vision, and Graphics*, S. Osher and N. Paragios, Eds. New York, NY: Springer, pp. 59-77, 2003.
- [7] N. Paragios, "Geodesic active regions and level set methods: contributions and applications in artificial vision." PhD in Computer Engineering. Sophia Antipolis, France: University of Nice, Jan. 2000.
- [8] A. Jemal, T. Murray, E. Ward, A. Samuels, R.C. Tiwari, A. Ghafoor, E.J. Feuer, and M.J. Thun, "Cancer Statistics, 2005," *CA: A Cancer Journal for Clinicians*, vol. 55, no. 1, pp. 10-30, 2005.
- [9] H. Kobatake, Y. Yoshinaga, and M. Murakami, "Automatic detection of malignant tumors on mammogram," *Proc. of the IEEE Intl. Conference on Image Processing (ICIP-94)*, Austin, TX, vol. 1, pp. 407-410, Nov. 1994.
- [10] I.N. Bankman, W.A. Christens-Barry, I.N. Weinberg, D.W. Kim, R.D. Semmel, and W.R. Brody, "An algorithm for early breast cancer detection in mammograms," *Proc. of the Fifth Annual IEEE Symposium on Computer-Based Medical Systems*, Durham, NC, pp. 362-369, Jun. 1992.
- [11] M. Sameti, R.K. Ward, B. Palcic, and J. Morgan-Parkes, "Texture feature extraction for tumor detection in mammographic images," *Proc. of the 1997 IEEE Pacific Rim Conference on Communications, Computers and Signal Processing (PACRIM)*, Victoria, BC, vol. 2, pp. 831-834, Aug. 1997.

- [12] American Cancer Society, "Finding Breast Cancer Early," in *CA: A Cancer Journal for Clinicians*, vol. 53, no. 3, pp. 170-171, 2003. Available: <http://caonline.amcancersoc.org>
- [13] W. Qian, L.P. Clarke, Z. Baoyu, M. Kallergi, and R. Clark, "Computer assisted diagnosis for digital mammography," *IEEE Engineering in Medicine and Biology Magazine*, vol. 14, no. 5, pp. 561-569, Sep.-Oct. 1995.
- [14] B. Sahiner, N. Petrick, C. Heang-Ping, L.M. Hadjiiski, C. Paramagul, M.A. Helvie, and M.N. Gurcan, "Computer-aided characterization of mammographic masses: accuracy of mass segmentation and its effects on characterization," *IEEE Trans. on Medical Imaging*, vol. 20, no. 12, pp. 1275-1284, Dec. 2001.
- [15] L.M. Bruce and R.R. Adhami, "Classifying mammographic mass shapes using the wavelet transform modulus-maxima method," *IEEE Trans. on Medical Imaging*, vol. 18, no. 12, pp. 1170-1177, Dec. 1999.
- [16] M. Heath, K.W. Bowyer, D. Kopans, W. Kegelmeyer, R. Moore, K. Chang, and S. Munishkumaran, "Current status of the Digital Database for Screening Mammography," in *Digital Mammography*, N. Karssemeijer, M. Thijssen, J. Hendriks, and L. van Erning, Eds. Boston, MA: Kluwer Academic Publishers, pp. 457-460, 1998.
- [17] B. Sahiner, H.-P. Chan, N. Petrick, M.A. Helvie, and M.M. Goodsitt, "Computerized characterization of masses on mammograms: The rubber band straightening transform and texture analysis," *Medical Physics*, vol. 25, no. 4, pp. 516-526, Apr. 1998.
- [18] J.E. Ball and L.M. Bruce, "Level Set Hyperspectral Image Segmentation and Classification via Spectral Band Selection and Optimized Pixel Discrimination Metrics," *IEEE Trans. on Geoscience and Remote Sensing*, 2007 [under review].
- [19] J.E. Ball and L.M. Bruce, "Level set segmentation of remotely sensed hyperspectral images," *Proc. of the IEEE Intl. Conference Geoscience and Remote Sensing (IGARSS)*, Anchorage, AL, vol. 8, pp. 5638 - 5642, Jul. 2005.
- [20] J.E. Ball and L.M. Bruce, "Accuracy analysis of hyperspectral imagery classification using level sets," *Proc. of the 2006 American Society of Photogrammetry and Remote Sensing Annual Conference*, Reno, NV, Apr. 2006.
- [21] J.E. Ball and L.M. Bruce, "Level Set Hyperspectral Segmentation: Near-Optimal Speed Functions using Band Selection and Scaled Spectral Angle Mapper," *Proc. of the 2006 IEEE Intl. Geoscience and Remote Sensing Symposium*, pp. 2596 - 2600, Jul. 2006.
- [22] J.E. Ball, T.W. Butler, and L.M. Bruce, "Towards automated segmentation and classification of masses in mammograms," *Proc. of the 26th Annual Intl. Conference of the Engineering in Medicine and Biology Society*, San Francisco, CA, vol. 1, pp. 1814-1817, 2004.
- [23] R.N. Dixon and C.J. Taylor, "Automated Asbestos Fiber Counting," *1979 Inst. Physics Conference*, vol. 44, pp. 178-185, 1979.
- [24] T.F. Chan and L.A. Vese, "Active contours without edges," *IEEE Trans. on Image Processing*, vol. 10, no. 2, pp. 266-277, 2001.

- [25] S. Osher and N. Paragios, "Level Set Methods," in *Geometric Level Set Methods in Imaging, Vision, and Graphics*, S. Osher and N. Paragios, Eds. New York, NY: Springer, pp. 1-20, 2003.
- [26] J.A. Sethian, "An analysis of Flame propagation." PhD in Applied Mathematics. Berkeley, CA: University of California, Berkeley, May 20, 1982.
- [27] D.L. Chopp, "Computing minimal surfaces via level set curvature flow," *Journal of Computational Physics*, vol. 106, no. 1, pp. 77-91, May 1993.
- [28] J.S. Suri and S. Laxminarayan, ed., *PDE & Level Sets: Algorithmic Approaches to Static and Motion Imagery*. New York: Kluwer Academic, 2002.
- [29] T. Chan and Z. Wei, "Level set based shape prior segmentation," *Proc. of the IEEE Computer Society Conference on Computer Vision and Pattern Recognition*, vol. 2, pp. 1164-1170, 20-25 Jun. 2005.
- [30] A. Tsai, A. Yezzi, Jr., W. Wells, C. Tempany, D. Tucker, A. Fan, W.E. Grimson, and A. Willsky, "A shape-based approach to the segmentation of medical imagery using level sets," *IEEE Trans. on Medical Imaging*, vol. 22, no. 2, pp. 137-154, Feb. 2003.
- [31] W. Ying, X. Xin-he, J. Tong, and Z. Da-zhe, "An Optimal Level Sets Method for Lung Nodules Detection in CT Images," *Proc. of the Sixth Intl. Conference on Intelligent Systems Design and Applications*, Jian, China, vol. 2, pp. 251-255, Oct. 2006.
- [32] M.F. Hansen, R. Larsen, B. Ersboll, and L.B. Christensen, "Coupled Shape Model Segmentation in Pig Carcasses," *Proc. of the 18th International Conference on Pattern Recognition*, vol. 1, pp. 468-471, 2006.
- [33] J.S. Suri, S. Singh, and S. Laxminarayan, "Medical image segmentation using level sets," in *PDE & Level Sets: Algorithmic Approaches to Static and Motion Imagery*, J. S. Suri and S. Laxminarayan, Eds. New York: Kluwer Academic, pp. 301-340, 2002.
- [34] D.H. Chung and G. Sapiro, "Segmenting skin lesions with partial-differential-equations-based image processing algorithms," *IEEE Trans. on Medical Imaging*, vol. 19, no. 7, pp. 763-767, Jul. 2000.
- [35] L. Pan, Z. Chong-Xun, and Y. Yong, "Model-based medical image segmentation: a level set approach," *Proc. of the Fifth World Congress on Intelligent Control and Automation (WCICA)*, vol. 6, pp. 5541-5544, Jun. 2004.
- [36] L. Pan, Y. Xiangguo, Z. Chongxun, and Y. Yong, "Medical image segmentation based on Mumford-Shah model," *Proc. of the Intl. Conference on Communications, Circuits and Systems (ICCCAS)* vol. 2, pp. 942-945, Jun. 2004.
- [37] M.E. Leventon, E. Grimson, O. Faugeras, R. Kikinis, and W.M. Well, III, "Knowledge-Based Segmentation of Medical Images," in *Geometric Level Set Methods in Imaging, Vision, and Graphics*, S. Osher and N. Paragios, Eds. New York, NY: Springer, pp. 401-419, 2003.

- [38] N. Paragios, "A variational approach for the segmentation of the left ventricle in MR cardiac images," *Proc. of the IEEE Workshop on Variational and Level Set Methods in Computer Vision* Vancouver, BC, pp. 153-160, Jul. 2001.
- [39] K. Seongjai and L. Hyeona, "A hybrid level set segmentation for medical imagery," *Proc. of the 2005 IEEE Nuclear Science Symposium Conference Record*, vol. 3 (CD-ROM), Oct. 2005.
- [40] M.E. Leventon, O. Faugeras, W.E.L. Grimson, and W.M. Well, III, "Level set based segmentation with intensity and curvature priors," *Proc. of the 5th IEEE EMBS Intl. Summer School on Biomedical Imaging* p. 8 pp., Jun. 2002.
- [41] S. Il-hong, K. Min-Jeong, C. Sung-Taek, and P. Hyun Wook, "Segmentation and visualization of left ventricle in MR cardiac images," *Proc. of the International Conference on Image Processing (ICIP)*, vol. 2, pp. II-89 - II-92, 2002.
- [42] Y. Yang, L. P., C. Zheng, and X. Yan, "A Robust Level Set Framework For Medical Image Segmentation," *Proc. of the Intl. Conference on Communications, Circuits, and Systems*, vol. 2, pp. 937 – 941, Jun. 2004.
- [43] A. Yezzi, Jr., S. Kichenassamy, A. Kumar, P. Olver, and A. Tannenbaum, "A geometric snake model for segmentation of medical imagery," *IEEE Trans. on Medical Imaging*, vol. 16, no. 2, pp. 199-209, Apr. 1997.
- [44] F. Mendels, C. Heneghan, P.D. Harper, R.B. Reilly, and J.P. Thiran, "Extraction of the optic disk boundary in digital fundus images," *Proc. of the First Joint BMES/EMBS Conference* Atlanta, GA, vol. 2, p. 1139, Oct. 1999.
- [45] U. Bottigli and B. Golosio, "Feature extraction from mammographic images using fast marching methods," *Nuclear Instruments and Methods in Physics Research Section A: Accelerators, Spectrometers, Detectors and Associated Equipment*, vol. 487, no. 1-2, pp. 209-215, Jul. 2002.
- [46] L. Yin, S. Deshpande, and J.K. Chang, "Automatic lesion/tumor detection using intelligent mesh-based active contour," *Proc. of the 15th IEEE Intl. Conference on Tools with Artificial Intelligence* pp. 390-397, Nov. 2003.
- [47] I. Dydenko, D. Friboulet, I.E. Magnin, J. D'Hooge, and B. Bijnens, "Segmentation and tracking of the cardiac muscle in echocardiographic sequences using a level set approach," *Proc. of the IEEE Symposium on Ultrasonics* vol. 1, pp. 21-24 Vol.21, Oct. 2003.
- [48] C. Baillard, P. Hellier, and C. Barillot, "Segmentation of 3D brain structures using level sets and dense registration," *Proc. of the IEEE Workshop on Mathematical Methods in Biomedical Image Analysis* pp. 94-101, Jun. 2000.
- [49] J.S. Suri, L. Kecheng, S. Singh, S.N. Laxminarayan, Z. Xiaolan, and L. Reden, "Shape recovery algorithms using level sets in 2-D/3-D medical imagery: a state-of-the-art review," *IEEE Trans. on Information Technology in Biomedicine*, vol. 6, no. 1, pp. 8-28, Mar. 2002.
- [50] R. Malladi and J.A. Sethian, "A real-time algorithm for medical shape recovery," *Proc. of the Intl. Conf. on Computer Vision*, Mumbai, India, pp. 304-310, Jan. 1998.

- [51] F. Dibos, G. Koepfler, and P. Monasse, "Total Variation Minimization for Scalar/Vector Regularization," in *Geometric Level Set Methods in Imaging, Vision, and Graphics*, S. Osher and N. Paragios, Eds. New York, NY: Springer, pp. 121-140, 2003.
- [52] L. Rudin, S. Osher, and E. Fatemi, "Nonlinear Total Variation-Based Noise Removal Algorithms," *Modelisations Mathematiques pour le traitement d'images, INRIA*, pp. 149-179, 1992.
- [53] J.A. Sethian, "Optimality and First Arrivals," in *Level Set Methods and Fast Marching Methods: Evolving Interfaces in Computational Geometry, Fluid Mechanics, Computer Vision, and Materials Science*, 2nd ed, P. G. Ciarlet, A. Iserles, R. V. Kohn, and M. H. Wright, Eds. Cambridge, UK: Cambridge University Press, pp. 284-312, 2002.
- [54] J.A. Sethian, "Etching and Deposition in Microchip Fabrication," in *Level Set Methods and Fast Marching Methods: Evolving Interfaces in Computational Geometry, Fluid Mechanics, Computer Vision, and Materials Science*, 2nd ed, P. G. Ciarlet, A. Iserles, R. V. Kohn, and M. H. Wright, Eds. Cambridge, UK: Cambridge University Press, pp. 313-356, 2002.
- [55] N. Paragios and R. Deriche, "Variational Principles in Optical Flow Estimation Tracking," in *Geometric Level Set Methods in Imaging, Vision, and Graphics*, S. Osher and N. Paragios, Eds. New York, NY: Springer, pp. 299-318, 2003.
- [56] S. Soatto, A. Yezzi, Jr., and A. Duci, "Region matching and tracking under deformations or occlusions," in *Geometric Level Set Methods in Imaging, Vision, and Graphics*, S. Osher and N. Paragios, Eds. New York, NY: Springer, pp. 319-340, 2003.
- [57] N. Paragios and R. Deriche, "Geodesic active contours and level sets for the detection and tracking of moving objects," *IEEE Trans. on Pattern Analysis and Machine Intelligence*, vol. 22, no. 3, pp. 266-280, Mar. 2000.
- [58] A.S. El-Baz, A.A. Farag, H.A. El Munim, and S.E. Yuksel, "Level Set Segmentation Using Statistical Shape Priors," *Proc. of the Conference on Computer Vision and Pattern Recognition Workshop* pp. 78-78, Jun. 2006.
- [59] D. Cremers, "Dynamical statistical shape priors for level set-based tracking," *IEEE Trans. on Pattern Analysis and Machine Intelligence*, vol. 28, no. 8, pp. 1262-1273, Aug. 2006.
- [60] M.E. Leventon, W.E.L. Grimson, and O. Faugeras, "Statistical shape influence in geodesic active contours," *Proc. of the 5th IEEE EMBS Intl. Summer School on Biomedical Imaging* p. 8 pp., Jun. 2002.
- [61] B. Vemuri and Y. Chen, "Joint Image Registration and Segmentation," in *Geometric Level Set Methods in Imaging, Vision, and Graphics*, S. Osher and N. Paragios, Eds. New York, NY: Springer, pp. 251-269, 2003.
- [62] R. Fedkiw, "Simulating Natural Phenomena," in *Geometric Level Set Methods in Imaging, Vision, and Graphics*, S. Osher and N. Paragios, Eds. New York, NY: Springer, pp. 461-480, 2003.

- [63] J.E. Ball and L.M. Bruce, "Level Set Hyperspectral Image Segmentation and Classification via Spectral Band Selection and Optimized Pixel Discrimination Metrics," *IEEE Trans. on Geoscience and Remote Sensing*, 2006 [under review].
- [64] F. Dell'Acqua, P. Gamba, and P. Prevedini, "Level-set based extraction and tracking of meteorological objects in satellite images," *Proc. of the IEEE Intl. Geoscience and Remote Sensing Symposium*, vol. 2, pp. 627-629, Jul. 2000.
- [65] T. Keaton and J. Brokish, "A level set method for the extraction of roads from multispectral imagery," *Proc. of the 31st Applied Imagery Pattern Recognition Workshop*, pp. 141-147, Oct. 2002.
- [66] Y. Yang and H. Ma, "Level Set Evolution Based Logic Fusion: A Novel Man-made Objects Segmentation from Radar Image," *Proc. of the 2006 Intl. Conference on Computational Intelligence and Security* vol. 2, pp. 1700-1705, Nov. 2006.
- [67] R. Malladi and J.A. Sethian, "Level set and fast marching methods in image processing and computer vision," *Proc. of the Intl. Conference on Image Processing (ICIP)*, Lausanne, vol. 1, pp. 489-492, Sept. 1996.
- [68] G. Hughes, "On the mean accuracy of statistical pattern recognizers," *IEEE Trans. on Information Theory*, vol. 14, no. 1, pp. 55-63, 1968.
- [69] S. Venkataraman, L.M. Bruce, A. Cheriyyadat, and A. Mathur, "Hyperspectral dimensionality reduction via localized discriminant bases," *Proc. of the IEEE Intl. Geoscience and Remote Sensing Symposium*, Seoul, Korea, vol. 2, pp. 1245-1248, Jul. 2005.
- [70] K. Fukunaga and R.R. Hayes, "Effects of sample size in classifier design," *IEEE Trans. on Pattern Analysis and Machine Intelligence*, vol. 11, no. 8, pp. 873-885, Aug. 1989.
- [71] D.A. Landgrebe, *Signal Theory Methods in Multispectral Remote Sensing*. Hoboken, NJ: Wiley, 2003.
- [72] K. Fukunaga, *Introduction to Statistical Pattern Recognition*, 2nd ed. San Francisco: Academic Press, 1990.
- [73] M. Nadler and E.P. Smith, *Pattern Recognition Engineering*. New York: Wiley-Interscience, pp. 350-356, 1993.
- [74] F.J. Gravetter and L.B. Wallnau, *Statistics for the Behavioral Sciences*, 7th ed. Belmont, CA: Thomson Wadsworth, 2007.
- [75] R.L. Egan, *Breast Imaging: Diagnosis and Morphology of Breast Diseases*. Philadelphia, PA: W. B. Saunders Co., 1988.
- [76] American Cancer Society, "American Cancer Society: Breast Cancer Facts & Figures 2005-2006," pp. 1-28, 2006. Available: <http://www.cancer.org/downloads/STT/CAFF2005BrF.pdf>.
- [77] *The Mosby Medical Encyclopedia*, Revised ed. New York, NY: The Penguin Group, 1992.

- [78] "Merriam-Webster's Medical Desk Dictionary Online," 2007. available: <http://www.healthline.com/dictionary/hamartoma>, Feb. 2007.
- [79] H.L. Kundel and P.B. Dean, "Tumor Imaging," in *Image Processing Techniques for Tumor Detection*, R. N. Strickland, Ed. New York, NY: Marcel Dekker, Inc., pp. 1-18, 2002.
- [80] S.M. Love and K. Lindsey, *Dr. Susan Love's Breast Book*. Cambridge, MA: Da Capo, 2005.
- [81] K.M. Willison, "Breast anatomy and physiology," in *Mammographic Imaging: A Practical Guide* New York, NY: Lippincott Williams & Wilkins, pp. 119-161, 1992.
- [82] M.J. Yaffe, "Mammography," in *Biomedical Imaging*: CRC Press, pp. 8-19 - 18-36, 2003.
- [83] R.M. Rangayyan, "The Nature of Biomedical Images," in *Biomedical Image Analysis*, M. R. Neuman, Ed. Boca Raton, FL: CRC Press, pp. 22-27, 2005.
- [84] J. Spratt and J. Spratt, "Growth Rates," in *Cancer of the Breast*, 3rd ed, W. Donegan and J. Spratt, Eds. Philadelphia, PA: Saunders, pp. 270-302, 1988.
- [85] D.R. Voegeli, "Mammographic Signs of Malignancy," in *Breast Imaging*, R. L. Eisenberg, Ed. New York, NY: Churchill Livingstone, pp. 183-217, 1989.
- [86] S.L. Lillé, "Background information and the need for screening," in *Mammographic Imaging: A Practical Guide* New York, NY: Lippincott Williams & Wilkins, pp. 7-17, 1992.
- [87] V.F. Andolina, S.L. Lillé, and K.M. Willison, *Mammographic Imaging: A Practical Guide*. New York, NY: Lippincott Williams & Wilkins, 1992.
- [88] S.W. Duffy, L. Tabár, H.-H. Chen, M. Holmqvist, M.-F. Yen, S. Abdsalah, B. Epstein, E. Frodis, E. Ljungberg, C. Hedborg-Melander, A. Sundbom, M. Tholin, M. Wiede, A. Åkerlund, H.-M. Wu, T.-S. Tung, Y.-H. Chiu, C.-P. Chiu, C.-C. Huang, R.A. Smith, M. Rosén, M. Stenbeck, and L. Holmberg, "The impact of organized mammography service screening on breast carcinoma mortality in seven Swedish counties," *Cancer*, vol. 95, no. 3, pp. 458-469, 2002.
- [89] L. Tabár, B. Vitak, H.-H.T. Chen, M.-F. Yen, S.W. Duffy, and R.A. Smith, "Beyond randomized controlled trials," *Cancer*, vol. 91, no. 9, pp. 1724-1731, 2001.
- [90] G. Cardenosa, *Breast Imaging*. Philadelphia, PA: Lippincott Williams & Wilkins, 2004.
- [91] R. Egan, "The new age of breast care," *Administrative Radiology*, p. 9, Sept. 1989.
- [92] American Cancer Society, "Cancer Facts and Figures 2006," Atlanta, 2006.
- [93] S.A. Feig, G.F. Schwartz, R. Nerlinger, and J. Edeiken, "Prognostic factors of breast neoplasms detected on screening by mammography and physical examination," *Radiology*, vol. 133, no. 3, pp. 577-582, 1979.

- [94] National Cancer Institute, "National Cancer Institute Fact Sheet: Improving Methods for Breast Cancer Detection and Diagnosis," 2006. Available: <http://www.cancer.gov/cancertopics/screening/breast>.
- [95] S.J. Nass, I.C. Henderson, and J.C. Lashof, ed., *Mammography and beyond: developing technologies for the early detection of breast cancer*. Washington, DC: National Academy Press, 2001.
- [96] D.A. Berry, K.A. Cronin, S.K. Plevritis, D.G. Fryback, L. Clarke, M. Zelen, J.S. Mandelblatt, A.Y. Yakovlev, J.D.F. Habbema, and E.J. Feuer, "Effect of Screening and Adjuvant Therapy on Mortality from Breast Cancer," *The New England Journal of Medicine*, vol. 353, no. 17, pp. 1784-1792, Oct. 2005.
- [97] American Cancer Society, "Mammograms: Room for Improvement Cited," pp. 1-2, 2004. Available: [www.cancer.org/docroot/NWS/content/NWS\\_2\\_1x\\_Mammograms\\_Room\\_for\\_Improvement\\_Cited.asp](http://www.cancer.org/docroot/NWS/content/NWS_2_1x_Mammograms_Room_for_Improvement_Cited.asp)
- [98] National Cancer Institute, "Cancer Trends Progress Report - 2005 Update," 2006. Available: <http://progressreport.cancer.gov>.
- [99] National Cancer Institute, "DEVCAN: Probability of Developing or Dying of Cancer," Bethesda, MD, 1999.
- [100] M.H. Dilhuydy, A. Le Treut, and J. Weber, "Architecture of the Breast," in *Mammography: A guide to interpretation*, Translated ed, A. Le Treut and M. H. Dilhuydy, Eds. Boston, MA: Mosby Year Book, pp. 38-65, 1991.
- [101] W.R. Hindie and E.R. Ritenour, *Medical Imaging Physics*. New York, NY: Wiley, 2002.
- [102] R.M. Rangayyan, S. Liang, S. Yiping, J.E.L. Desautels, H. Bryant, T.J. Terry, N. Horeczko, and M.S. Rose, "Improvement of sensitivity of breast cancer diagnosis with adaptive neighborhood contrast enhancement of mammograms," *IEEE Trans. on Information Technology in Biomedicine*, vol. 1, no. 3, pp. 161-170, Sep. 1997.
- [103] M.E. Peters, D.R. Voegeli, and K.A. Scanlan, *Breast Imaging*. New York, NY: Churchill Livingstone, 1989.
- [104] L. Tabár and P.B. Dean, *Teaching Atlas of Mammography*, vol. 2nd revised ed. New York, NY: Georg Thieme Verlag, 1985.
- [105] H.D. Cheng, X.J. Shi, R. Min, L.M. Hu, X.P. Cai, and H.N. Du, "Approaches for automated detection and classification of masses in mammograms," *Pattern Recognition*, vol. 39, no. 4, pp. 646-668, Apr. 2006.
- [106] Z. Huo, M.L. Giger, C.J. Vyborny, and C.E. Metz, "Breast Cancer: Effectiveness of Computer-aided Diagnosis—Observer Study with Independent Database of Mammograms," *Radiology*, vol. 224, no. 2, pp. 560-568, 2002.
- [107] L.J.W. Burhenne, S.A. Wood, C.J. D'Orsi, S.A. Feig, D.B. Kopans, K.F. O'Shaughnessy, E.A. Sickles, L. Tabar, C.J. Vyborny, and R.A. Castellino, "Potential Contribution of

- Computer-aided Detection to the Sensitivity of Screening Mammography," *Radiology*, vol. 215, no. 2, pp. 554-562, 2000.
- [108] L. Hadjiiski, H.-P. Chan, B. Sahiner, M.A. Helvie, M.A. Roubidoux, C. Blane, C. Paramagul, N. Petrick, J. Bailey, K. Klein, M. Foster, S. Patterson, D. Adler, A. Nees, and J. Shen, "Improvement in Radiologists' Characterization of Malignant and Benign Breast Masses on Serial Mammograms with Computer-aided Diagnosis: An ROC Study," *Radiology*, vol. 233, no. 1, pp. 255-265, 2004.
- [109] H.-P. Chan, B. Sahiner, M.A. Helvie, N. Petrick, M.A. Roubidoux, T.E. Wilson, D.D. Adler, C. Paramagul, J.S. Newman, and S. Sanjay-Gopal, "Improvement of Radiologists' Characterization of Mammographic Masses by Using Computer-aided Diagnosis: An ROC Study," *Radiology*, vol. 212, no. 3, pp. 817-827, 1999.
- [110] R.L. Birdwell, D.M. Ikeda, K.F. O'Shaughnessy, and E.A. Sickles, "Mammographic Characteristics of 115 Missed Cancers Later Detected with Screening Mammography and the Potential Utility of Computer-aided Detection," *Radiology*, vol. 219, no. 1, pp. 192-202, 2001.
- [111] T.W. Freer and M.J. Ulissey, "Screening Mammography with Computer-aided Detection: Prospective Study of 12,860 Patients in a Community Breast Center," *Radiology*, vol. 220, no. 3, pp. 781-786, 2001.
- [112] N. Karssemeijer, J.D.M. Otten, A.L.M. Verbeek, J.H. Groenewoud, H.J. de Koning, J.H.C.L. Hendriks, and R. Holland, "Computer-aided Detection versus Independent Double Reading of Masses on Mammograms," *Radiology*, vol. 227, no. 1, pp. 192-200, 2003.
- [113] D.J. Winchester and D.P. Winchester, *American Cancer Society Atlas of Clinical Oncology: Breast Cancer*. London, UK: B.C. Decker, 2000.
- [114] M.E. Peters, "Benign Masses," in *Breast Imaging*, R. L. Eisenberg, Ed. New York, NY: Churchill Livingstone, pp. 141-161, 1989.
- [115] D.R. Voegeli, "Other Benign Processes," in *Breast Imaging*, R. L. Eisenberg, Ed. New York, NY: Churchill Livingstone, pp. 163-182, 1989.
- [116] N. Karssemeijer, "Detection of Masses in Mammograms," in *Artificial Intelligence Techniques in Breast Cancer Diagnosis and Prognosis*, A. Jain, A. Jain, S. Jain, and L. Jain, Eds. River Edge, NJ: World Scientific, pp. 187-212, 2000.
- [117] H.-P. Chan, N. Petrick, and B. Sahiner, "Computer-Aided Breast Cancer Diagnosis," in *Artificial Intelligence Techniques in Breast Cancer Diagnosis and Prognosis*, A. Jain, A. Jain, S. Jain, and L. Jain, Eds. River Edge, NJ: World Scientific, pp. 179-264, 2002.
- [118] T. Franquet, C. De Miguel, R. Cozcolluela, and L. Donoso, "Spiculated Lesions of the Breast: Mammographic Pathologic Correlation," *RadioGraphics*, vol. 13, pp. 841-852, Jul. 1993.
- [119] F.B. Demirkazık, M. Gülsün, and P. Firat, "Mammographic feature of nonpalpable spiculated lesions," *Clinical Imaging*, vol. 27, pp. 293-297, Sept. 2003.

- [120] J.M. Jeske, J.R. Bernstein, and M.A. Stull, "Screening and Diagnostic Imaging," in *American Cancer Society Atlas of Clinical Oncology* London, UK: B.C. Decker, pp. 41-63, 2000.
- [121] National Cancer Institute, "National Cancer Institute 2005 Fact Book," no. Final, p. 16, 2005. Available: <http://fmb.cancer.gov/financial/attachments/FY-2005-FACT-BOOK-FINAL.pdf>.
- [122] J. Suckling, J. Parker, D. Dance, S. Astley, I. Hutt, C. Boggis, I. Ricketts, E. Stamatakis, N. Cerneaz, S. Kok, P. Taylor, D. Betal, and J. Savage, "The mammographic images analysis society digital mammogram database," *Digital Mammography*, pp. 375-378, 1994.
- [123] American College of Radiology (ACR), "Breast Imaging Reporting and Data System Atlas (BI-RADS® Atlas)," 2003. Available: <http://www.acr.org>.
- [124] "DDSM: Description of a case," 2006. available: [http://marathon.csee.usf.edu/Mammography/DDSM/case\\_description.html](http://marathon.csee.usf.edu/Mammography/DDSM/case_description.html).
- [125] E.D. Pisano, E.B. Cole, B.M. Hemminger, M.J. Yaffe, S.R. Aylward, A.D.A. Maidment, R.E. Johnston, M.B. Williams, L.T. Niklason, E.F. Conant, L.L. Fajardo, D.B. Kopans, M.E. Brown, and S.M. Pizer, "Image Processing Algorithms for Digital Mammography: A Pictorial Essay," *RadioGraphics*, vol. 20, no. 5, pp. 1479-1491, 2000.
- [126] S. Baeg and N. Kehtarnavaz, "Texture based classification of mass abnormalities in mammograms," *Proc. of the 13th IEEE Symposium on Computer-Based Medical Systems (CBMS)*, Houston, TX, vol. 1, pp. 163-168, Jun. 2000.
- [127] J.S. Lim, *Two Dimensional Signal and Image Processing*. Englewood Cliffs, NJ: Prentice-Hall, pp. 536-540, 1990.
- [128] P. Mayo, F. Rodenas, and G. Verdu, "Comparing methods to denoise mammographic images," *Proc. of the 26th Annual Intl. Conference of the Engineering in Medicine and Biology Society (EMBC)* vol. 1, pp. 247-250, 2004.
- [129] R. Mekle, A.F. Laine, S. Smith, C. Singer, T. Koenigsberg, and M. Brown, "Evaluation of a multiscale enhancement protocol for digital mammography," *Proc. of the Wavelet Applications in Signal and Image Processing VIII*, San Diego, CA, USA, vol. 4119, pp. 1038-1049, Dec. 2000.
- [130] P. Sakellaropoulos, L. Costaridou, and G. Panayiotakis, "A wavelet-based spatially adaptive method for mammographic contrast enhancement," *Physics in Medicine and Biology*, vol. 48, no. 6, pp. 787-803, Mar. 2003.
- [131] A. Laine, F. Jian, and Y. Wuhai, "Wavelets for contrast enhancement of digital mammography," *IEEE Engineering in Medicine and Biology Magazine*, vol. 14, no. 5, pp. 536-550, Sept.-Oct. 1995.
- [132] M.A. Kupinski and M.L. Giger, "Automated seeded lesion segmentation on digital mammograms," *IEEE Trans. on Medical Imaging*, vol. 17, no. 4, pp. 510-517, Aug. 1998.
- [133] E.A. Tabár, "New Swedish breast cancer detection results for women aged 40-49 " *Cancer*, vol. 72, pp. 1437-1448, Aug. 1993.

- [134] S. Baeg, A.T. Popov, V.C. Karnat, S. Batman, K. Sivakumar, N. Kehtarnavaz, E.R. Dougherty, and R.B. Shah, "Segmentation of mammograms into distinct morphological texture regions," *Proc. of the 11th IEEE Symposium on Computer-Based Medical Systems* Lubbock, TX, pp. 20-25, Jun. 1998.
- [135] B. Calder, S. Clarke, L. Linnett, and D. Carmichael, "Statistical models for the detection of abnormalities in digital mammography," *Proc. of the IEE Colloquium on Digital Mammography*, London, UK, pp. 6/1-6/6, Mar. 1996.
- [136] I. Christoyianni, E. Dermatas, and G. Kokkinakis, "Automatic detection of abnormal tissue in mammography," *Proc. of the IEE Colloquium on Digital Mammography*, vol. 2, pp. 877-880, Mar. 2001.
- [137] D.M. Catarious, A.H. Baydush, and C.E. Floyd Jr., "Incorporation of an iterative, linear segmentation routine into a mammographic mass CAD system," *Medical Physics*, vol. 31, no. 6, pp. 1512-1520, Jun. 2004.
- [138] M. Beller, R. Stotzka, T.O. Mueller, and H. Gemmeke, "An Example-based System to Support the Segmentation of Stellate Lesions," in *BVM - image processing in medicine*: Springer, pp. 475-479, 2006.
- [139] K. Bovis and S. Singh, "Detection of masses in mammograms using texture features," *Proc. of the 15th Intl. Conference on Pattern Recognition* Barcelona, Spain, vol. 2, pp. 267-270, Sep. 2000.
- [140] D. Brzakovic, X.M. Luo, and P. Brzakovic, "An approach to automated detection of tumors in mammograms," *IEEE Trans. on Medical Imaging*, vol. 9, no. 3, pp. 233-241, Sep. 1990.
- [141] R. Campanini, D. Dongiovanni, E. Iampieri, N. Lanconelli, M. Masotti, G. Palermo, A. Riccardi, and M. Roffilli, "A novel featureless approach to mass detection in digital mammograms based on support vector machines," *Physics in Medicine and Biology*, no. 6, pp. 961-975, Feb. 2004.
- [142] A. Cao, Q. Song, X. Yang, L. Sheng, and G. Chengyi, "Mammographic mass detection by vicinal support vector machine," *Proc. of the IEEE Intl. Joint Conference on Neural Networks*, vol. 3, pp. 1953-1958, Jul. 2004.
- [143] C. Burges, "A tutorial on support vector machines for pattern recognition," *Data Mining and Knowledge Discovery*, vol. 2, no. 2, pp. 121-167, Jun. 1998.
- [144] D. Guliato, R.M. Rangayyan, W.A. Carnielli, J.A. Zuffo, and J.E.L. Desautels, "Segmentation of breast tumors in mammograms by fuzzy region growing," *Proc. of the 20th Annual Intl. Conference of the IEEE Engineering in Medicine and Biology Society (EMBS)* Hong Kong, vol. 2, pp. 1002-1005, Nov. 1998.
- [145] R. Gupta and P.E. Undrill, "The use of texture analysis to delineate suspicious masses in mammography," *Physics in Medicine and Biology*, no. 5, pp. 835-855, May 1995.
- [146] K. Laws, "Textured Image Segmentation." PhD in Electrical Engineering. Los Angeles, CA: Image Processing Institute, University of Southern California, Jan. 1980.

- [147] K. Laws, "Rapid Texture Identification," *Proc. of the Image processing for missile guidance seminar*, San Diego, CA, pp. 376-380, Jan. 1980.
- [148] N. Székely and B. Pataki, "Tumor Detection on Preprocessed Mammograms," *Proc. of the 11th Mini-Symposium, Budapest, Hungary*, Budapest, Hungary, pp. 54-55, 23-25 May 2004 2003.
- [149] N. Székely, N. Tóth, L. Lasztovicza, and B. Pataki, "Combining Methods For Mass Detection In Mammograms," *Proc. of the 17th Biennial Intl. EURASIP Conference, BIOSIGNAL 2004*, Brno, Czech Republic, pp. 281-283, 23-25 May 2004.
- [150] N. Szekely and B. Pataki, "Detecting lesions in a mammogram," *Proc. of the 4th EURASIP Conference focused on Video/Image Processing and Multimedia Communications* vol. 1, pp. 113-118, Jul. 2003.
- [151] S.M. Lai, X. Li, and W.F. Bischof, "On techniques for detecting circumscribed masses in mammograms," *IEEE Trans. on Medical Imaging*, vol. 8, no. 4, pp. 377-386, Dec. 1989.
- [152] R. Pfisterer and F. Aghdasi, "Comparison of texture based algorithms for the detection of masses in digitised mammograms," *Proc. of the IEEE AFRICON*, Cape Town, South Africa, vol. 1, pp. 383-388, Sep.-Oct. 1999.
- [153] M.D. Heath and K.W. Bowyer, "Mass Detection by Relative Image Intensity," *Proc. of the 5th Intl. Conference on Digital Mammography*, Toronto, Canada, Jun. 2000.
- [154] B.B. Bennett, B.G. Steinbach, N.S. Hardt, and L.S. Haigh, ed., *Breast Disease for Clinicians*. New York: McGraw Hill, p. 133, 2001.
- [155] C. Hagay, "Stellate Images," in *Mammography: A Guide to Interpretation*, Translated ed, A. Le Treut and M. H. Dilhuydy, Eds. St. Louis, MO: Mosby Year Book, pp. 66-78, 1991.
- [156] M.P. Sampat and A.C. Bovik, "Detection of spiculated lesions in mammograms," *Proc. of the 25th Annual Intl. Conference of the IEEE Engineering in Medicine and Biology Society (EMBS)* pp. 810-813, Sept. 2003.
- [157] N. Karssemeijer and G.M. te Brake, "Detection of stellate distortions in mammograms," *IEEE Trans. on Medical Imaging*, vol. 15, no. 5, pp. 611-619, Oct. 1996.
- [158] H. Jiang, W. Tiu, S. Yamamoto, and S.I. Iisaku, "Detection of spicules in mammograms," *Proc. of the 1997 Intl. Conference on Image Processing*, Santa Barbara, CA, vol. 3, pp. 520-523, Oct. 1997.
- [159] H. Kobatake and Y. Yoshinaga, "Detection of spicules on mammogram based on skeleton analysis," *IEEE Trans. on Medical Imaging*, vol. 15, no. 3, pp. 235-245, Jun. 1996.
- [160] W.P. Kegelmeyer, Jr., J.M. Pruneda, P.D. Bourland, A. Hillis, M.W. Riggs, and M.L. Nipper, "Computer-aided mammographic screening for spiculated lesions," *Radiology*, vol. 191, no. 2, pp. 331-337, 1994.
- [161] J.Y. Hsiao and A.A. Sawchuk, "Supervised textured image segmentation using feature smoothing and probabilistic relaxation techniques," *IEEE Trans. on Pattern Analysis and Machine Intelligence*, vol. 11, no. 12, pp. 1279-1292, Dec. 1989.

- [162] S. Liu, C.F. Babbs, and E.J. Delp, "Multiresolution detection of spiculated lesions in digital mammograms," *IEEE Trans. on Image Processing*, vol. 10, no. 6, pp. 874-884, Jun. 2001.
- [163] R. Zwiggelaar, S.M. Astley, C.R.M. Boggis, and C.J. Taylor, "Linear structures in mammographic images: detection and classification," *IEEE Trans. on Medical Imaging*, vol. 23, no. 9, pp. 1077-1086, Sept. 2004.
- [164] R. Zwiggelaar, T.C. Parr, and C.J. Taylor, "Finding oriented line patterns in digital mammographic images," *Proc. of the 7th British Machine Vision Conf.*, pp. 715-724, 1996.
- [165] T. Lindeberg, "Edge detection and ridge detection with automatic scale selection," *Intl. Journal of Computer Vision*, vol. 30, no. 2, pp. 117-154, 1998.
- [166] J.E. Ball and L.M. Bruce, "Digital Mammographic Computer Aided Diagnosis (CAD) using Adaptive Level Set Segmentation," *IEEE Trans. on Medical Imaging*, [under review].
- [167] T. Parr, R. Zwiggelaar, S. Astley, C. Boggis, and C. Taylor, "Comparison of methods for combining evidence for spiculated lesions," in *Digital Mammography: Nijmegen, 1998*, N. Karssemeijer, M. Thijssen, J. Hendriks, and L. v. Erning, Eds. Dordrecht, The Netherlands: Kluwer Academic, pp. 71-78, 1998.
- [168] R. Zwiggelaar, S. Astley, and C. Taylor, "Detecting the central mass of a spiculated lesion using scale-orientation signatures," in *Digital Mammography: Nijmegen, 1998*, N. Karssemeijer, M. Thijssen, J. Hendriks, and L. van Erning, Eds. Dordrecht, The Netherlands: Kluwer Academic, pp. 63-70, 1998.
- [169] M.L. Giger, C.J. Vyborny, and R.A. Schmidt, "Computerized characterization of mammographic masses: analysis of spiculation," *Cancer Letters*, vol. 77, no. 2-3, pp. 201-211, Mar. 1994
- [170] B. Sahiner, H.-P. Chan, N. Petrick, M.A. Helvie, and L.M. Hadjiiski, "Improvement of mammographic mass characterization using spiculation measures and morphological features," *Medical Physics*, vol. 28, no. 7, pp. 1455-1465, Jul. 2001.
- [171] M. Goto, A. Morikawa, H. Fujita, T. Hara, and T. Endo, "Detection of spicules on mammograms based on a multistage pendulum filter," in *Digital Mammography: Nijmegen, 1998*, N. Karssemeijer, M. Thijssen, J. Hendriks, and L. v. Erning, Eds. Dordrecht, The Netherlands: Kluwer Academic, pp. 135-138, 1998.
- [172] R.M. Haralick, I. Dinstein, and K. Shanmugam, "Textural features for image classification," *IEEE Trans. on Systems, Man, and Cybernetics*, vol. SMC-3, pp. 610-621, Nov. 1973.
- [173] N. Petrick, C. Heang-Ping, B. Sahiner, and M.A. Helvie, "Combined Adaptive enhancement and region-growing segmentation of breast masses on digitized mammograms," *Medical Physics*, vol. 26, no. 8, pp. 1642-1654, Aug. 1999.
- [174] A. Agatheeswaran, "Analysis of the effects of JPEG2000 compression on texture features extracted from digital mammograms ". Masters Thesis in Electrical and Computer Engineering. Starkville, MS: Mississippi State University, pp. 20-37, 42-43, Dec. 2004.

- [175] A.N. Papadopoulos, M.E. Plissiti, and D. Fotiadis, "Medical image processing and analysis for CAD systems," in *The Electrical Engineering and Applied Signal Processing Series*, L. Costaridou, Ed. New York: Taylor & Francis, pp. 51-86, 2005.
- [176] J.E. Ball and L.M. Bruce, "Digital mammographic computer aided diagnosis (CAD) using adaptive level set segmentation," *IEEE Trans. on Medical Imaging*, 2007 [under review].
- [177] D.M. Catarious, "A Computer-Aided Detection System for Mammographic Masses." PhD Dissertation in Biomedical Engineering. Durham, NC: Duke University, Aug. 2004.
- [178] M. Kallergi, "Medical Image Analysis Methods," in *The Electrical Engineering and Applied Signal Processing Series*, L. Costaridou, Ed. New York: Taylor & Francis, pp. 433-472, 2005.
- [179] J.A. Hanley and B.J. McNeil, "The Meaning and Use of the Area under a Receiver Operating Characteristic (ROC) Curve," *Radiology*, vol. 143, pp. 29-36, Apr. 1982.
- [180] V. Franc and V. Hlavac, "Statistical Pattern Recognition Toolbox for Matlab User's Guide, Document Number CTU-CMP-2004-08," version 2.05: Center for Machine Perception, Czech Technical University. Jun. 2004. available: <http://cmp.felk.cvut.cz/>.
- [181] N. Eltonsy, H.E. Rickard, G. Tourrasi, and A. Elmaghraby, "Morphological concentric layer analysis for automated detection of suspicious masses in screening mammograms," *Proc. of the 26th Annual Intl. Conference of the IEEE Engineering in Medicine and Biology Society (EMBS)* San Francisco, CA, vol. 1, pp. 1279-1282, Sept. 1-5 2004.
- [182] L. Kinnard, S.-C.B. Lo, P. Wang, M.T. Freedman, and M.F. Chouikha, "Separation of Malignant and Benign Masses using Maximum-Likelihood Modeling and Neural Networks," *Proc.- SPIE The Intl. Society for Optical Engineering*, no. Part 2, pp. 733-741, May 2002.
- [183] J.T. Sample, "Computer Assisted Screening of Digital Mammographic Images." PhD Dissertation in Computer Science. Hattiesburg, MS: The University of Southern Mississippi, Aug. 2003.
- [184] A.O. Bilska-Wolak, C.E. Floyd, Jr., L.W. Nolte, and J.Y. Lo, "Application of likelihood ratio to classification of mammographic masses; performance comparison to case-based reasoning," *Medical Physics*, vol. 30, no. 5, pp. 949-958, May 2003.
- [185] H.D. Cheng and M. Cui, "Mass lesion detection with a fuzzy neural network," *Pattern Recognition*, vol. 37, no. 6, pp. 1189-1200, Jun. 2004.
- [186] G.M. te Brake, N. Karssemeijer, and J.H.C.L. Hendriks, "An automatic method to discriminate malignant masses from normal tissue in digital mammograms," *Physics in Medicine and Biology*, vol. 45, no. 10, pp. 2843-2857, Oct. 2000.
- [187] J.E. Ball and L.M. Bruce, "Digital mammogram spiculated mass detection and spicule segmentation using level sets," *IEEE Trans. on Medical Imaging*, 2007 [under review].
- [188] \_\_\_\_\_, "Matlab," version 7.0.1.15 SP 1, Natick, MA: The Mathworks. Available: <http://www.mathworks.com/products/matlab/>.

- [189] G. Baudat and F. Anouar, "Generalized discriminant analysis using a kernel approach," *Neural Computation*, vol. 12, no. 10, pp. 2385-2404, Oct. 2000.
- [190] C.J. Vyborny, T. Doi, K.F. O'Shaughnessy, H.M. Romsdahl, A.C. Schneider, and A.A. Stein, "Breast Cancer: Importance of Spiculation in Computer-aided Detection," *Radiology*, vol. 215, no. 3, pp. 703-707, Jun. 2000.
- [191] J. Cohen, *Statistical Power Analysis for the Behavioral Sciences*. Hillsdale, NJ: Lawrence Erlbaum Assoc., 1988.
- [192] J.E. Ball and L.M. Bruce, "Level set-based core segmentation of mammographic masses facilitating three stage (core, periphery, spiculation) analysis," *IEEE Trans. on Medical Imaging*, 2007 [under review].
- [193] V.P. Shah, L.M. Bruce, and N.H. Younan, "Applying modular classifiers to mammographic mass classification," *Proc. of the 26th Annual Intl. Conference of the Engineering in Medicine and Biology Society (EMBC)* vol. 3, pp. 1585-1588, Sept. 2004.
- [194] R.J. Ferrari, A.F. Frère, P.M.A. Marques, S.K. Kinoshita, L.A.R. Spina, and R.L. Villela, "Comparative evaluation of statistical pattern recognition techniques for the classification of breast lesions," in *Digital Mammography: Nijmegen, 1998*, N. Karssemeijer, M. Thijssen, J. Hendriks, and L. v. Erning, Eds. Dordrecht, The Netherlands: Kluwer Academic, p. 251, 1998.